Universidad Pública de Navarra
Nafarroako Unibertsitate Publikoa

Universidad Pública de Navarra
Electric and Electronical Engineering department

Contribution to the development of distributed fiber optic sensors based on the Brillouin and Rayleigh scattering effects

This dissertation is submited for the degree of
Doctor of Philosophy

Juan José Mompó i Roselló

Advisor:
Professor **Alayn Loayssa Lara**

Pamplona, April 2020

A la familia:
als que estan
i als que no estan
però mai se n'han anat

Agraïments / Acknowledgements

Perquè hi haurà un dia
que no podrem més
i llavors ho podrem tot.
(Vicent Andrés Estellés)

Arribar ací implica que la part grossa de la feina ja està feta: per fi he acabat d'escriure la tesis. Pero no seria just deixar de reconèixer i agrair a tota eixa gent que ha estat al meu costat donant-me ànims, ajudant-me i recolzant-me en aquestos anys.

Me gustaría empezar agradeciendo al capitán del barco que ha dirigido este viaje llamado tesis: Alayn Loayssa Lara. Su puerta, al final del pasillo a la izquierda, se abrió por primera vez un martes 23 de septiembre de 2014 y siempre ha permanecido así para aclarar dudas (y escuchar alguna que otra idea descabellada). Muchísimas gracias por haber puesto todo tu empeño y fuerzas en llevar por el buen camino a este *valencià*.

No puedo, de ninguna de las maneras, dejar de lado a quién ha sido mi familia más cercana, dentro y fuera de la universidad, y que es de lo mejor que me llevo de Iruña: Jon Mariñelarena, Javier Urricelqui y Amagoia Tellechea. Sin vosotros seguro que esto hubiese sido muy duro y es que, al final, lo que más queda en la memoria son las risas y los buenos momentos, y tenemos unos cuantos. *Eskerrik asko.* También, a los que han contribuido a que ese ratito a mitad del día que dedicábamos a comer, y a apuntar *palitos* en la pizarra de los bizcochos, fueran también momentos de echar unas risas. Bueno, oficialmente ya podemos decir que os dejamos ganar al frontón (¿o no, Jon?) Gracias también!

Tampoco me puedo olvidar a la gente que ha hecho posible que cada día en la universidad se traduzca en buenos momentos. Son muchos y espero no dejarme a nadie: Hartiz Iribas, Santi Tainta, Rosa Ana Pérez, Dani Leandro, Sergio Rota, Mikel Bravo, Mikel Sagues, Manolo López, Santiago de Miguel, Enrique Piñeiro, Desiree, Pablo Zubiate, Adrián... gracias. Entre todos habéis conseguido a que todo este tiempo sea inolvidable.

Durante todo este tiempo he tenido la suerte de poder compartir tiempos con otros grupos de investigación. Me gustaría agradecer a Miguel González Herráez y Sonia Martín López, así como a toda la gente del Grupo de Ingeniería Fotónica de la Universidad de Alcalá de Henares por acogerme como uno más en su laboratorio.

I want to express my most sincere gratitude to professor Avishay Eyal from Tel-Aviv University, Israel, who allowed me to join his group in an experience I will never forget. I can not forget my Israeli friends Lihi, Nadav and Roy who always helped me when I needed and made me feel like home. *Tuda!* My home will always be open for you!

No sería justo dejar de lado a las dos majas con quién tantas anécdotas, y la gestación de alguna resaca, hemos compartido desde que coincidimos en el *euskaltegui*. Tampoco a mis *aseres* preferidos, con quién no podría haber tenido más suerte de compartir piso. Son quienes me hicieron de los mejores guías en su Cuba natal y, sobre todo, con quien he compartido muchas, muchísimas risas, buenos momentos y algún que otro *coulant*.

L'amor i el gust per la ciència és algo amb el que s'ha de nàixer, però també s'ha de cultivar. És per això, que voldria donar les gràcies als professors que m'han inculcat l'amor pel saber, pel preguntar-me el perquè de les coses i el desig de voler anar més lluny. Per això voldria agrair a Rosa Ferrer, de l'IES Josep de Ribera de Xàtiva l'estima cap a la ciència que em va transmetre quan feia quart d'ESO. També a Jose Luís Cruz, del departament de Física aplicada de la universitat de València qui em va obrir les portes del món de la fotónica, un mon desconegut per a mi, quan vaig tocar a la porta del seu despatx preguntant per un treball final de grau sobre antenes. També voldria agrair a les institucions que han permès que aquesta tesis s'haja pogut transformar en una realitat: Universidad Pública de Navarra, fons FEDER i al Ministeri d'Economia i competitivitat que m'han financiat a través del projecte TEC2013-47264-C2-2-R.

Hi ha amics que arriben per a quedar-se i és que, més enllà de les quatre grans forces de la física, existeix la força de l'amistat que també ha unit la Física. Ells són Oreto, Gemma, Maria Dolores i Quatre. Qui ens anava a dir que hi havia vida més enllà d'aquella classe on veiérem, entre flors, les equacions de Maxwell per primera vegada?

No em puc deixar de costat als meus amics del poble, de La Torre. Sempre han estat, estan i estaran ahi quan fa falta, especialment a tots els que no fallen cap divendres (ni dissabte) per la vesprada a la cerveseta del mercat. És prou tindre un dia fotut com per a que qualsevol d'ells t'alce l'ànim en un tres i no res. Gràcies de tot cor AMICS! També a Marieta, que sempre que ha estat ahi i segur que continua estant, gràcies xiqueta!

Finalment, no em puc oblidar a la gent que més prop he tingut sempre, els que mai fallen, els que han fet de mi qui sóc i als que dedique la tesis: la meua família. Especialment a ma uela, Nieves *La Fornera* qui en este moment està preparant mones de pasqua, les millors de tota la contornà, per a berenar quan acabe d'escriure acò. Òscar, prepara't que el pròxim eres tu!

En resum, moltíssimes gràcies a tots als que heu estat ahi. Als que no, que ...

Juan José Mompó Roselló
Torre D'en Lloris
Abril 2020

Abstract

Distributed optical fiber sensors DOFS are a technology that have acquired considerable importance due to their applications in areas such as structural health monitoring (SHM), intrusion detection in perimeters or the monitoring of high voltage line oil and gas pipelines. DOFS are suitable to monitor extra-large distances, of the order of hundreds of km with a high spatial resolution, offering a huge quantity of resolved points. Among DOFS, those based on Brillouin and Rayleigh scattering are in the center of attention due its capability to monitor, simultaneously, temperature and strain. Besides, DOFS based on Rayleigh scattering can be used to perform high frequency dynamical measurements.

Among sensors based on Brillouin scattering, Brillouin optical time-domain analysis (BOTDA) is one of the most studied and developed techniques due to its capabilities to realize extra-large distances measurements of strain and temperature with high spatial resolution. In the last years, BOTDA has been the focus of research to improve its performance regarding longer sensing range, high accuracy measurements and higher spatial resolutions, among others. One of the main problems that impair the performance of BOTDA is the second-order non local effects (NLE). Second-order NLE affect BOTDA sensors that use two probe waves to compensate the transfer of energy between probe wave and pump pulse. It causes a spectral distortion of the pump pulse that is translated to measurement errors. Another consequence of second-order NLE is a limitation in the maximum probe wave power that can be injected in the fiber limiting, in turn, the maximum sensing range of the sensor. In this thesis, we theoretically and experimentally demonstrate that the previous techniques presented to mitigate second-order NLE are only effective when the Brillouin frequency shift (BFS) along the sensing fiber does not present strong variations. In real world, this scenario is not realistic because of the deployment of fibers with different BFS and existence of fiber links exposed to different environmental conditions. We present a technique that reduces the onset of second-order NLE related to the variation of the BFS of the fiber. This technique is based on the modulation of the frequency of the probe wave to track the variations of the BFS of the fiber. This method has been experimentally tested and we have demonstrate, to the best of our knowledge, the largest probe wave ever injected in a BOTDA sensing link.

Another problem that impairs the performance of BOTDA sensors is the attenuation of its optical signals. This leads to a limit of the sensing range of the sensor. In this thesis, we present a simple technique to provide pulse amplification to a BOTDA sensors. This technique is based on filtering out the low frequency probe wave and managing the sensor in loss configuration in order to have energy transferred from the probe wave to the pump pulse, which is amplified as it conter-propagates with the probe wave through the optical fiber. Besides, the probe wave is frequency modulated in order for the pump pulse to experience a flat total gain spectrum that amplify equally all the spectral components of the pulse. In addition, this frequency modulation

prevents the apparition of second-order NLE and spontaneous Brillouin scattering (SpBS), allowing to increase the maximum optical power of the probe wave.

Another technology vastly used in DOFS is based on Rayleigh scattering. It was demonstrated for the first time 40 years ago and has experimented an exponential growth in the last years due to its capabilities. Second part of this thesis is based on the development of DOFS based on Rayleigh scattering. Among the multiple techniques, phase-sensitive optical time-domain reflectometry (ϕ-OTDR) is the most used due to its simplicity and measurements that provides. The basics of ϕ-OTDR consists on launching a coherent optical pulse into the fiber. As the pulse travels through the fiber multiple reflections are backscattered. These reflections interfere coherently in the detector, generating an interference pattern which variates according to the perturbations that affect the fiber.

One of the problems that affect ϕ-OTDR is the attenuation of the pulse. It reduces the quantity of the energy that pulse contains, then the SNR of the measured signal. A possible solution to increase the energy is to increase the amplitude or the duration of the pulse, but these two solutions are limited by non-linear effects and loss of spatial resolution. A possible solutions to overcome these limitations is a technique that permits to increase the pulse energy without impairing the spatial resolution or introducing non-linear effects. This, technique known as optical pulse compression reflectometry (OPCR), applies a matched filter to the measured signal. However, the resultant signal presents sidelobes that impairs the SNR of the mesurement. In this thesis, we demonstrate a technique to mitigate these sidelobes by filtering the injected signal using a Gaussian-shape probe pulse with linear frequency modulation (LFM). Using this technique, a reduction of 13 dB in the power of the sidelobes has been achieved compared with previous OPCR techniques using a square-shape probe pulse.

Another limitation that impairs the performance of the ϕ-OTDR is fading. There are two main sources of fading. One of them is signal fading, which comes from the destructive interference of multiple backscattering signals. The other one is the polarization fading which results from the combinations of two signals with different state-of-polarization (SOP). It reduces the mixing efficiency in coherent detection and, consequently the SNR of the received signal. In this thesis, we present a technique that simultaneously reduces both kinds of fading by launching into the fiber four sequential pulses with different frequencies and relative SOP. To do that, each pulse is modulated in a different optical wavelength and a differential group delay (DGD) turns the relative SOP according to their optical wavelength. All this is done in a all-fiber setup, so it does not introduces time penalty in the measurement. The combination of different SOP and optical wavelengths provides measure backscattering signals statistically independent and with different SOP so, at least one of them will not suffer fading.

Finally, ϕ-OTDR presents a limitation in environments where high and fast strain changes has to be measured, such as in structural health monitoring (SHM). Phase unwrapping techniques fail when phase difference between two consecutive samples exceeds a value of π. In this thesis, a technique based on the measurement of two optical signals with a slightly difference of optical phase. This difference is obtained propagating the optical signals through the two axes of a polarization-maintaining (PM) fiber, which exhibits slightly different propagation constants. The difference between the phase of these two signals is proportional to the phase variation induced by the perturbation. This permits to reduce the sensitivity of the sensor and, consequently, increase the amplitude of the perturbation that can be measured without phase-wrapping issues. In addition, since both axes of the PM fiber exhibits an statistically independent backscattering response, both signals can be combined in order to avoid signal fading.

In summary, in this thesis different techniques to improve the performance DOFS based on

Brillouin and Rayleigh scattering have been presented and experimentally demonstrated. These new techniques permit to increase the sensing range and accuracy of BOTDA measurements and to enhance the SNR and the fading tolerance of ϕ-OTDR sensors.

Resumen

Los sensores distribuidos de fibra óptica (DOFS, por sus siglas en inglés) son una tecnología que ha adquirido una importancia notable debido a sus propiedades en la monitorización de estructuras, detección de intrusiones en perímetro y control de líneas de alta tensión, oleoductos y gaseoductos. Entre otra propiedades, los DOFS pueden monitorizar grandes distancias, del orden de cientos de kilómetros, con una gran resolución espacial, ofreciendo una gran cantidad de puntos resueltos de medida. Entre los DOFS, son los que están basados en dispersión Brillouin y Rayleigh los que gozan de mayor atención debido a su capacidad de medir, de forma simultanea temperatura y deformación mecánica. Además, los DOFS basados en dispersión Rayleigh pueden ser usados para caracterizar medidas de vibración a altas frecuencias.

Entre los sensores basados en la dispersión Brillouin, el análisis óptico de la dispersión Brillouin en el domino del tiempo (BOTDA, por sus siglas en inglés) es uno de los más estudiados dado que ofrece la posibilidad de monitorizar temperatura y deformación mecánica en distancias ultra largas ofreciendo una alta resolución espacial. En los últimos años, los sensores BOTDA has sido objeto de mucha investigación con el objetivo de mejorar sus prestaciones como son conseguir mayores distancias, precisión en las medidas y mayor resolución espacial entre otras.

Uno de los problemas que afecta a los sensores BOTDA son los efectos no locales de segundo orden (second-order NLE por sus siglas en inglés). Los NLE de segundo orden afectan a los BOTDA que usan dos ondas de prueba para compensar la transferencia de energía entre la onda de prueba y el pulso. Sus consecuencias son una distorsión espectral del pulso de bombeo que, a su vez, se traduce en errores en la medida y, por otra parte, una limitación de la potencia máxima de onda de prueba que se puede inyectar en la fibra que se traduce en una disminución de la máxima distancia a la que se puede medir. En esta tesis demostramos teóricamente y experimentalmente que las técnicas que se habían presentado previamente para reducir los NLE de segundo orden sólo funcionan bien cuando el perfil de desplazamiento en frecuencia Brillouin (BFS, por sus siglas en inglés) no presenta grandes variaciones a lo largo de la fibra. Este es un escenario que en el mundo real no se da bien por la diferencia de fibras empleadas o por las condiciones ambientales del entorno donde están instaladas. En esta tesis se presenta una técnica que reduce el impacto del los NLE de segundo orden cuando existen variaciones de BFS en al fibra. Esto se consigue modulando en frecuencia la onda de prueba y haciendo que la frecuencia de modulación siga el perfil de BFS que presenta la fibra. Este método se ha demostrado experimentalmente con la mayor potencia de onda de prueba que jamás se ha inyectado, hasta la fecha, en un dispositivo BOTDA.

Otro de los problemas que limitan las características de los sensores BOTDA es la atenuación que sufre las ondas ópticas usadas para medir la dispersión Brillouin. Esto se traduce en una limitación de la máxima distancia a la que puede trabajar el sensor. En esta tesis presentamos una técnica simple que proporciona una amplificación intrínseca de la onda pulsada en sensores

BOTDA. Esta técnica se basa en filtrar la onda de baja frecuencia y manejar el sensor el configuración de pérdida. De esta forma se consigue que la transferencia de energía entre la onda de prueba y la pulsada, cuando se contrapropagan a través de la fibra, se traduzca en una ganancia neta de energía de la onda pulsada. Además, la onda de prueba se modula en frecuencia para conseguir una amplificación constante en todas las componentes espectrales de la onda pulsada. Esta modulación plana, a su vez, permite reducir la aparición de la emisión espontanea de Brillouin (SpBS, por sus siglas en inglés) de la onda de prueba al mismo tiempo que reduce la aparición de NLE de segundo orden.

Otra de las tecnologías ampliamente usadas en DOFS está basada en la dispersión Rayleigh. Esta fue demostrada inicialmente hace 40 años pero no ha sido hasta los últimos años cuando su desarrollo ha experimentado un crecimiento exponencial debido a sus propiedades. La segunda parte de esta tesis está centrada en la contribución al desarrollo de sensores basados en este tipo de dispersión. Entre las distintas técnicas, la reflexión óptica en el dominio del tiempo de forma coherente (ϕ-OTDR, por sus siglas en inglés) es la más usada debido a su simplicidad y propiedades que presenta como, por ejemplo, una sensibilidad extremadamente alta. La idea básica de un sistema ϕ-OTDR consiste en lanzar un pulso óptico en el interior de una fibra óptica y medir el patrón de interferencia que generan las múltiples reflexiones que el pulso genera mientras se transmite a través de la fibra. Este patrón de interferencia depende de la fase relativa entre las múltiples reflexiones, por lo que de la variación del patrón de interferencia se puede saber dónde ha habido una perturbación en la fibra.

Uno de los problemas que afectan a ϕ-OTDR es la atenuación que sufre el pulso de sondeo. Esto se traduce en una reducción de la energía del pulso y, como consecuencia, pérdida de SNR de la señal medida. Una posible solución para incrementar la energía consiste en incrementar la amplitud o la duración del pulso, pero estas soluciones presentan limitaciones por efectos no lineales y por la degradación de la resolución espacial. Una solución que evita estas limitaciones consiste en realizar una compresión de de pulso mediante la aplicación de un *matched filter* (MF) a la señal reflejada, pero esta técnica provoca la aparición de lóbulos laterales en la señal comprimida, degradando la SNR de la misma. En esta tesis, presentamos una técnica que usa pulsos con envolvente Gaussiana y modulación lineal de frecuencia (LFM). Usando esta técnica se ha demostrado reducir la amplitud de los lóbulos laterales en 13 dB respecto de las técnicas previas donde se usaban pulsos con envolvente cuadrada.

Otra de los problemas que limitan las prestaciones de los sensores ϕ-OTDR es el fading. Existes dos causas principales de fading. Por un lado está el fading de señal que es consecuencia de las interferencias destructivas de las señales reflejadas. El otro, llamado fading de polarización, es consecuencia del mezclado de dos señales con diferentes estados relativos de polarización (SOP, por sus siglas en inglés). Esto puede inducir una reducción de la eficiencia de suma de ondas en la detección coherente, lo que se traduce en una reducción de la SNR de la señal medida. En esta tesis presentamos un sistema que reduce, de forma simultánea, ambos tipos de fading. Esta técnica se basa en lanzar, de fora consecutiva, pulsos con diferentes frecuencias y SOP. Para hacer eso, se modula cada pulso con una frecuencia óptica diferentes y un retardador diferencial de grupo (DGD por sus siglas in inglés) gira el SOP de cada pulso según la frecuencia óptica del mismo. De esta forma, mediante la combinación de pulsos con diferentes longitudes de onda óptica y SOP se asegure que, al menos uno de los múltiples pulsos no esté afectado por fading.

Finalmente, una limitación que presenta ϕ-OTDR en escenarios como monitorización de grandes estructuras, o aeronáutica, son los cambios grandes, o rápidos, de fase entre dos medidas consecutivas. Esto genera que, cuando el cambio de fase entre dos medidas consecutivas es mayor que π las técnicas de reconstrucción de fase presenten un mal funcionamiento. Para combatir esta

limitación, en esta tesis hemos presentado una técnica que usa las medidas de dos señales ópticas con una pequeña diferencia de fase entre ellas. Esta diferencia se obtiene haciendo propagar las señales a través de los ejes principales de una fibra mantenedora de polarización (PM), los cuales tienen constantes de propagación ligeramente diferentes. La diferencia de fase entre las dos señales sigue la forma de la perturbación, lo que permite medir perturbaciones que excedan la diferencia de π entre dos medidas consecutivas.

En resumen, en esta tesis se presenta diferentes técnicas que contribuyen en la mejora de DOFS basados en dispersión Brillouin y Rayleigh. Todas estas técnicas han sido demostradas experimentalmente mostrando resultados prometedores. Con estas nuevas técnicas, los sensores BOTDA pueden llegar a medir más lejos y con más precisión. Además, las técnicas encaradas a mejorar las prestaciones basadas en dispersión Rayleigh coherente permiten mejorar la SNR de la señal, reducir el fading que afecta a la señal medida así como incrementar notablemente la máxima amplitud de la perturbación que se puede medir.

Contents

List of acronyms

AC	alternating current
ASE	amplification spontaneous emission
AWG	arbitrary waveform generator
BFS	Brillouin frequency shift
BGS	Brillouin gain spectrum
BOCDA	Brillouin optical correlation-domain analysis
BOFDA	Brillouin optical frequency-domain analysis
BOTDA	Brillouin optical time-domain analysis
BPD	balanced photodetector
C-OTDR	coherent-optical time domain reflectometry
CW	continuous wave
DAS	distributed acoustic sensing
DBA-BOTDA	distributed Brillouin amplifier-Brillouin optical time-domain amplifier
DBA	distributed Brillouin amplifier
DC	direct current
DFB	distributed feedback laser
DGD	differential group delay
DP-EOM	dual parallel-electrooptic modulator
DPP	differential pulse pair
DOFS	distributed optical fiber sensors
DPOH	dual polarisation optical hybrid
DRA	distributed Raman amplification
DSF	dispersion shifted fibers
DVS	distributed vibration sensor
DWDM	dense wavelength division multiplexing
EDFA	Erbium doped fiber amplifier
ER	extinction ratio
FBG	fiber Bragg grating
FM	frequency modulation
FFT	fast Fourier transform
FWHM	full-wave half-maximum
FUT	fiber under test
GL	gauge length

I	in-phase
IFFT	inverse fast Fourier transform
I-OTDR	incoherent- optical time domain reflectometry
LFM	linear frequency modulation
LO	local oscillator
MF	matched filter
MI	modulation instability
MZ	Mach-Zehnder
MZ-EOM	Mach Zehnder-electrooptic modulator
NLE	non-local effects
OF	optical filter
OFS	optical fiber sensors
OFDR	optical frequency domain reflectometry
OPCR	optical pulse compression reflectometry
OSA	optical spectrum analyzer
OSSB	optical single-sideband
OSSB-EOM	optical single-sideband electro optical modulator
OTDR	optical time domain reflectometry
PAC	perfect auto-correlation
PBS	polarization beam splitter
PC	polarization controller
PFS	piezoelectric fiber stretcher
PG	pulse generator
PM	polarization maintaining
PPA	perfect periodic autocorrelation
PS	polarization scrambler
PSK	phase shift keying
PSR	peak side-lobe ratio
Q	in-quadrature
SBS	spontaneous Brillouin scattering
second-order NLE	second order non-local effects
SHM	Structural Health Monitoring
SMF	single mode fiber
SNR	signal-to-noise ratio
SOA	semiconductor optical amplifier
SOP	state-of-polarization
SPM	self-phase modulation
SpBS	spontaneous Brillouin scattering
RF	radio frequency
RZ	return-to-zero
SBS	stimulated Brillouin scattering
RIN	relative intensity noise
RS	Rayleigh scattering
VNA	vector network analyzer
VOA	variable optical attenuator

List of Figures

Introduction to this thesis

Motivation of this thesis

The use of optical fibers in the field of the telecommunication industry has contributed, due to its low optical attenuation, to reach long distances when propagating signals. Besides, as a result of their substantial optical bandwidth, the rate of data transmission is higher when compared with conventional radio or electric cable systems. All of this has permitted us to develop an extensive optical fiber network around the world.

Further, their use for data transmission, another essential use of optical fiber is the development of optical fiber sensors (OFS). Intrinsic OFS take advantage of variations that light experience in its propagation along the fiber in response to environmental conditions. OFS can be classified into two main groups: punctual sensors, such as fiber Bragg grating (FBG), and DOFS, which use the whole fiber as a sensor, working as a virtual array of multiple punctual sensors.

Other sensors, such as punctual electrical sensors, use electrical cables to feed and read the measured values of the sensor. As a consequence of the use of electrical cables, this kind of sensor is not suitable when used in environments affected by electromagnetic interferences. In contrast, optical fiber used in OFS is made with a dielectric material makes to this kind of sensor suitable to be used in environments affected by electromagnetic interferences.

In addition, since in OFS the whole optical fiber is used as a sensor, all the points that fiber covers are a candidate to be measured, whereas when the punctual sensors, all the points between two consecutive sensors can not be measured giving an advantage of the DOFS over conventional punctual sensors. Moreover, DOFS can be entirely developed using standard telecom fiber without any modification, which facilitates the implementation using the existent optical fiber network.

The continuum measurements that DOFS provide permits them to be employed in large structures when a significant number of points has to be measured simultaneously. As a consequence, the cost per sensing point is dramatically reduced.

For all these reasons, OFS has become a revolutionary technique in the field of structure health monitoring (SHM). The use of this kind of sensors is continuously growing. During 2017, its market value was USD 852.15 Million in 2017 and is projected to reach USD 2592.28 Million by 2025 [4].

Basically, there are three kinds of optical effects that permits to implement DOFS. First of all, Raman scattering which permits to measure temperature. Another technique is Brillouin scattering, which measures temperature and strain. Finally, Rayleigh scattering offers, in addition to

strain and temperature variation, the possibility to deploy acoustic distributed sensors. Nevertheless, DOFS are not limited to strain and temperature measurement. Their field of applications is vast and includes monitoring of large structures such as tunnels, dams, oil and gas pipelines deformation, perimeter intrusion. In addition, DOFS can be used to detect humidity, vibrations, nuclear radiation among others. The key to these measurements is to link the desired parameter to temperature and /or strain measurement.

Objectives of the PhD thesis

The work done during this thesis is focused on the contribution of the improvement of the performance of distributed optical fiber sensors (DOFS) based on BOTDA which is one of the most studied and developed Brillouin based on sensors and phase-optical time-domain reflectometry (ϕ-OTDR), one of the most studied Rayleigh distributed sensor.

During the first part of this thesis, the objective of this thesis has been focused on the improvement of the performances of BOTDA sensors. These improvements have been done through an enhancement of the SNR that permits to meliorate the sensing range, spatial resolution and accuracy of measurements.

- The SNR of the BOTDA sensors depends on the optical power that sensor deploys. The maximum optical power are limited by non local effects (NLE) and non lineal effects.
  - Study and mitigation second-order NLE. This effect distorts the spectrum of the pulsed wave which induces an error in the measured value of strain and temperature. To prevent the apparition of second-order NLE the maximum optical power of the probe wave is limited, therefore, the SNR of the sensor. An objective of this thesis is to modify the prove wave in order to avoid second-order NLE then increase the maximum optical power and the SNR of the sensor.
  - The maximum optical power of the pulsed wave is limited by modulation instability. It limits the maximum amplitude of the pulsed wave. An objective of this thesis is to develop a system that generates intrinsic amplification over the pulsed wave therefore increase the SNR of the sensor and, consequently, extend the sensing range and enhance the spatial resolution an accuracy of the system.
- Improvement in ϕ-OTDR sensors. The performance of this kind of sensors depends on the SNR of the measured optical signal. The objective of this thesis in ϕ-OTDR sensors are:
  - Contribute to develop a techinque that permits to increase the sensing range without damage the spatial resolution of the sensor.
  - Develop a system that permits to mitigate simultaneously polarization and signal fading without the use of polarization diversity detection scheme.
  - Contribute to the development of a system that permits to increase the dynamic range of the measured perturbation in ϕ-OTDR sensors.

Structure of the thesis

In order to present and demonstrate how each one of these objectives has been carried out, the content of this thesis has been divided into seven chapters.

- Chapter 1: Introduction

  This chapter is divided into two main parts:

  First one, Brillouin scattering and its use in DOFS are presented. Then, the main techniques of sensors based on Brillouin scattering, and their limitations are explained. Finally, the BOTDA technique, which is used during the thesis, is deeply explained as well as its limitations and how they have been avoided using techniques previously presented.

  The second part of the introduction is used to introduce DOFS based on Rayleigh scattering. First a brief explanation of the evolution of the techniques using this effect for sensing is presented. Then, the differential phase-OTDR method and its principal limitations are presented.

- Chapter 2: Non-Local effects mitigation by tracking of the Brillouin frequency shift (BFS) of the fiber

  This chapter introduces NLEs that affect the performance of BOTDA sensors. First, the physical origin of this kind of limitation is presented, as well as how it has been previously mitigated. Then, theoretically and experimentally, the apparition of second order non-local effects (second-order NLE) is demonstrated. Finally, a new technique implemented to avoid second-order NLE is presented.

- Chapter 3: Pump wave amplification in long-range BOTDA

  This chapter describes the optical attenuation of the pulse wave and its effect over the performance of the BOTDA sensor. Then, a technique to amplify the power of the pulse and compensate the optical attenuation is presented.

- Chapter 4: Sidelobes apodization in optical pulse compression DAS

  This chapter, the first one about DOFS based on Rayleigh scattering, is focused on extending the measuring range without a loss of spatial resolution. Pulse compression technique and its limitations, related to the apparition of sidelobes, are explained. Finally, a technique to mitigate the apparition of sidelobes is theoretically and experimentally demonstrated.

- Chapter 5: Mitigation of Rayleigh and polarization fading in DAS

  In this chapter, the origin of fading, which damage the signal-to-noise ratio (SNR) of the measured signal, is introduced. Both sources of fading and previous technique that have been introduced to avoid them are explained. Finally, a technique that mitigates all fading effects simultaneously is theoretically and experimentally demonstrated.

- Chapter 6: High dynamic range measurements in DAS

  In this chapter, a technique to increase the maximum amplitude of the perturbation that can be measured in a DAS sensor is presented. The maximum amplitude is limited by phase wraping. The new technique uses the phase difference between the two orthogonal signals generated in a DAS using the two principal polarization axis in a PM fiber. This phase difference follows the profile of the perturbation, but its amplitude is proportional to the difference of refractive index between both axis of the PM fiber.

- Chapter 7: Conclusions and open lines

  Finally, this chapter offers a summary of what has been done in each part of this thesis. Open research lines in Brillouin and Rayleigh based on DOFS are given as well.

CHAPTER 1

DOFS based on Brillouin and Rayleigh scattering

1.1. Scattering in optical fibers

THERE are different scattering effects that appear when a light beam is transmitted through a medium. The way that scattering is generated depends on the intensity of incident light. The first one is spontaneous scattering, which occurs when the intensity of the light transmitted through the media does not exceed a certain threshold. In this case, the medium is not modified by the effect of the light. In the other case, when the power of the light overcomes this threshold, the effect is known as stimulated. In this case, the intensity of the light modifies the properties of the medium leading to a non-linear effect.

In terms of energy, scattering phenomena are classified in elastic processes, where the energy of the incident and scattered photons have the same energy (same frequency), and inelastic processes where the energy of the scattered photons is different from the incident photons. In the latter, the frequency of the emitted photon is different from the input photon.

There is another classification of scattering processes that is more useful for this thesis: according to their nature. There are three kinds of the scattering process. The first one is **Raman scattering**. This kind of scattering comes from the interactions between incident photons and optical phonons, which have higher energy, in frequency, in the order of tens of THz ($\sim$14 THz in optical fibers) [5]. **Brillouin scattering** is the scattering of light due to their interaction with sound waves that come from the propagation of the pressure and density waves. As an inelastic process, where the incident light interacts with acoustic phonons, the frequency of the scattered light changes. This process will be the focus of study in the first half part of this thesis due to its potential to characterize strain and temperature when the process occurs in optical fibers. Finally, among the elastic process where the energy (frequency) of the scattered light is not modified, is **Rayleigh scattering**. There are two kinds of Rayleigh scattering processes that come from different interactions. The first one, called **Rayleigh-wing**, comes from fluctuations in the orientation of the anisotropic molecule. Their reorientation process is very fast, so its spectral content is enormous. The other one, known as **Rayleigh scattering** or Rayleigh-center scattering is the scattering produced by the interaction with a non-propagating density fluctuations [5]. This last scattering process will occupy the second part of this thesis due to its potential to provide

distributed vibration sensing. The frequency distribution of all the scattering process is shown in Fig. 1.1.

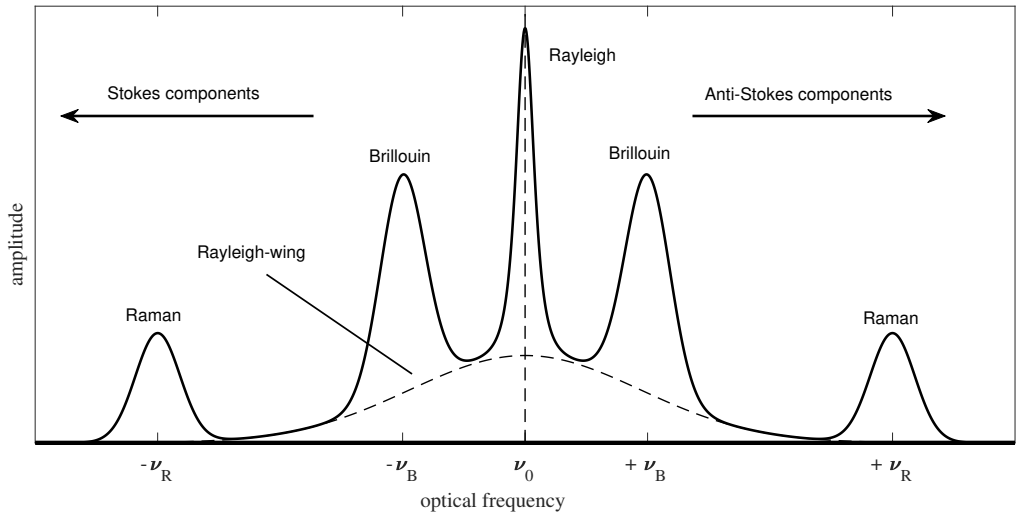

Figure 1.1: Spectrum of the different optical scattering processes in an inhomogeneous medium. ν_R denote frequency of Raman scattering, ν_B mean frequency of Brillouin scattering process. ν_0 is the frequency of the Rayleigh scattering.

1.2. Interaction between photon and acoustic phonon: Brillouin scattering

As mentioned in the introduction of this chapter, Brillouin scattering comes from the interaction between incident photons and sound waves (acoustic phonons) that are propagated through the fiber. Following the mathematical description used in [5], Brillouin scattering can be described starting from the equation of motion for a pressure wave, which is well known from the acoustics field and is given by:

$$\frac{\partial^2 \Delta p}{\partial t^2} - \Gamma \nabla^2 \frac{\partial \Delta p}{\partial t} - v_a^2 \nabla^2 \Delta p = 0 \tag{1.1}$$

In this equation the damping coefficient is given by Γ and v_a is the velocity of the acoustic wave, which is given, in terms of thermodinamics variables, by:

$$v_a^2 = \left(\frac{\partial p}{\partial \rho}\right)_s = \frac{1}{C_s \rho} \tag{1.2}$$

where C_s is the compressibility at a constant entropy and ρ is the density. The propagation of the acoustic involved in the interaction can be described as:

$$\Delta p = \Delta p_0 exp\left[i(qr - \Omega t)\right] + c.c \tag{1.3}$$

where the frequency of the acoustic wave is denoted by $\Omega = v_a|q|$, and q is its wave vector. Finally, without loss of generality, in the interaction between the incident wave and the acoustic wave, the incident wave can be described by a monochromatic wave:

$$E = E_o exp\left[i(kr - \omega t)\right] + c.c. \tag{1.4}$$

where its angular frequency and wave vector are given by ω and k.

The scattered field obeys the perturbed wave equation, which is derived from Maxwell's equation:

$$\nabla^2 E - \frac{n^2}{c^2}\frac{\partial^2 E}{\partial t^2} = \mu_0 \frac{\partial^2 P}{\partial t^2} \tag{1.5}$$

where n and c are the index of refraction of the medium and the velocity of the light in the vacuum, E, is the electric field and P is the polarization field induced by electric dipoles. The relation between polarization and electric field is given by:

$$P = \nabla\chi E = \Delta\varepsilon E \tag{1.6}$$

where $\nabla\chi$ is the fluctuation of the dielectric susceptibility that is translated to fluctuation of dielectric constant, $\Delta\varepsilon$. Variations of both, $\nabla\chi$ and $\Delta\varepsilon$ result in a variation of refraction index. If variation of refraction index is given by fluctuations of adiabatic density, such as acoustic waves, Eq. 1.6 becomes:

$$P = \varepsilon_0 \left(\frac{\partial\varepsilon}{\partial\rho}\right)\left(\frac{\partial\rho}{\partial p}\right)\Delta p E = \varepsilon_0 \gamma_e C_s \Delta p E \tag{1.7}$$

Combining Eq. 1.3, 1.5 and 1.7, it gives:

$$\nabla^2 E - \frac{n^2}{c^2}\frac{\partial^2 E}{\partial t^2} = -\frac{\gamma_e C_s}{c^2}\left[(\omega-\Omega)^2 E_0 \Delta_p^* e^{i((k-q)r-(\omega-\Omega)t)} + (\omega-\Omega)^2 E_0 \Delta_p e^{i((k+q)r-(\omega+\Omega)t)} + c.c.\right] \tag{1.8}$$

In the last equation, the first term is related to Stokes scattering, while the second one to anti-Stokes scattering. Frequency and vector wave are $\omega' = \omega - \Omega$ and $k' = k - q$ for Stokes wave and $\omega'' = \omega + \Omega$ and $k'' = k + q$ for anti-Stokes wave. Acoustic phonons that intervene in a Brillouin scattering process carry a momentum which value moves proportionally to the frequency of the phonon that is, in turn, given by the acoustic velocity of the medium. Frequency and wave vector of the incident optical field, involved in Brillouin scattering, are related by

$$\omega = |k|\frac{c}{n} \tag{1.9}$$

also, the parameters that define the acoustic wave are connected by:

$$\Omega = |q| v_a \tag{1.10}$$

The scatter optical wave can be coupled efficiently to this component of polarization only when its frequency, ω' and vector wave, k', are related, by the relation of dispersion, as:

$$\omega' = |k'|\frac{c}{n} \tag{1.11}$$

In Brillouin scattering, the frequency of the sound wave and wave vector must each have a particular value for any particular direction in order to satisfy the requirements of Brillouin scattering.

1.2.1. Conservation of momentum and energy in Brillouin scattering process

During the scattering process, both total momentum and energy are kept constant. In the case of energy, the three waves involved in the interaction are related according to:

$$\frac{h}{2\pi}\omega = \frac{h}{2\pi}(\omega' + \Omega) \tag{1.12}$$

for the momentum, it follows:

$$hk = h(k' + q) \tag{1.13}$$

where h is the constant of Plank. Due to $|k|$ is very similar to $|k'|$, since Ω is much smaller than ω, so q and k are related as:

$$|q| = 2|k|sin\left(\frac{\theta}{2}\right) \tag{1.14}$$

where θ is the angle between the wave vector of the input and output optical wave. The relation of dispersion, given by Eq. 1.10 can be described, considering that the acoustic velocity is much smaller than light velocity, as:

$$\Omega = \frac{2n\omega v_a}{c} sin\left(\frac{\theta}{2}\right) \tag{1.15}$$

It is found the that acoustic frequency varies between a minimum value of 0, when $\theta = 0$ (forward scattering), and a maximum value for a $\theta = \pi$ (backscattering). In this case, the acoustic frequency, known as BFS is given by[5, 6]:

$$\Omega_{max} = \frac{2n\omega v_a}{c} = \frac{2n\omega}{c}\sqrt{\frac{(1-\kappa)Y}{(1-2\kappa)(1+\kappa)\rho}} \tag{1.16}$$

where κ is the Poisson ratio, Y is the Young modulus and ρ is the density of the material. For the case of standard optical fiber working at the third communication windows ($\sim 1550\ nm$), the frequency shift ($\nu_a = \Omega/2\pi$) becomes 10.8 GHz.

1.2.2. Brillouin spectrum and linewidth

In the previous deduction of the acoustic wave, its attenuation has been neglegted, however the Brillouin wave scattered has a linewidth due to the attenuation of the acoustic wave. When the propagation of the acoustic wave (Eq. 1.3) is introduced in the acoustic wave equation (Eq. 1.5) and it is found that q and Ω are related through a dispersion relation as follows [5]:

$$\Omega^2 = q^2(v_a - i\Omega\Gamma) \tag{1.17}$$

that can be rewritten as [5]:

$$q \sim \frac{\Omega}{v_a} + \frac{i\Gamma_B}{2v_a} \tag{1.18}$$

where $\Gamma_B = \Gamma_q^2$ represents the decay rate of the phonon (also known as acoustic damping coefficient). When this expression is substituted in Eq. 1.3, the intensity of the acoustic wave varies as [5]:

$$|\Delta p(z)|^2 = |\Delta p(0)|^2 exp(-\alpha_a z) \tag{1.19}$$

α_a represents the absortion coefficient of the acoustic phonon, and it is given by:

$$\alpha_a = \frac{\Gamma_B}{v_a} \tag{1.20}$$

Using the damping coefficient, Γ_B, the lifetime of the acoustic phonon is given by:

$$\tau_B = \frac{1}{\Gamma_B} \tag{1.21}$$

Due to the attenuation that the acoustic wave experiences, in the frequency domain, Eq. 1.19 becomes a non-monochromatic wave, leading to a Brillouin components that exhibit a Lorentzian spectral shape given by [5]:

$$g_B = g_0 \frac{(\Delta\nu_B/2)^2}{(\nu - \nu_B)^2 + (\Delta\nu_B/2)^2} \tag{1.22}$$

where $\Delta\nu_B = \Gamma_B/2\pi$ is the full-wave half-maximum (FWHM) Brillouin linewidth and g_0 represents the maximum value of the Brillouin gain in the resonance, where $\nu = \nu_B$.

1.2.3. Stimulated Brillouin scattering in optical fibers

As said, when the intensity of the incident optical beam is low, the system works in a linear regime without modifying the characteristics of the medium. As the power of the optical wave is incremented, the system enters in a nonlinear regime leading to a modification of the properties of the medium, obtaining SBS. In Brillouin scattering, the system becomes more efficient when SBS is used. This section will introduce the characteristics of SBS.

When high optical intensities are used in order to stimulate the scattering process, the dipoles of polarization (P) depend on the non-linearities of the electric field (E). Total polarization takes the value [7]:

$$P = \varepsilon_0(\chi^{(1)} \cdot E + \chi^{(2)} : EE + \chi^{(3)} \vdots EEE + ...) \tag{1.23}$$

Where ε_0 is the vacuum permittivity and $\chi^{(j)}$ $(j = 1, 2, 3, ...)$ is the j-th order susceptibility. The principal contribution to P is given by the linear susceptibility $\chi^{(1)}$, which effects are included in both refraction index (n) and optical attenuation coefficient (α). The second order susceptibility $\chi^{(2)}$ is the cause of some non-linear effects as second harmonic generation and the generation of the frequency sum. However, $\chi^{(2)}$ is equal to zero in symmetric molecules as the case of SiO_2. In optical fiber made with SiO_2, $\chi^{(3)}$ is the main source of nonlinear effects such as Kerr effect, third harmonic generator, four wave mixing and stimulated scattering [7]. The polarization field, inducted by the dipoles depends on the electric field [7]:

$$P^{NL} = \varepsilon_0 \chi^{(3)} \vdots EEE \tag{1.24}$$

with the attenuation of the fiber, α, and the nonlinear polarization, P^{NL}. The perturbated wave equation, then becomes:

$$\nabla^2 E - \frac{n^2}{c^2}\frac{\partial^2 E}{\partial^2 t} - \frac{\alpha n}{c}\frac{\partial E}{\partial t} = \mu_0 \frac{\partial^2 P^{NL}}{\partial t^2} \tag{1.25}$$

Electrostriction is a mechanism in which materials suffer a compression when an electric field is applied. The interest of electrostriction lies in that it is a mechanism to generate a third-order non-local optical response and a coupling mechanism to generate SBS [5].

In an optical fiber, counterpropagating signals interfere, generating electrostriction. When detuning frequency between waves is close to the BFS of the fiber, the electrostriction generated in the optical fiber becomes in an acoustic wave. This acoustic wave modulates the refraction index of the fiber, generating a Bragg grating that propagates through the fiber and scatters the pump wave. As the acoustic wave moves along the fiber, parallel to the pump wave, it generates a down-shifter frequency Doppler effect in the scattered wave. In the other direction, it generates an up-shifted frequency Doppler effect. The first case is added to the probe wave as constructive interference, generating a gain over the Stokes wave. In the other case, a depletion over the counterpropagated wave is generated.

From the macroscopic point of view, electrostriction can be explained as the effect a concentration of energy from constructive interference between both counterpropagated waves. This energy depends on the electric field, E, as:

$$U = \frac{1}{2}\varepsilon_0\varepsilon_r E^2 \tag{1.26}$$

where ε_r is the relative dielectric constant of the medium.

From the microscopic point of view, this force develops a dipole momentum over each molecule affected by the electric field. As a consequence, it generates a strictive pressure that can be written as:

$$p_{st} = -\frac{1}{2}\varepsilon_0\rho\left(\frac{\partial\varepsilon}{\partial\rho}\right) < EE > \tag{1.27}$$

where $< EE >$ denotes the time average during an optical period. Due to the negative character of p_{st}, when it is applied a strong electric field, the pressure is reduced leading to a reduction of the density, that can be expressed as:

$$\Delta\rho = -\rho\left(\frac{1}{\rho}\frac{\partial\rho}{\partial p}\right)p_{st} = -\rho C P_{st} \tag{1.28}$$

where the compressibility of the material is written as $C = \rho^{-1}(\partial\rho/\partial p)$. Combining Eq. 1.27 with Eq. 1.28, the equation that is obtainned is:

$$\Delta\rho = \frac{1}{2}\varepsilon_0\rho C\gamma_e < EE > \tag{1.29}$$

As the change in the susceptibility, when an electric field is applied it can be represented as $\Delta\chi = \Delta\varepsilon$, and $\Delta\varepsilon = (\partial\varepsilon/\partial\rho)\Delta\rho$, being $\Delta\rho$ given by Eq. 1.29. The result becomes as:

$$P^{NL} = \varepsilon_0 C_T \chi_e^2 |E|^2 E \tag{1.30}$$

Using Eq. 1.30 in the perturbed wave equation, for both optical waves and taking in consideration the acoustic wave, the couple equation waves for SBS is obtained, as it is shown in the next section

1.2.4. Mathematical model of SBS in single mode fibers

In the Brillouin scattering process, three waves are involved: Stokes wave ($E_s(z,t)$), pump signal ($E_p(z,t)$) and the acoustic wave ($Q(z,t)$). These three waves are coupled and can be modelled (assuming plane waves interactions) by the system of equation that follows [5]:

$$\left[\frac{\partial}{\partial z} + \frac{n}{c}\frac{\partial}{\partial t} + \alpha_p\right]E_p(z,t) = \frac{i\omega_p\gamma_e}{2nc\rho_0}QE_s(z,t) \tag{1.31a}$$

$$\left[-\frac{\partial}{\partial z}+\frac{n}{c}\frac{\partial}{\partial t}+\alpha_s\right]E_s(z,t)=\frac{i\omega_p\gamma_e}{2nc\rho_0}Q^*E_p(z,t) \tag{1.31b}$$

$$\left[-2iq\nu_a^2\frac{\partial}{\partial t}-2i\Omega\frac{\partial}{\partial t}+(\Omega_B^2-\Omega-i\Omega\Gamma_B)\right]Q(z,t)=\varepsilon_0\gamma_e q^2E_p(z,t)E_z^*(z,t) \tag{1.31c}$$

In order to solve the value of $E_s(z,t)$, both numerical integration and analytical methods can be used. In the case of an analytical solution, some simplifications have to be done to considerate a temporal interaction longer than the lifetime of the phonon (τ_p); in that case, temporal derivative in the equations can be negligible. Also, since the acoustic velocity is much smaller than optical velocity, the acoustic wave can be perfectly taken as static. Acoustic wave vanishes after propagation of few optical wavelengths as well, so the temporal derivative in the third equation, 1.31c, can be considered equal to zero. As a consequence, the third equation remains as [8]:

$$Q(z)=\varepsilon_0\gamma_E q^2\frac{E_p(z)E_s^*(z)}{\Omega_B^2-\Omega^2-i\Omega\Gamma_B} \tag{1.32}$$

Due to optical properties of the material, both optical frequencies are almost the same, so they both have the same attenuation ($\alpha_p\approx\alpha_s=\alpha$). With these approximations and using the Eq. 1.32 in Eq. 1.31a and 1.31b, the result becomes:

$$\frac{d}{dz}E_s(z)=-\frac{i\varepsilon_0\omega\gamma_e^2q^2}{2nc\rho_0}\frac{|E_p(z)|^2E_s(z)}{\Omega_B^2-\Omega^2-i\Omega\Gamma_B}+\alpha E_s(z) \tag{1.33a}$$

$$\frac{d}{dz}E_p(z)=\frac{i\varepsilon_0\omega\gamma_e^2q^2}{2nc\rho_0}\frac{|E_s(z)|^2E_p(z)}{\Omega_B^2-\Omega^2+i\Omega\Gamma_B}-\alpha E_p(z) \tag{1.33b}$$

In this system, it can be seen that Eq. 1.33a determines that SBS is a gain process over the probe wave and it depends, basically, on the pump and probe wave intensities. Using $dI/dz=d|A|^2/dz=A^*dA/dz+AdA^*/dz$, and some algebraic manipulation [8], system of equations can be rewritten as a coupled intensity equations as follow:

$$\frac{d}{dz}I_p(z)=-g_B(\nu)I_p(z)I_s(z)-\alpha I_p(z) \tag{1.34a}$$

$$\frac{d}{dz}I_s(z)=-g_B(\nu)I_p(z)I_s(z)+\alpha I_s(z) \tag{1.34b}$$

where the intensity of pump and probe wave are given by I_p and I_s, g_B is the Brillouin gain coefficient (given by Eq. 1.22). If it is assumed that evolution of the intensity of the pump wave is dominated by the optical attenuation of the fiber and the pump depletion is considered negligible [8], Eq. 1.34a can be approximated to $I_p(z)=I_p(0)e^{-\alpha z}$ where $I_p(0)$ is the pump intensity at the input of the fiber. Puting this approximation in Eq. 1.34b, it is obtained:

$$Is(z)=I_s(L)e^{-\alpha(L-z)}exp\left[g_B(\nu)I_p(0)e^{-\alpha z}L_{eff}\right] \tag{1.35}$$

where $I_s(L)$ is the intensity of the probe wave at its input in the extreme end of the fiber ($z=L$) and L_{eff} is the effective length of the fiber, in which a lossless fiber would exhibit the same nonlinear effect as in a real lossy fiber [8], and is given by:

$$L_{eff} = \frac{1 - exp(-\alpha(L - z))}{\alpha} \tag{1.36}$$

The evolution of the intensity of the probe wave is determined by the SBS interaction along its propagation. This interaction generates a gain, and by the optical attenuation of the optical fiber. Although this model has been developed for gain-based BOTDA, the same system presented in Eq. 1.34 is valid for loss-based BOTDA if signs for the Brillouin interaction are changed.

In this section, the physical origin and its mathematical demonstration of the SBS have been explained. In the next section, the use of SBS in optical fiber is developed. This is a particular case, useful in this thesis since optical fiber provides a continuum medium able to generate a distributed sensor.

1.2.5. Distributed optical fiber sensor using Brillouin Scattering

The dependence of the BFS on the perturbation that affect to the fiber: strain and temperature, is used to depelop DOFS. The relation between variation of BFS and strain and temperature is given as follows [9]:

$$BFS(T, \delta\varepsilon) - BFS_0 = A\delta\varepsilon + B(T - T_0) \tag{1.37}$$

where BFS_0 is the BFS measured at a room temperature ($T_0 = 25°C$) and without any strain applied, T is the temperature of the measurement and $\delta\varepsilon$ is the difference in the applied strain. A and B are a constants that determine how is each variation, and are given by [9]:

$$A' = \frac{A}{BFS_0} = \frac{\partial n}{n\partial\varepsilon} - \frac{\partial\rho}{2\rho\partial\varepsilon} + \frac{\partial E_1}{2E_1\partial\varepsilon} \tag{1.38a}$$

$$B' = \frac{B}{BFS_0} = \frac{\partial n}{n\partial T} - \frac{\partial\rho}{2\rho\partial T} + \frac{\partial E_1}{2E_1\partial T} \tag{1.38b}$$

In the system presented in Eq. 1.38, each equation is formed with three elements. The first element for both equations is the elasto-optic and thermo-optic coefficient. The second elements are the strain-induced distortion and thermal expansion, respectively. Finally, the last term in both equations reefer to strain-induced second-order non-linearity of Young modulus and the thermal-induced second-order nonlinearity of Young modulus [9].

When Brillouin interaction occurs between two continuous wave (CW), the resultant Brillouin gain spectrum (BGS) is an integration over all the length of the fiber, but it is not possible to discern the BFS in each location of the fiber. In order to characterize the Brillouin interaction (BFS) in each point of the fiber, several techniques have been developed.

In the next section, the principal techniques used to determine the BFS in each location of the fiber are briefly explained.

1.2.5.1. Brillouin optical correlation domain analysis (BOCDA)

Brillouin optical correlation-domain analysis (BOCDA) technique was presented, for the first time, in 2000 [10]. This technique shows a desirable behavior when a spatial resolution of millimeters in a few meter range is needed.

The fundamentals of this technique are based on the interaction of two waves: pump and probe. They both are identically frequency-modulated following a sinusoidal shape and, in addition, the probe wave is frequency shifted around the BFS of the fiber. Both waves counterpropagate along

the fiber, leading to correlation peaks (due to the Brillouin gain) where is frequency separation is constant in time and equal to the BFS of the fiber. In the other points, where the frequency separation changes in time, the Brillouin interaction is negligible. The spatial resolution and the maximum length of the measurement is defined by the parameters of the modulation such as frequency and depth of modulation.

In essence, this setup presents three limitations. The total time of the measurement increases with spatial resolution. The length that can be measured is limited by distance between two correlation peaks (one period of modulation). Finally, the setup is rather complex.

1.2.5.2. Brillouin optical frequency domain analysis (BOFDA)

This technique, presented in 1996 [11], is based on the measurement of the relation between the amplitudes of probe wave and pump wave in order to obtain the complex transfer function of the fiber. In this technique, two counterpropagating waves are deployed. In one direction, a CW pump wave counter propagates a CW probe wave, which is frequency shifted equal to the BFS of the fiber and amplitude-modulated by a sine-function. The resulting Brillouin interaction of both signals is analyzed by a vector network analyzer (VNA), which is fed by two photodetectors. Finally, the inverse Fourier transform of the frequency response is calculated, giving the Brillouin interaction response in the time-domain of each section of the fiber.

Since the amplitude of the Brillouin interaction depends on the BGS, the spatial resolution achieved by this technique is limited by the low amplitude of the interaction when the acoustic phonon is not excited enough. Also, more distance and high spatial resolution imply a bigger frequency swept and, as a consequence, the measurement time is increased. Although Brillouin optical frequency-domain analysis (BOFDA) has worse performance than other distributed sensors based on Brillouin interaction, a measurement of a fiber link of 5.5 km with a spatial resolution of 3 cm, using a post-processing method, has been achieved [12].

1.2.5.3. Brillouin optical time-domain analysis (BOTDA)

Finally, the technique deployed in this thesis is called BOTDA. This technique was demonstrated for the first time in 1990 for temperature monitoring [13] and is the most used technique in several applications [14, 15, 16]. BOTDA systems are based on two counterpropagating waves, as shown in Fig. 1.2, continuous probe wave and a pump wave with a frequency separation approximately equal to the BFS of the fiber.

During the propagation of the pump wave, an acoustic wave is locally excited. The frequency of the acoustic wave depends on the characteristics of the fiber in each location. Acoustic wave facilitates an energy transfer between both waves through Brillouin interaction. Depending on the configuration, when the optical frequency of the pump wave is higher than the probe wave, the system works in a gain-based configuration, in the opposite case, the system works in the loss-based configuration. After the whole propagation of the pulse along the fiber, the probe wave is detected in the time domain. Then, each time of the probe wave has suffered a gain/loss (depending on the configuration) depending on its interaction with the pump wave. These time-dependences of the variation in the amplitude of the probe wave can be turned into position-dependences over the fiber using the round-trip time relation:

$$z = \frac{c}{2n}t \tag{1.39}$$

where t is the time since pump pulse entered in the fiber and z is the position of the fiber where pulse meets each front wave of the probe wave.

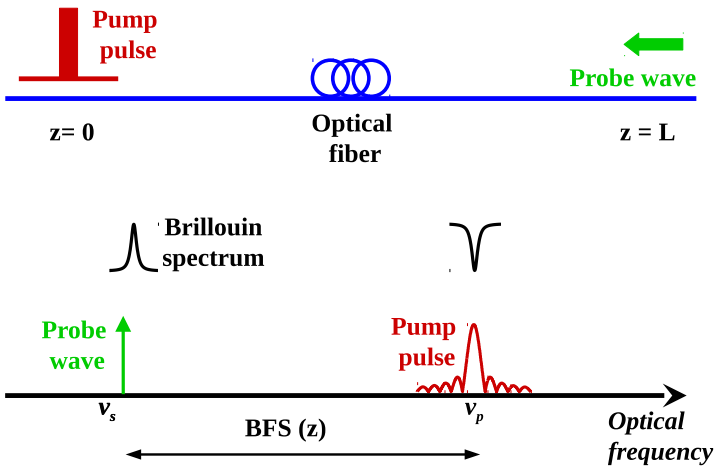

Figure 1.2: Basics of the BOTDA where two waves are counterpropagated through the optical fiber. Probe wave (green) suffers a gain whereas pump wave (red) suffers a depletion induced by Brillouin interaction.

Since the Brillouin interaction occurs throughout an optical bandwidth equal to the Brillouin linewidth, it is necessary to measure the frequency difference at which the Brillouin interaction experiences a maximum gain/loss for each location of the fiber. With this aim, a scan of the frequency difference between the pump and probe wave is done. The distribution of the BGS is reconstructed after the measurement, as shown in Fig. 1.3(a). Finally, as Fig. 1.3(b) the accuracy of the maximum of the BGS is given by the position of the maximum of the fit applied to the spectrum given by Eq. 1.22

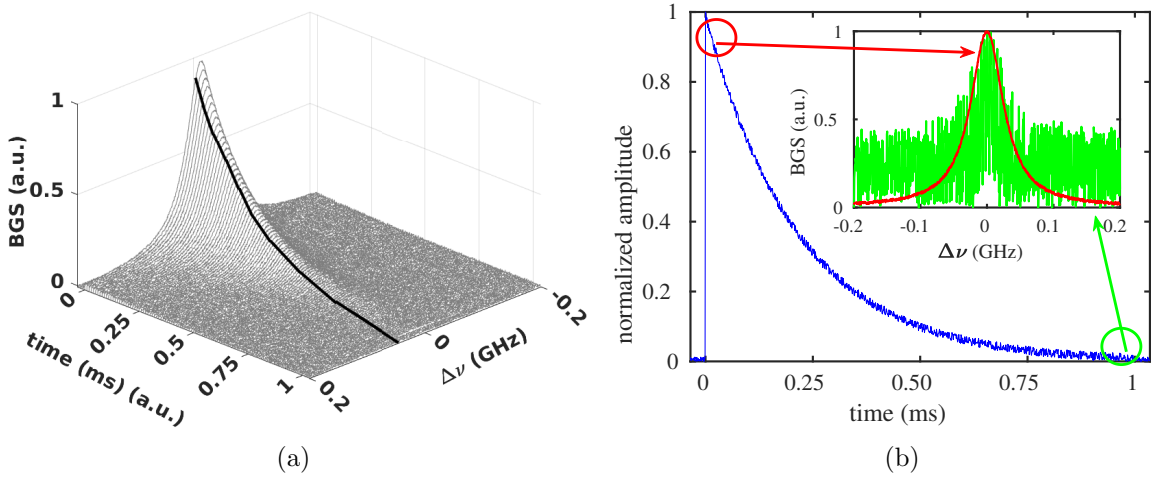

(a) (b)

Figure 1.3: (a)Brillouin specatrum gain along 100-km fiber link. (b) Amplitude of a single frequency marked as a black in (a) figure. Also the BGS at the input (red) and end (green) of the fiber are shown.

1.2.6. Mathematical model of the BOTDA sensors

As said before, in BOTDA sensors probe and pump waves counterpropagate along the fiber. As the pump pulse meets each front wave of the probe wave, there is an energy transfer from the pump pulse to the probe wave (in gain-based configuration). As a consequence, the probe wave experiences an amplification at each location. This amplification can be expressed solving the coupled equations shown in Eq. 1.33

$$\frac{d}{dz}E_p(z) = \left[-\frac{g_0}{2}\frac{i\Delta\nu_B}{i\Delta\nu B + 2\Delta\nu} - \frac{\alpha}{2}\right]E_p \tag{1.40a}$$

$$\frac{d}{dz}E_s(z) = \left[-\frac{g_0}{2}\frac{i\Delta\nu_B}{i\Delta\nu B - 2\Delta\nu} + \frac{\alpha}{2}\right]E_p \tag{1.40b}$$

where E_p and E_s are the optical amplitude fields of the pump and probe wave respectively. The maximum of the BGS is located at a frequency $\Delta\nu = \nu_s - \nu_p + \nu_{BFS}(z)$, being ν_s and ν_p (with $\nu_s < \nu_p$ for gain-based configuration) the optical frequencies of probe wand pump wave and $\nu_{BFS}(z)$ the BFS of the fiber at the location z.

Probe wave and pump wave are introduced in the positions $z = L$ and $z = 0$ of the fiber respectively. If it is assumed that pulsed signals just experiences fiber attenuation because of its propagation, Eq. 1.40a can be easily solved as:

$$E_p(z) = E_p(0)exp\left[-\frac{\alpha}{2}z\right] \tag{1.41}$$

this last equation can be directly used in Eq. 1.40b in order to calculate the gain experienced by probe wave due to the Brillouin interaction, that becomes

$$E_s(z-\Delta z) = E_s(z)exp\left[\frac{g_0}{2}\frac{(\Delta\nu_B/2)^2 - (\Delta\nu\Delta\nu_B/2)}{(\Delta\nu_B/2)^2 + \Delta_\nu^2}|E_p(z)|^2\right] \tag{1.42}$$

where the spatial resolution of the sensor is given by $\Delta z = T_p c/2n$ with T_p the temporal duration of the pulse. Since the duration of the pulse is short enough to considerate that pump pulse does not experience optical attenuation during the interaction, both amplitudes probe and pump waves are kept constant during interaction. Therefore, Eq. 1.42 evaluated in the optical receiver (Rx) turns out as follows:

$$P_s(z)\Big|_{Rx} = P_{s_i}e^{-\alpha L}exp\left[\frac{g_0}{A_{eff}}\frac{(\Delta\nu_B/2)^2}{(\Delta\nu_B/2)^2 + (\Delta\nu)^2}P_{P_i}e^{-\alpha z}\Delta z\right] \tag{1.43}$$

where A_{eff} is the effective area of the fiber. Eq. 1.43 gives the power of the probe wave in any location, that can be simplified if it is assumed that BOTDA sensor works in a small signal regime, giving an expression as follows:

$$P_s(z)\Big|_{Rx} \approx P_{s_i}e^{-\alpha L}\left[1 + \frac{g_0}{A_{eff}}\frac{(\Delta\nu_B/2)^2}{(\Delta\nu_B/2)^2 + (\Delta\nu)^2}P_{p_i}e^{-\alpha z}\Delta z\right] \tag{1.44}$$

where the term inside the bracket represents the power of the probe wave and the gain experienced by the probe wave, which is proportional to the gain coefficient (g_0), pump wave and duration of the interaction [17].

From Eq. 1.44, it can be deduced that in a sensor link that shows a uniform distribution of the BFS, the gain experienced by the probe wave will decay exponentially with the length (position)

of the fiber. However, the case when the distribution of the BFS is not constant, the gain profile will experience a shape different from the exponential decay, in the same way, when the system experiences any nonlinear effects or distributed amplifier [17]. If an ideal case, when it is considered that both waves experience optical attenuation, it is expected that a larger fiber link implies smaller gain experienced by the probe wave at the end of the fiber and, as a consequence, worst SNR. Therefore, the worst-case location in a fiber link sensor will be located at the end of the fiber, and its gain will be given by [17]:

$$P_s(L)\Big|_{Rx} \approx P_{s_i} e^{-\alpha L} + \frac{g_0}{A_{eff}} \frac{(\Delta\nu_B/2)^2}{(\Delta\nu_B/2)^2 + (\Delta\nu)^2} P_{P_i} P_{s_i} e^{-2\alpha L} \Delta z \tag{1.45}$$

In the last equation, the signal at the end of the fiber is twice affected by the optical attenuation. First, by the attenuation of the pulsed pump wave due to its propagation throughout the fiber. Second, by the probe wave that travels all the fiber between its input in the fiber and the receiver.

After the mathematical model of the BOTDA sensors has been shown in the last section, the next section will introduce the principal limitations that BOTDA faces.

1.2.6.1. Limitations of BOTDA sensors

The main aim of BOTDA sensors is to determine the BFS profile of the fiber. The BFS profile is obtained from the peak value of the BGS at each fiber location. The precision of the detection of the BGS peak depends directly on the SNR, which is directly related to the Brillouin gain. As shown in Eq. 1.45, when the powers of both counterpropagating waves are optimized, and the distribution of the BFS along the fiber is uniform, the farthest point from pulse input is the worst-case, where the amplitude (therefore the SNR) is minimum.

There are some factors that limitate the performance, such as the maximum power of waves that can be introduced in the fiber. In the next sections, the principal limitations that the power of each wave experience are explained.

Pump power limitations

As shown in Eq. 1.45, a limiting factor in the Brillouin gain induced over the probe wave is the power of the pump wave. An obvious solution to increasing the Brillouin gain induced over the probe wave is to inject a higher pump power, but it presents a problem related to nonlinear effects such as modulation instability (MI), self-phase modulation (SPM) and Raman dispersion.

MI generates a depletion of the pump wave [18, 19] that impairs the performance of the sensor [20]. MI comes from the combination of Kerr effect and anomalous dispersion in the fiber [21]. Due to MI, two symmetric sidebands next to the optical frequency of the pump wave are generated. The spectrum of these MI sidebands are expressed as [21]:

$$G_{MI}(\Omega_p) = 1 + \frac{\sinh^2\left(2\gamma P_P L \sqrt{\left(\frac{\Omega_p}{\Omega_c}\right)^2 \left(1 - \left(\frac{\Omega_p}{\Omega_c}\right)^2\right)}\right)}{2\left(\frac{\Omega_p}{\Omega_c}\right)^2 \left(1 - \left(\frac{\Omega_p}{\Omega_c}\right)^2\right)} \tag{1.46}$$

where γ is the nonlinear coefficient of the fiber. The power of the pump wave is given by P_P, Ω_p is the frequency of the sidebands around the optical frequency of the pump wave and Ω_c is the cutoff frequency. When the pump wave is launched, there is an exchange energy between the frequency of the pump wave and the sidebands, resulting in a power fluctuation of the pump power.

These fluctuations of the power are translated to the amplitude of the Brillouin gain along the fiber. This leads to a reduction in the precision of the measurement of the BFS at those locations where the amplitude, and hence the SNR, drop.

Before being injected in the fiber, the pump pulse is typically amplified using an Erbium doped fiber amplifier (EDFA). The more the pump wave is amplified, the higher the amplified spontaneous emision (ASE) is generated, which co-propagates with the pulse signal. Furthemore, amplification spontaneous emission (ASE) works as a seed to the generation of MI. However, the use of an optical filter (OF) to limit the spectral bandwidth of ASE can reduce the increased MI due to this effect [17].

The maximum power of pump wave that can be injected into the fiber can be expressed using [21]:

$$P_{max} = \frac{\sigma_{crit}}{2\gamma L_{eff}} \tag{1.47}$$

where σ_{crit} is the critical gain calculated as a function of the noise power spectral density (S_n). The depletion ratio ($R_{D,MI}$) is given by [21]

$$\sigma_{crit} - ln(\sigma_{crit}) = ln(R_{D,MI}) - \left(\frac{S_n}{10} + 9\right) ln(10) + \frac{ln(2)}{2} \tag{1.48}$$

In standard telecommunication fiber, MI typically imposes a maximum pump pulse power of 22 dBm. This limitation can be overcome when dispersion shifted fibers (DSF) are used. However, this kind of fibers have smaller effective areas and lower dispersion that standard SMF. As a consequence, another kind of nonlinear effect such as Raman scattering are induced, deploying the pump wave, and, consequently, limiting the distance of the sensor.

Finally, another nonlinear effect related to the temporal shape of the pump wave plays a fundamental restriction in the performance of the sensor: SPM. In this effect, the intensity of the pump pulse wave modulates the refractive index, generating a phase-shift of the transmitted signal. As a consequence, the spectral bandwidth of the pump pulse is broadened [22]. The effect of the SPM over the instantaneous frequency of the pump pulse can be expressed as [22]:

$$\Delta\omega(\tau) = -\frac{\partial \Phi_{NL}}{\partial \tau} = -\gamma P_{P_i} L_{eff} \frac{\partial}{\partial t} |U(0,\tau)|^2 \tag{1.49}$$

where $U(z,\tau)$ is the normalized pulsed signal. Eq. 1.49 can be understood as any temporal change in the phase leads to a variation of an instantaneous frequency of the pulse from its central frequency (ω_p). This time dependence of the instantaneous frequency has the same effect as a pulsed chirp which chirp amplitude is increased in the distance.

Probe wave limitations: spontaneous Brillouin scattering and NLE.

Another critical factor that limits the performance of the BOTDA sensor is the power of the probe wave, which limits the SNR of the probe wave. But the maximum power of probe wave is limited by NLE [1, 23] and by the spontaneous Brillouin scattering (SpBS) [24]. These both effects introduce noise in the measurement, producing a damage of the SNR.

In BOTDA systems, two counterpropagating waves interact along the optical fiber. The interaction between both waves has a frequency dependence on the BFS of the fiber. It leads to an energy exchange due to the SBS process, leading to a spectral distortion of the pump wave and

resulting in a measurement error. In order to reduce this pulse distortion, the injected probe wave has to be reduced.

In this thesis, two kinds of NLE are studied: first-order NLE and second-order NLE. In chapter 2, their physical origins, and the methods proposed to compensate this effect are discussed and explained.

Another significant restriction on the power of the probe wave is the so-called SpBS. This critical limitation comes from the Brillouin interaction between probe wave and thermal-induced acoustic waves in the fiber. In order to avoid spontaneous amplification, the maximum power of the injected probe wave is limited. This maximum power is given by the so-called Brillouin threshold of the fiber [25]. When optical power exceeds the Brillouin threshold, a significant power begins to reflect that leads to a random depletion of the input probe wave, becoming in a reduction of the SNR. In single-mode fibers, the theoretical limit for a CW probe wave is around 6 dBm [26, 24].

Spatial resolution

As shown in Eq. 1.43, the spatial resolution, Δz depends on the length of the pulse in the fiber that, in turn, is related to the temporal duration of the pulse, T_p, as:

$$\Delta z = \frac{T_p c}{2n} \tag{1.50}$$

This relation between the temporal and spatial length of the pulse is valid for any reflectometry technique.

When a high spatial resolution is required, it is necessary to reduce the temporal duration of the pulse, but this presents a series of problems such as less Brillouin interaction and, therefore, less Brillouin gain over the probe wave, leading to a worse SNR. Moreover, since the linewidth of the BGS becomes from the convolution of the pulse and the natural Brillouin linewidth, the spectrum of the Brillouin interaction is broadened, further than the natural Brillouin linewidth, when pulse shorter that acoustic phonon lifetime is used. This broadening of the Brillouin linewidth leads to a reduction of the accuracy of the determination of the BFS.

Different techniques have been presented in order to overcome the limitation on the pulse length and improve the spatial resolution. Some of them are based on the pre-excitation of the acoustic phonon [27, 28, 29]. Other technique, described in chapter 3, is based on calculating the difference between two BGS generated with pump pulses with different temporal duration [30].

Sensing Range

Another major constrain experienced by BOTDA is the maximum distance that can be measured. As Eq. 1.43 demonstrates, each location of the fiber suffers twice optical attenuation, one due to the whole propagation of the probe wave through the optical fiber and the other because of the pulse propagation between its input and the location where the interaction occurs. The attenuation experienced at the last point of the fiber is twice the optical attenuation of the whole fiber, as Eq. 1.45 shows. As a consequence, the SNR is reduced, and the maximum distance of the measurement is constrained.

In order to minimize this loss of SNR, a number of techniques have been implemented. The first one, and the most simple, is to perform an average measurement that reduces the noise but, in turn, increases the measurement time. Other techniques use distributed amplification of the waves during their propagation in order to compensate for the optical attenuation of the signals.

These techniques, which are fully explained in chapter 3, are based on Raman amplification [31, 32], second-order Raman amplification [33] and distributed Brillouin amplification [34]. Other techniques use discrete amplification [35] or pulse coding techniques [36]. Finally, a technique based on heterodyne detection schema was presented. This technique beats the probe wave with a local oscillator in order to increase the SNR [37].

1.3. Rayleigh Scattering

1.3.1. Rayleigh scattering as a physical phenomena in optical fibers

In contrast with inelastic processes such as Brillouin and Raman scattering, photons in Rayleigh scattering do not experience any exchange of energy during their interaction with the medium. Rayleigh scattering process was discovered by Lord Rayleigh in the 19^{th} Century. It was initially found when studying the origin of the color of the sky, which is due to the small suspended particles that divert the light from its regular course [38]. In particular, in Rayleigh scattering, the size of the particles is approximately a tenth of the wavelength and, besides, it has a strong dependence with the wavelength as λ^{-4} [39].

As an optical wave travels through a medium, there is an interaction of its electric field with the medium. The incident electrical field excites the medium generating an electrical dipole. The oscillating dipole reemits an optical wave with the same frequency of the incident wave but with less amplitude and a phase delay.

This thesis is focused on the use of scattering light to use as a sensor hence the scattering process will be explained from a macroscopic point of view. From the macroscopic point of view, Rayleigh scattering (RS) is based on the coherent superposition of the waves generated by all Rayleigh scatters, located randomly along the medium. In the ideal case of a perfect crystal with no imperfections, reemitted light by all the particles (scatters) have an optical phase that depends just on the position. As a consequence, the phase delay between all the waves is constant in all the directions. This leads to a cancellation of the interference between the multiple scatters in all the directions except forward.

In contrast, a real medium such as optical fiber has imperfections. These imperfections are a consequence of the fabrication process. The origin of the imperfections is thermal fluctuations, which lead to a variation on the crystal structure of the fiber [8, 40, 41]. As a consequence of these variations, the refractive index of crystal variates locally, generating Fresnel reflections. The typical size of these fluctuations is much smaller than the wavelength of the optical wave, becoming a Rayleigh scatter. All the Rayleigh scatters are randomly located, but their location is fixed in the crystal structure.

In this case, the interaction of light with the medium occurs as with perfect media. Nevertheless, now each RS adds an extra phase delay due to the local variation of the refractive index. The variation of phase delay between the set of scattered waves is translated to multiple scattered waves are not in phase between them. It leads to not destructive interference in all directions of the propagation, being part of the optical energy reflected in the backward direction [42, 43]

1.3.2. Use of Rayleigh Scattering as a DOFS

When Rayleigh scattering is analyzed in an enclosed medium, such as al optical fiber (as Fig. 1.4 indicates), part of the scattered light is propagated with an angle that allows leaving the core of

the fiber, losing its guided propagation. Another part of the energy is kept being guided and propagated in a backward or forward direction, as Fig. 1.4 indicates.

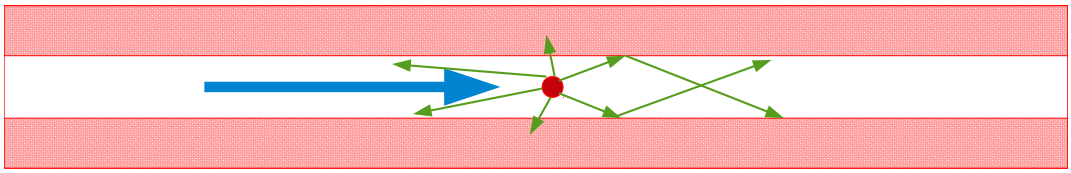

Figure 1.4: Set of scatters and their reflected waves along the length of the fiber.

DOFS, based on Rayleigh scattering, use the analysis of backscattering signal generated when an optical signal is launched into an optical fiber. The red dot in Fig. 1.4 depicts schematically the multiple scatter centers present along the fiber. The incident optical signal, depicted with the blue arrow, excites all the dipoles along the whole length of the fiber. Each dipole reflects a weak amplitude copy of the incident light with a random phase delay, which depends on the local refractive index variation. Finally, the set of reflected waves interfere in their way to the input extreme of the fiber.

The amount of energy that a medium scatters depends directly on both the length of the medium and the wavelength of the used optical signal [38]. In telecom pure silica fiber, the scattering coefficient is around 0.7 dB$km^{-1}\mu m^{-4}$, being reflected an average value of 0.12 dBkm^{-1} of the incident power when third telecom window wavelength, 1.55μm (which fiber presents the minimum absorption) is employed [43].

Depending on the domain of the measurement, main sensors types based on Rayleigh scattering are classified as:

- **OTDR**

  when an optical pulse is launched into the fiber to retrieve the impulsive response of the fiber

- **optical frequency domain reflectometry (OFDR)**

  This system measures the frequency response of the fiber using an optical CW, which frequency is swept along a bandwidth.

1.3.2.1. Incoherent OTDR and OFDR

The basic implementation of the DOFS based on Rayleigh backscattering is schematically depicted in Fig. 1.5. Its aim is to retrieve the optical attenuation of the fiber, $\alpha(z)$, through the measurement of the detected reflected signal $E_t(z)$ [44]. The technique consists of measuring the roundtrip response of the channel (fiber) in order to retrieve the optical attenuation from the measured signal.

The setup presented in Fig. 1.5 is based on the well-known time-domain technique called OTDR. Its operation consists of a waveform generator that controls the intensity that the light source emits. The optical pulsed signal is sent through a circulator to the FUT. In addition, the circulator diverts the backscattering Rayleigh pattern generated in the fiber to the photodetector, where the optical signal is translated to the electrical domain to be digitized and stored by the oscilloscope to be analyzed.

As the pulse travels through the fiber, each Rayleigh scattering center, contained into the length that pulse occupies, reflects a weak copy of the probe pulse. Depending on the coherence

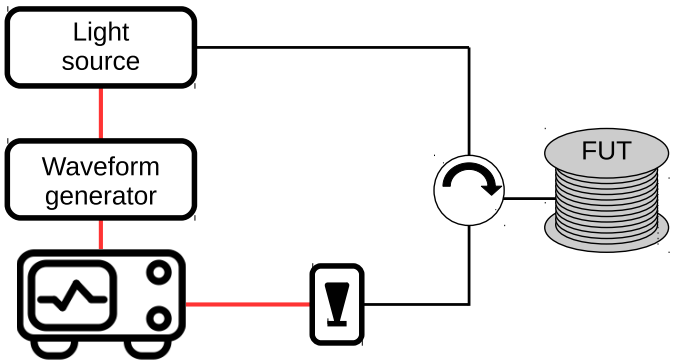

Figure 1.5: Basic setup implemented in a based on Rayleig DOFS.

length of the light source, the addition of the multiple backscattering waves is produced in intensity (incoherent) or in field (coherent). If coherence length is shorter than the length of the optical pulse, the backscattering waves generated inside the pulse are not in phase. As a consequence, all of them are added in intensity. In contrast, when the coherence length of the light is longer than the pulse length, the multiple reflected waves have a constant phase difference between them, leading to a coherent interference.

Fig. 1.6 shows the schematic analysis of an incoherent-OTDR back-reflection. The red line symbolizes a 10-km length optical fiber that has an optical connector and a splice. The black line indicates the intensity of the backscattering signal generated by the optical pulse as it travels through the fiber. In the figure, the interaction of the optical pulse with the connector gives a weak reflection. Also, splice generates an optical attenuation, which is translated to a drop of the reflected intensity.

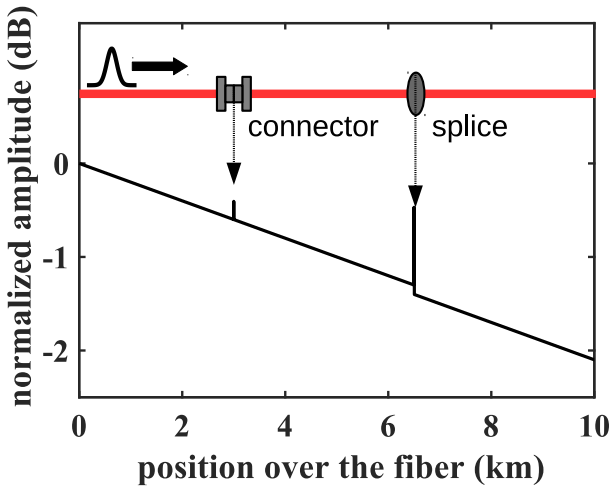

Figure 1.6: Measured signal in a basic OTDR used to retrieve the attenuation of the fiber.

The first time these kinds of OTDR sensors were presented was in 1976 by Barnoski and Jensen [44] to investigate the attenuation characteristics of fiber links. This property was exploited in order to characterize optical fiber links and dynamical events that affect the attenuation of the fiber. To that, the fiber was covered with a metallic coating, inducing an optical attenuation when a perturbation was applied.

For the analysis of the measurement, the position of the perturbation along the fiber is extracted

from the time of the measured backscattering signal. Using the index of refraction of the medium, time and position over the fiber are linked through:

$$z = \frac{1}{2}\frac{c}{n}t \tag{1.51}$$

An important parameter to have in mind regarding OTDR systems is the spatial resolution. Spatial resolution can be understood as the spatial accuracy with which the specific physical field is mapped over the fiber. The duration of the pulse gives the spatial resolution according to:

$$\Delta z = \frac{c}{2n}T_p \tag{1.52}$$

where T_p represents the temporal duration of the pulse.

The sensing range of the measurement is another parameter that characterizes the performance of the DOFS. It determines the maximum distance that can be sensed before the SNR of the backscattering signal becomes so small. Since the maximum sensing range depends on the energy of the pulse, there are two techniques to increase it. The first one is to increase the peak power of the pulse. However, as with BOTDA sensors, this enhancement is limited by the onset of MI. apparition of MI. Another solution consists of increasing the length of the optical pulse since more length implies more energy, but this solution implies a degradation of the spatial resolution according to Eq. 1.52. A solution of these two limitations will be introduced in the next sections and fully explained theoretically and experimentally in Chapter 4.

Alternatively, at the OTDR system, OFDR uses a CW to retrieve equivalent round-trip channel through the measurement of the frequency response of the fiber [45, 46]. Basically, two techniques can be employed to implement an OFDR measurement. The difference between these two techniques depends on the nature of the deployed signals. On the one hand, there is Incoherent-OFDR when a light source with low coherence length is employed [47]. In this technique, the frequency response of the FUT at each optical frequency is obtained by measuring the backscattering signal of the FUT using direct detection in a photo-detector. In contrast, Coherent-OFDR uses a highly coherent CW signal that generates a backscattering signal for each one of the tuned optical frequency along the measured bandwidth. The backscattered signal is beaten with the reference light from the laser generating a coherent interference that is detected by an homodyne receiver. In both techniques, the temporal Rayleigh profile is calculated using the inverse fast Fourier transform (IFFT). In Coherent-OFDR (C-OFDR), in contrast with incoherent-OFDR (I-OFDR), the measured signal is complex. As a consequence, the sensitivity of the system is hugely increased. Since the OFDR technique uses a CW, the spatial resolution that the system achieves depends on the inverse of the bandwidth of the frequency swept, and the SNR is not reduced as the spatial resolution is improved [48, 49]. However, better spatial resolution implies larger bandwidth and, as a consequence, a time-penalty that makes the system unsuitable to perform dynamical measurements.

1.3.2.2. Coherent OTDR

The OTDR sensor described in the previous section uses a non-coherent light source. It simplifies the implementation of the system, although it pays a penalty in terms of sensibility, since the relative phase shifting between the multiple scatters has no effect over the resultant interference of the multiple non-coherent waves. When the used light source has a high coherence length, it presents an intrinsic sensitivity to temperature and strain variations.

DOFS sensors based on coherent interference can be classified according to their frequency or time-domain operation. While C-OFDR sensors can achieve extremely high spatial resolution, coherent-optical time domain reflectometry (C-OTDR) can perform extremely high-frequency measurements, making it possible to implement high-speed dynamic sensors. Since this thesis is focused on developing sensors that provide high sensitivity and frequency sample rate, the explanation of the DOFS based on Rayleigh scattering will be centered in the time-domain.

C-OTDR, also known as ϕ-OTDR is a technique that increases extremely the sensitivity of the sensor when compared with basic OTDR. ϕ-OTDR is based on launching an optical pulse, conformed by coherent light, into the fiber. When the coherence length of light exceeds the length of the pulse, all the backscattered waves that the pulse generates as it travels through the fiber interfere coherently. Due to the highly coherent light, all the scatters centers within the pulse have a constant, but random, phase delay between them. The optical signal that arrives to the photodetector is measured as the summation of all the backscattered waves. As a consequence, the total measured power is not proportional to the summation of individual power of each reflected waves, as in the case of incoherent - optical time domain reflectometry (I-OTDR).

Due to the coherent addition of all the waves, the amplitude along the measurement variates abruptly along the measurement. The phase delay of the waves in some points of the fiber results in constructive interference leading to a strong amplitude. In contrast, in other locations of the fiber, the relative phase delay between the multiple waves results in destructive interference, which leads to a weak measured amplitude. This variation in the amplitude is a well-known limitation that ϕ-OTDR presents and is called fading. The main limitation that fading imposes on the systems is the reduction of the SNR when the signal is weak. A solution of this issue will be presented in the section 1.3.4.2 and chapter 5.

When a perturbation occurs locally over the fiber, the relative positions of the scattering centers are modified, as a consequence, the phase delay between the set of backscattering waves are modified as well. The extreme dependence of the optical phase on an external perturbation is translated to a substantial variation of the resultant amplitude from the coherent interference, which occurs locally over the backscattering pattern when the perturbation is applied.

There are two basic techniques to use a ϕ-OTDR as a sensor: measure either the intensity or the optical phase of the backscattering signals

In a intensity-based ϕ-OTDR setup, the backscattering signal is detected, using a direct-detection in a photodetector, as the square of the electric field. The measured Rayleigh backscattered signal is then power versus time, which can be translated to power versus distance using Eq 1.51. When the optical source wavelength and the fiber are stabilized, the multiple consecutive measured traces do not exhibit changes on their power backscattering profile. This power profile is completely random and unique for each optical fiber and optical wavelength.

When the optical fiber is perturbed, a variation in the phase delay between multiple optical waves reflected around the position of the perturbation occurs. This variation of phase delay is translated to a modification of the pattern of backscattering power. By mean of the comparison of the power profile of the consecutive measurements, a perturbation can be detected. Due to the extremely high dependence of the amplitude on the optical phase delay between the multiple waves, the a minimal is translated to a significant variation of the measured amplitude. However, the resultant amplitude does not vary linearly with the variation of the phase induced by the perturbation. As a consequence, although the perturbation is detected, it can not be characterized. Therefore ϕ-OTDR based on the power measurement technique just provide a simple detection of perturbation, limiting their use scenarios to applications such as the detection of position and speed monitoring of trains [50, 51] or the detection of intrusion [52].

In order to overcome the limitation that ϕ-OTDR power measurement technique presents to characterize the amplitude of the perturbation, several techniques have been presented. These techniques make use of the dependence of the backscattering power profile on the optical wavelength and the refraction index. The basics of the technique consist of launching consecutive pulses with a slight variation of the optical frequency. When a perturbation is applied to the fiber, the backscattering patterns are locally spatial shifted due to the variation of optical phase that the change of refractive index produces. The aim of the variation of optical frequency is to compensate the local spatial shift of optical frequency by mean of neutralizing the variation of optical phase by changing the optical wavelength. From the relation between optical wavelength and refractive index when the position of the power pattern is translated to its original location, the variation of the index of refraction, thus the strain or temperature, can be extracted. This technique has been demonstrated by measuring strain [53], temperature [54] and birrefringence [55]. Although this technique permits to characterize the magnitude of the perturbation, the frequency scan introduces a time-penalty. As a consequence, the maximum frequency sampling of the sensor is limited.

An evolution of this technique was presented in 2016 [56]. This technique employs chirped pulses to measure the variation of strain and temperature in a single shot, without the need to perform a stepped frequency scan. The basics of the technique consist of compensating the shape of the backscattering pattern, that the variation of refractive index produces, by a variation of the optical wavelength. In this case, the frequency variation is applied linearly during the pulse duration. When a perturbation is applied to the fiber, the induced variation of the refractive index generates a longitudinal shift of the trace. Measuring the time separation between two consecutive measurements, the optical frequency shift that generates both identical patterns is obtained and, as a consequence, the variation of the induced refractive index is extracted. Even though, this technique avoids the time-penalty that stepped frequency scan induces, an extremely high oscilloscope frequency sample is needed in order to achieve a high-frequency resolution along the pulse, generating a massive quantity of data.

An alternative to intensity-based ϕ-OTDR, is the phase-recovery OTDR, which is able to measure dynamic perturbations and quantify their magnitude. Since the optical phase variates linearly with the amplitude of the perturbation, this kind of sensor presents a considerable potential in the field of acoustic sensors, which are able to characterize both amplitude and frequency of the perturbation.

1.3.3. Differential-phase OTDR DAS

As described above, measurement of backscattering power trace permits to detect an event that occurs in the proximities of the optical fiber, but this technique does not allow to characterize the magnitude of the event, so power direct detection techniques are not able to perform a DAS. DAS and distributed vibration sensor (DVS) are both used equally to allude to systems employed to measure the variation of the optical phase along the measurement. Phase recovery OTDR offers a suitable technique to determine the characteristics of the perturbation.

When a perturbation is applied over a section of the fiber, the position of the Rayleigh scattering centers is spatially shifted. Then the optical phase of each reflected wave is modified, in a proportional way to the elongation that the fiber suffers, which depends on the amplitude of the perturbation. On the one hand, this has the effect of a random modulation of the resultant backscattering amplitude (which is used in direct detection OTDR techniques). On the other hand, the optical phase of the set of reflected waves that interfere is added linearly, being possible to establish a relation between the resultant optical phase and the amplitude of the perturbation [57].

As the pulse travels through the optical fiber, the optical phase the reflected wave accumulates in a distance ΔL is given by:

$$\Delta\Phi = 2\xi\Delta L\beta \tag{1.53}$$

where β is the propagation constant, ξ is a correction to the optical path length change that accounts for the strain-optical effect and 2 indicates the round-trip of the optical signal through the perturbed region.

When a perturbation, such a pressure wave occurs over the fiber, the length of the fiber is slightly modified. For simplicity and without loss of generality, it is assumed that the perturbation is isolated in the fiber and affects a fiber length equal to Δl. Then, the optical phase before the perturbed region is given by Φ_1. After the perturbed region, the optical phase is given by $\Phi_2 = \Phi_1 + \Delta\Phi_{pert}(t)$, where $\Delta\Phi_{pert}(t)$ denotes the temporal dependence of the optical phase variation due to the perturbation.

In order to extract the phase information related to the perturbation, the phase difference between two points located after and before the perturbed zone, separated a distance known as gauge length (GL) is performed. By this way, in the perturbed area, the differential optical phase that perturbation introduces is given by:

$$\Delta\Phi(z) = \Phi_2(z + GL) - \Phi_1(z) \tag{1.54}$$

The basics to implement differential phase technique is to retrieve the optical phase of the reflected signal. Different techniques have been implemented in order to measure the optical phase.

- **Interferometric phase recovery**

  This technique, presented in [58], uses a conventional basic Φ-OTDR setup, but a Mach-Zehnder interferometer is included before the detection scheme. This interferometer is conformed by two imbalanced fiber segments. The imbalanced length is equal to ΔL, which represents the GL, is calculated. At the output of the interferometer, both path signal interference is directed to a 3x3 coupler, which feeds three photodetectors that are $3\pi/2$ rad shift between them. The combination of these three signals permits to retrieve the evolution of the amplitude and phase of the reflected signal [59, 60].

  The principal advantage of this technique resides on its simplicity since just two more photodetectors and two couplers have to be added to the basic ϕ-OTDR. On the contrary, the Mach-Zehnder interferometer constrains the GL, which can not be modified after the measurement has been performed.

- **Dual-pulse simultaneously fiber scan**

  This technique, proposed by [61], is based on launching two consecutive pulses with an optical frequency slightly shifted. In addition, both pulses are temporally shifted, generating a spatial separation between them. As both pulses travel along the fiber, each one leads to light being reflected at its carrier frequency. When both backscattering signals, from different arrive at the photodetector, the fiber position over the fiber that arrives simultaneously are spatial shifted a distance equivalent to the temporal separation between both pulses.

  When a perturbation occurs between both pulses, the optical phase of the first pulse is modified. As a consequence, the resultant electrical field that arrives at the photodetector changes. The response of the photodetector depends on the square of the interference of both

backscattering signals. The variation of the optical phase is extracted from the variation of the resultant phase-difference between two consecutive measurements.

The main limitation of the previous technique is partially avoided, since the temporal separation between both pulses, which defines the GL, is easily configurable.

- **Phase-shift keying pulse**

  This technique is a modification of the dual-pulse technique presented above. In contrast with the previous technique, in this case, just one pulse is launched simultaneously, into the fiber, but a phase-shift keying is applied during the second half of the pulse [62]. A sequence of pulses with a constant stepped phase variation is sequentially launched. The variation of phase between the multiple pulses remains constant along each sequence. Using the combination of the signal measured from the backscattering of the multiple pulses, the phase difference along the fiber is calculated. Unlike the previous technique, the gauge length in this technique is related to half of the pulse duration. Moreover, since multiple pulses have to be launched, the optical phase variation ,due to the perturbation, between two consecutive pulses can not be significant, limiting the performance of the sensor to measure high-frequency perturbations.

- **Coherent detection phase recovery**

  Finally, using a coherent detection technique, the phase difference is not performed in the optical domain but the electrical domain during the postprocessing stage. It avoids the fundamental limitation imposed by previous techniques related to the predefined GL before the measurement.

  The fundamental of coherent technique is based on launching a single pulse into the FUT. Then, the backscattering signal is beaten, in a coherent detector, with a local oscillator (LO) [63, 64]. From the detection, both amplitude and optical phase of the trace generated by the pulse are obtained. Finally, from the distribution of the optical phase, the phase difference is calculated as a difference of the optical phase of the desired spatial separation as a GL.

  Since coherent detection is the main phase recovery technique employed during this thesis, its advantages and disadvantages, as well as its limitation and how they have been resolved, will be explained in the next section.

1.3.4. Use of coherent detection to recovery the optical phase

As explained, coherent detection allows us to translate the raw distribution of the optical phase along the fiber to the electrical domain, and then, during the post-processing stage, calculate the differential phase according to the desired GL.

Fig. 1.7 depicts schematically the basic setup employed in differential phase-OTDR (dϕ-OTDR) with coherent detection. As in a conventional OTDR setup, the pulse generator (PG) emits an electrical signal that feeds the semiconductor optical amplifier (SOA), which pulses the optical signal that the laser emits. The optical pulse is then sent to the FUT using a circulator. As the optical pulse travels along the FUT, the backscattering signal is diverted to the 90° coherent receiver [64] where a LO signal is introduced directly from the laser. Both optical signals are beaten generating an in-phase (I) and in-quadrature (Q) electrical signals, which are digitized and stored

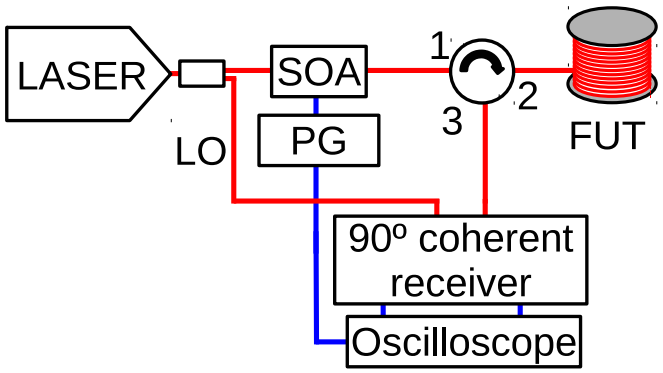

Figure 1.7: Basic setup used to coherent detection.

by the oscilloscope. Using I and Q signals, amplitude and phase of the backscattering signals are obtained as follows:

$$A(t) = \sqrt{I^2(t) + Q^2(t)} \tag{1.55}$$

$$\phi(t) = atan\frac{Q(t)}{I(t)} \tag{1.56}$$

Then, the backscattering phase pattern is reconstructed using the relation between measurement time and position over the fiber, $t = 2z/v_g$ where t is the time since the optical probe signal has been launched into the fiber, z is the position of the fiber ang v_g is the group velocity of the probe wave in the fiber.

$$\Delta\phi(t) = \phi_{z_2}(t) - \phi_{z_1}(t) \tag{1.57}$$

Although this technique needs to change the direct photodetector by a 90° hybrid coherent photodetector and split the optical signal that the laser emits in order to generate the LO, it permits to configure the GL, as $z_2 - z_1$, after the measurement is done, which confers flexibility to the sensor. In addition, a coherent detection scheme permits to increase the SNR [65]. This translates to an extension of the measurement range of the sensor.

The measurement range of the sensor depends directly on the energy contained inside the probe optical pulse. Due to the optical attenuation of the fiber the amplitude of the pulse is reduced, therefore the SNR of the measurement. In order to increase the energy of the pulse, and thus the measurement range, the first parameter that can be modified is the pulse peak power. As the amplitude of the pulse is boosted, its energy is increased. However, This enhancement is constrained by the onset of non-linear effects such as MI and SPM, which results in an effective reduction to the SNR of the measurement. Another possible method to extend the measurement range is to extend the duration of the pulse and thus the energy. Nevertheless, this solution leads to a trade-off since the spatial resolution is linked to the temporal duration of the pulse.

1.3.4.1. Spatial resolution

In order to overcome the trade-off between spatial resolution and SNR of the measurements, some techniques have been presented. One of these techniques consists on using correlation-OTDR [66, 67, 68] although coded-OTDR offers an increment of the sensitivity [69] and enhancement of the SNR [70, 71].

Another technique that breaks the trade-off between spatial resolution and measurement range and, besides, permits to perform dynamical measurements is the pulse compression. This technique was initially developed in the radar environment. Pulse compression technique is based on applying a matched filter (MF) to the backscattering signal generated by a single pulse, which has been FM [72]. At the output of the MF all spectral components of the reflected pulse are merged in the same position, enhancing the SNR.

Another vital issue that limits the performance of the ϕ-OTDR sensors is fading.

1.3.4.2. Fading

The fading problem results in a random variation of the amplitude of the resultant electrical field along the backscattering measured signal. Two different causes may result in fading. Nevertheless the effect over the measurement is the same in both cases. The first origin of fading is the own nature of coherent-OTDR. Due to the high coherence between the multiple backscattering reflected waves, the superposition of all of them may result in destructive interference. As a consequence, the amplitude of the resultant electric field becomes low in a specific positions of the fiber, which is translated to a low SNR, and hence, to unreliable measurements.

In order to combat the effect of Rayleigh fading, a technique that exploits the dependence of the optical phase between waves on the optical frequency was presented [73]. This technique launched a set of pulses with different optical frequencies in order to generate different backscattering traces statistically independent and combine them. With this technique, the position of constructive and destructive interference are spatially shifted, ensuring that a given position will not suffer fading at least for one of the pulses in the set.

The other source of fading is polarization. It is suffered by the systems where two signals with different SOP are beaten in order to recovery the optical phase [64]. When two signals are mixed, the efficiency of the mix depends on the relative SOP between both signals. The SOP of a signal variates randomly along a standard telecom fiber due to its birefringence as its backscattering signal as well. As a consequence, when the backscattering signal is beaten, the signal coming from some positions of the fiber may have an orthogonal SOP relative to the LO, becoming in a low amplitude output signal. The low amplitude implicates low SNR, which is directly translated to an untrustworthy measured value.

In order to reduce the effect that polarization mismatch has over the SNR, some techniques have been presented. The basic idea of these techniques is to measure simultaneously both horizontal and vertical polarizations. With that purpose, the conventional 90° hybrid coherent photodetector is changed by a polarization diversity 90° hybrid coherent photodetector. This device consists of splits the LO signal in both orthogonal polarizations in order to ensure that the backscattering signal is mixed with a parallel and orthogonal SOP [74, 75, 76]. But this technique requires to install a new, more sophisticated detection setup, which increases the complexity of the sensor. Moreover, the generated data, as well as the acquisition and processing hardware is doubled. Another implemented technique consists of install PM fiber in order to keep the backscattering SOP constant. This technique does not permit to employ existent fiber links and, besides, it increases dramatically the cost of the sensors [77].

In chapter 5 of this thesis, a technique that mitigates, simultaneously, both Rayleigh and polarization fading is presented [78]. This technique is based on launching consecutively four pulses with different optical frequencies and a defined relative SOP between them in order to measure at the same time four statistically independent backscattering signals with both possible orthogonal polarizations.

Finally, another problem that constrains the performance of the sensors based on phase recovery is the ambiguity of the phase, which limits the maximum amplitude and frequency of the perturbation that can be measured. Phase ambiguity is not related to a reduced SNR, but to the malfunction of the phase unwrapping technique.

1.3.4.3. Ambiguity of the phase

During the phase recovery technique, the signal at the output of the hybrid 90° coherent photodetector is sampled and digitized by the oscilloscope. After the differential phase is calculated, its phase profile is reconstructed using the unwrap algorithm. Unwrap algorithms by works adding or subtracting multiples of 2π to compensate 2π-jumps of the differential phase. Due to the limitation imposed by phase ambiguity in the unwrap algorithm, the maximum variation of the differential-phase in the same location between consecutive measurements is limited to 2π. This limits the maximum phase change rate that can be mesured, and hence, the maximum amplitude and frequency of the perturbation.

This problem constrains the performance of the sensor in applications where high amplitude and frequency perturbations are analyzed, such as structural health monitoring (SHM) in aircraft wings.

The mitigation of this problem is addressed in chapter 6 of this thesis. The solution presented in [79] develops a system which measures at the same time the phase variation on both axis of a PM fiber. Each axis response is measured in one different polarization using a polarization diversity 90° hybrid photodetector. Then, the phase difference between both polarizations, whose amplitude is proportional to the difference of refractive index between both axis, reduces the rate of phase variation per unit of time. In addition, since both PM fiber axes have a different refractive index, their Rayleigh response is statistically independent. This permits to mitigate Rayleigh fading by the combination of both measured signals.

CHAPTER 2

Non-local effects mitigation by tracking the BFS of the fiber

2.1. Introduction

DURING the last few years, DOFS that make use of Brillouin scattering have been in the focus of research due to their ability to be used as distributed sensors in extremely large distances since they can provide a high precision measurement of temperature and strain. Among all the possible different techniques to implement a distributed sensor based on Brillouin scattering (see section 1.2.5), BOTDA is the technique that offers better performance when an extremely large measurement range is needed.

In this technique, a pulsed pump wave is launched into the FUT, where it interacts with a counter-propagating CW probe. Due to its robustness working with large distance, BOTDA can be a good candidate to be used in several scenarios such as monitoring the integrity of oil and gas pipeline, structural health of bridges and other kind of civil structures, deformation in dams, fire detection in installations such tunnels and a temperature sensor of underwater and underground high power electric cables.

As it has been said in section 1.2.5.3, among the main focus topics of the research on BOTDA sensors is the improvement of the performance of the sensor in order to get the longest distance range without compromising the spatial resolution. One possibility to solve this trade-off is to increase the power of the waves that interact, but this presents some problems linked to the use of high optical powers. When the power of the pulsed pump wave launched into the sensing fiber link is too high, it leads to the generation of nonlinear effects such as MI [21] and SPM [24], therefore the maximum peak power of the injected pump wave is constrain. Another possibility to increase the SNR of the signal that arrives at the optical receiver in long-range BOTDA sensors is to increase the power of the probe wave, but this leads to an increment of the added noise due to the SpBS effect. The other significant effect that limits the optical power of the probe wave is the so-called NLE [1, 23].

This chapter presents the physical sources of the NLE as well as the effects on the performance of the sensor. Besides, a review of the techniques that have been previously used in order the mitigate the start of NLE is presented. Finally, a system developed to mitigate NLE is introduced. This system performs a measurement using a FM probe wave, in which central frequency is locally

adapted to the BFS of the fiber to compensates the second-order NLE due to the variations of the BFS. This system permits us to inject the highest probe wave power that has been ever demonstrated in a BOTDA to our knowledge.

2.2. Sources of non-local effects

As explained in section 1.2.6.1, when BOTDA DOFS are implemented, two optical waves are used: a pump pulsed wave counter-propagates a CW probe. When the optical frequency separation between these both waves is close to the BFS, an interaction between them comes into play, generating an exchange of energy via SBS. Although the physics behind the interaction between both waves is, in its essence, always the same, there are two possibles configurations: gain-based BOTDA and loss-based BOTDA depending on the role that each one of the waves plays.

When a gain-based BOTDA is implemented, the pump pulsed wave, which has a higher optical frequency than the probe wave, transfers energy to the CW. As a consequence, the CW suffers gain, whereas the pump wave experiences a depletion over its spectrum. On the other side, in loss-based BOTDA configurations, the lower optical frequency wave is the pump pulsed wave, and the CW is located a higher optical frequencies. In this case, when the optical frequency detuning between both waves is close to the BFS of the fiber, the CW provides energy, via Brillouin interaction, to the pump wave leading to an attenuation of the CW at the same time that the pump pulsed wave experiences a gain [1].

In BOTDA, the interaction between both pump pulsed wave and probe wave takes place in a length of fiber equal to the pulse length, and the spatial resolution of the system is given by the duration of the pulse. During this interaction, the effect that pulse induces over the CW is very small, as well as the effect that Brillouin interaction has over the pump wave. However, although pump wave interacts with a different front wave along its travel through the optical fiber, the different front waves of the probe wave interact over the same pump pulse wave, exchanging a small quantity of energy with the probe wave in each position of the fiber. After the pump wave has traveled all the optical fiber, the integration of all the small interactions becomes in a significant gain/loss (depending on the configuration of the BOTDA) over the pump pulsed spectrum. This phenomenon is proportional to the length of the fiber, so more fiber length becomes in a more significant exchange of the energy of the pump pulse. The consequence of the accumulation of energy in a part of the spectrum of the pulse, due to its Brillouin interaction with probe wave, results in a distortion of the pulse shape.

To understand the physical phenomena behind the pulse distortion due to Brillouin interaction, the optical power of the pump pulse at the end of the fiber has to be calculated. With that purpose, the model of Brillouin interaction between two coupled waves (Eq. 1.40) is used. Without a loss of generality, the gain-based BOTDA is studied. In the other case (loss-based BOTDA configuration), the signs of Brillouin interaction of the model have to be exchanged, but the fundamentals of the system does not change [1]. As said before, pump pulse interacts with a different front wave of the probe wave in each location of the fiber, so it can be perfectly assumed that the probe wave is just subject to the optical attenuation of the fiber. Therefore, the interaction model between the fields of both waves can be described as:

$$E_p(L) = E_p(0)e^{-\frac{\alpha}{2}L}exp\left[-\frac{g_0}{2}\frac{(\Delta\nu_B/2)^2 - i(\Delta\nu\Delta\nu_B/2)}{(\Delta\nu_B/2)^2 + \Delta\nu^2}|E_s(L)|^2 L_{eff}\right] \tag{2.1}$$

where the field of the pump wave is given by $E_p(z)$, with $z = 0$ and $z = L$ for the input and output of the fiber, respectively. The peak Brillouin gain coefficient is represented by g_0, $\Delta\nu_B$ references to FWHM Brillouin linewidth. The frequency detuning between the probe wave and the pump wave is represented by $\Delta\nu$. The probe wave, injected into the fiber at the extreme end ($z = L$), is denoted by $E_s(L)$. Finally, $L_{eff} = (1 - exp(-\alpha L))/\alpha$ indicates the effective length of the fiber. Despite what it might seem, the amount of energy that the pulse wave exchanges is not significantly increased with the fiber lengthabove L_{eff} the amount of depletion of the pulse wave stabilizes when the length of fiber exceeds $L_{eff} \approx 22km$ (for $\alpha = 0.2dB/km$).

From Eq. 2.1, that describes the evolution of the amplitude of the field of the pump wave, the power of the pump wave of the output of the fiber can be deduced as:

$$P_p(L) = Pp(0)e^{-\frac{g_B(\Delta\nu)}{A_{eff}}P_s(L)L_{eff}}e^{-\alpha L} \tag{2.2}$$

where the power of the pump wave at the input of the fiber is given by $P_p(0)$, A_{eff} denotes the effective area of the fiber, g_B the coefficient gain of the Brillouin interaction, that has a dependence on the frequency detuning between probe and pump wave. $P_s(L)$ indicates the power of the probe wave at its input of the fiber ($z = L$).

Notice that Eq. 2.2 denotes that the depletion of the pulse has a frequency dependence given by the natural Lorentzian response typical of Brillouin interaction. In this case, the depletion of the pulse has its maximum value (given by the peak value of the Brillouin interaction) when the frequency separation between both signals is equal to the BFS of the fiber.

When the fiber has a constant BFS along all its length, the disminution in the energy that the pump pulse suffers after its journey along the whole fiber, for a specific frequency detuning, can be given as a dimensionless deplection factor, d [1]:

$$d(L, \Delta\nu) = \frac{P_p^o(L, \Delta\nu) - P_p(L, \Delta\nu)}{P_p^o(L, \Delta\nu)} \tag{2.3}$$

where P_p^o represents the pump pulse power at the end of the fiber in absence of Brillouin interaction. It also can be understood as the effect that optical attenuation of the fiber has over the pump pulse. If Eq. 2.2 is sustitute in Eq. 2.3, the depletion factor is obtained as follows:

$$d(L, \Delta\nu) = 1 - e^{-\frac{g_B(\Delta\nu)}{A_{eff}}P_s(L)L_{eff}} \tag{2.4}$$

Notice that the coefficient that determines the depletion of the pulsed wave in each frequency has a unique dependence, for each frequency and length of the fiber, with the power of probe wave that is injected into the fiber, so more power of probe wave translates to more loss that is induced over the spectrum of the pump wave. Also, notice that there is not a dependence of the depletion neither on the duration of the pulse nor on the power itself. Using Eq. 2.4, the maximum power of the probe wave that induces a given depletion coefficient over the pump pulse wave can be calculated as:

$$P_s(L) = -\ln(1 - d(L, \Delta\nu))\frac{A_{eff}}{g_B(\Delta\nu)L_{eff}} \tag{2.5}$$

A schematic depiction of the effect that depletion has over the pump pulse spectrum is shown in Fig. 2.1. This figure assumes a constant BFS along the fiber with a slight variation in a small section at the end. As it has been shown in Eq. 2.4, the depletion factor that the pump wave suffers depends on the frequency separation between pump and probe wave [1]. Consequently of the depletion that pump wave suffers, the Brillouin spectrum suffers a distortion resulting in peak

gain shifting and, consequently, a measurement error of the BFS. That is because of, as explained in section 1.2.5.3, the Brillouin gain, that pump wave experiences after its travel through the optical fiber, is given by the integration, along the fiber, of each local Brillouin interaction, as it is described as follows:

$$G_k = e^{\int_{z_k}^{z_k+\Delta z} \frac{g_B(\Delta\nu)}{A_{eff}} P_p(0) e^{-\alpha z_k} dz} \tag{2.6}$$

in this equation, the local region where the interaction occurs is given by Δz, which corresponds to the spatial resolution of the sensor, given by the pulse duration.

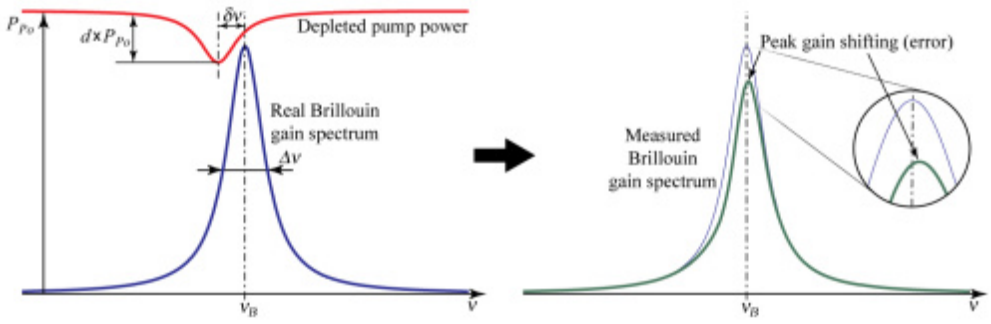

Figure 2.1: Effect of a non-uniform frequency distribution of the pump pulse power on the measurement of the Brillouin gain spectrum: if the pump power is reduced by a fraction d at a given frequency and a Brillouin gain spectrum is analyzed with a peak gain frequency shifted by $\delta\nu$ from this given frequency, a distorted Brillouin gain spectrum will be measured, as shown on the right (thick solid line). The measured peak gain frequency is shifted with respect to the real gain spectrum (thin solid line) and suffers from a systematic error. ©2013 Optical Society of America [1].

This dependence of the depletion on the frequency becomes in a distortion of the pulse. It leads to an offset in the frequency of the measured BFS. As Fig. 2.1 shows, the peak of the Brillouin spectrum is biased to high frequencies when a gain-based BOTDA configuration is used, while the shift of the peak of the Brillouin spectrum is moved to low frequencies when loss configuration is deployed [1].

It is useful to mention that this error induced in the measured value of the BFS is known as NLE. This error generates, in a located position of the fiber, a depletion over the pump pulse. That depletion is generated in other locations of the fiber. This makes the Brillouin interaction in a location of the fiber, to be conditioned by the interaction that pump wave had with probe wave in the previous locations of the fiber.

As said before, both the variation on the BFS ($\delta\nu$) and depletion factor (d) influence the measurement error due to the pump pulse depletion (ν_e). Assuming an error in the BFS smaller than FWHM of the gain spectrum and a depletion coefficient not so big, $d < 0.2$, the error in the measurement of the BFS, induced by the depletion of the pump wave, is given by [1]:

$$\nu_e \cong \frac{d\delta\nu}{\left(1+4\left(\frac{\delta\nu}{\Delta\nu_B}\right)^2\right)^2 - 2d\left(1+2\left(\frac{\delta\nu}{\Delta\nu_B}\right)^2\right)} \tag{2.7}$$

If a constant depletion coefficient, δ, is fixed, the frequency shift of the BFS at which the error

is maximized is given by:

$$\delta\nu = \sqrt{\frac{2-d}{28}}\Delta\nu_B \approx \underbrace{0.26\Delta\nu_B}_{d\ll 1} \tag{2.8}$$

From the equation 2.8, it is deduced that the maximum error in the measured BFS at the end of the fiber, occurs when its BFS, has a difference around a quarter of the FWHM of the gain spectrum with respect to the constant BFS along the rest of the fiber. Furthermore, as Eq. 2.7 shows, the depletion factor, and the error in the determination of the BFS are linked, so more depletion leads to more measurement error. This dependence is shown in Fig. 2.2. To that, a a fiber link with a constant BFS and a variation, equal to $\delta\nu = \Delta\nu_b/4$, in the last section has been simulated. An error no bigger than 1 MHz in the BFS and a maximum epletion coefficient of $\delta \approx 0.2$ have been imposed as well [1]. With these parameters and the restrictions imposed in order to not beat the maximum error in the measurement of the BFS, according to Eq. 2.5, the maximum power that can be injected at the extreme end input of the fiber is -11 dBm. Finally, as in a conventional BOTDA, the Brillouin gain is reduced by a factor 1/2 due to the random relative SOP between both probe and pump waves [80].

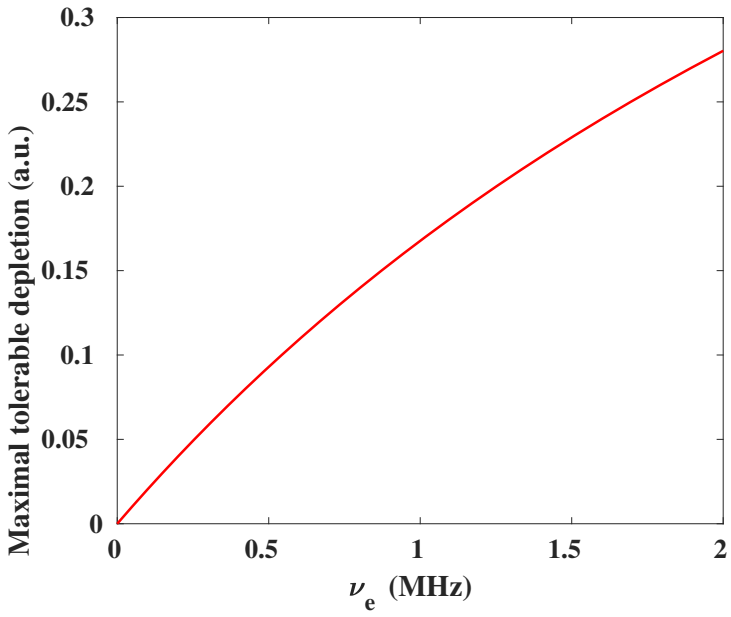

Figure 2.2: Maximal depletion in function of the error of the BFS for the worst-case scenario.

2.2.1. Previous techniques used to avoid NLE

As it has been explained in the section 1.2.5.3 several effects impair the performance of the BOTDA systems, but NLE is one of the main. Due to the limitation on the probe wave, that can be injected into the fiber, that this effect imposes, in order to limit the error on the measurement of the BFS, the SNR that BOTDA devices can achieve is severely limited. That is the reason that, in the last few years, several groups have focused their research on looking for techniques that mitigate that problem. In this section, a brief review of the main solutions, developed in order to hit NLE, is presented.

One of the first methods that was developed did not require to make changes in the experimental setup. It was oriented to do a numerical reconstruction of the BFS measurement [81]. This technique used an algorithm to reconstruct the profile of BFS based on a multidimensional algorithm to find coefficients that parametrize the unknown profile of the BFS. This method was satisfactory demonstrated over a measurement of a fiber of 7 km where NLE were avoided. Although this technique demonstrated to be useful, it needed a previous knowledge of the fiber characteristics. Besides, the time needed to perform the post-processing of the data makes this technique not suitable for most realistic scenarios.

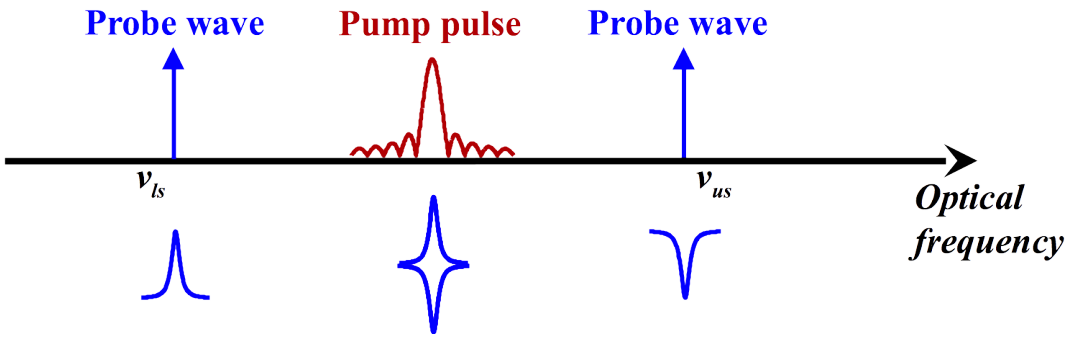

Figure 2.3: Basic of Brillouin interaction between probe waves and pump pulsed wave when two probe waves are deployed in a BOTDA sensor.

After this technique, a technique that deploys two probe waves was presented [82]. Both probe waves are arranged symmetrically in frequency around the pump pulse. This setup makes use of both waves in order to generate a complementary Brillouin interaction with the pump pulse. In this way, while the probe wave located at higher frequencies, generates gain over the pulse, the probe wave (at lower frequencies) contributes to the system generating a loss. The fundamental of this technique is shown in Fig. 2.3, where it displays how the higher frequency probe wave transfers energy (following a Lorentzian profile) to the pulse whereas lower frequency probe wave contributes to the pump spectrum with a Lorentzian shape loss, typical of the Brillouin interaction. As a consequence, both interactions over the pump pulse are completely, or almost completely, compensated, leading to no depletion of the pulse. It is important to note that both probe waves are launched at the same time into the fiber. They both are co-propagated, so both arrive at the photodetector at the same time. For this reason, one of them has to be filtered out, before the detection, in order to perform a measurement.

Notwithstanding, this mutual compensation between both interactions can be accepted partially since it does not take into account the effect that interaction has over both probe waves: amplification of the Stokes wave and loss in the anti-Stokes wave. If Brillouin interaction between these three waves (both probe waves and pump wave) is studied in detail, it is proved that, even though depletion over the pulse is highly mitigated, there is pump depletion yet since both waves that are interacting simultaneously with the pulse are unbalanced due to the interaction itself [1]. When it is considered that power of low-frequency probe wave ($P_{SL}(z)$) and high-frequency probe wave ($P_{SU}(z)$) Eq. 2.2, that describes the pump power at the output of the fiber, can be given as [1]:

$$P_P(L,\Delta\nu) = \frac{P_P(0)e^{-\alpha L}}{1+\frac{g_B(\Delta\nu)^2}{A_{eff}^2}P_P(0)\left[P_{SL}(L)+P_{SU}(L)\right]e^{-\alpha L}\Delta z L} \tag{2.9}$$

at the output of the fiber, $z = L$, the depletion that pump pulse experiences can be calculated using Eq. 2.9 in Eq. 2.3 as:

$$d(L, \Delta\nu) = 1 - \frac{1}{1 + \frac{g_B(\Delta\nu)}{A_{eff}^2 P_P(0)[P_{SL}(L)+P_{SU}(L)]e^{-\alpha L}\Delta z L}} \tag{2.10}$$

note that, from Eq. 2.10, the maximum depletion when dual probe wave is used, in contrast with one probe wave BOTDA, occurs when $L = 1/\alpha$. Besides that, the dependence of the depletion in function of the pulse can be obtained. There is a dependence on the depletion with both pulse peak and pulse duration. More power and/or duration implies a bigger depletion coefficient of the pulse. With the same purpose that Eq. 2.5, the maximum power of the probe waves, for a given depletion coefficient, is given as follow:

$$P_{SL}(L) + P_{SU}(L) = \frac{d(L, \Delta\nu)A_{eff}^2}{g_B(\Delta\nu)^2 P_P(0)(1 - d(L, \Delta\nu))e^{-\alpha L} u L} \tag{2.11}$$

from this equation, the maximum power that probe wave in a long-range dual-probe BOTDA sensor ($L = 1/\alpha$) when a pulse of 10-ns and a maximum peak power before generating MI, 20 dBm [21], is found to be approximately 10 dBm per side-band (13 dBm in total). As said before, the depletion factor depends on the power and duration of the pulse, as for 50-ns pulse duration, with the same peak power, the maximum power of the probe waves drops up to 6 dBm in total (3 dBm per side-band). Although depletion of the pulse becomes dependent on pulse characteristics when two side-bands are used, this method presents a significant improvement in the performance of the sensor, compared to the BOTDA sensor with just one side-band.

2.2.2. Onset of second order NLE

Second-order NLE are due to the spectral distortion of the pump pulse signal when it continuosly interacts with the Brillouin spectra induced by the two probe waves deployed in NLE-compensating BOTDA sensors [23]. As depicted in Fig. 2.4(a), the use of two probe waves equally spaced from the pulsed pump signal by the BFS of the fiber is enough to solve the problem of first-order NLE, since the Brillouin gain spectrum generated by one of the probe waves upon the pulsed signal is canceled out with the Brillouin loss spectrum induced by the other probe wave. However, during the scanning process used to retrieve the Brillouin spectrum, the frequency spacing of both probe waves from the pump is shifted. As a consequence, the Brillouin spectra generated by both probe waves do not longer overlap over the pulsed signal, inducing an spectral distortion of the pulse, as it is schematically depicted in Fig. 2.4 (b) and (c). The onset of this spectral distortion effectively limits the maximum probe power to around -3 dBm for typical long-range BOTDA systems [23].

2.2.3. Techniques to avoid second order NLE

As said before, the conventional scan process of the Brillouin interaction in an optical fiber with two probes, that are moved in frequency symmetrically, presents a substantial limitation in the power of the probe bands due to the second-order NLE [24, 23].

In order to solve the limitation set by the described second-order NLE several solutions have been proposed [2, 83]. One solution is to maintaining a constant frequency difference between both probe waves during the scanning process, which should be fixed to twice the BFS of the fiber as depicted in Fig. 2.5(a) [2]. However, whenever the BFS varies along the fiber, the Brillouin

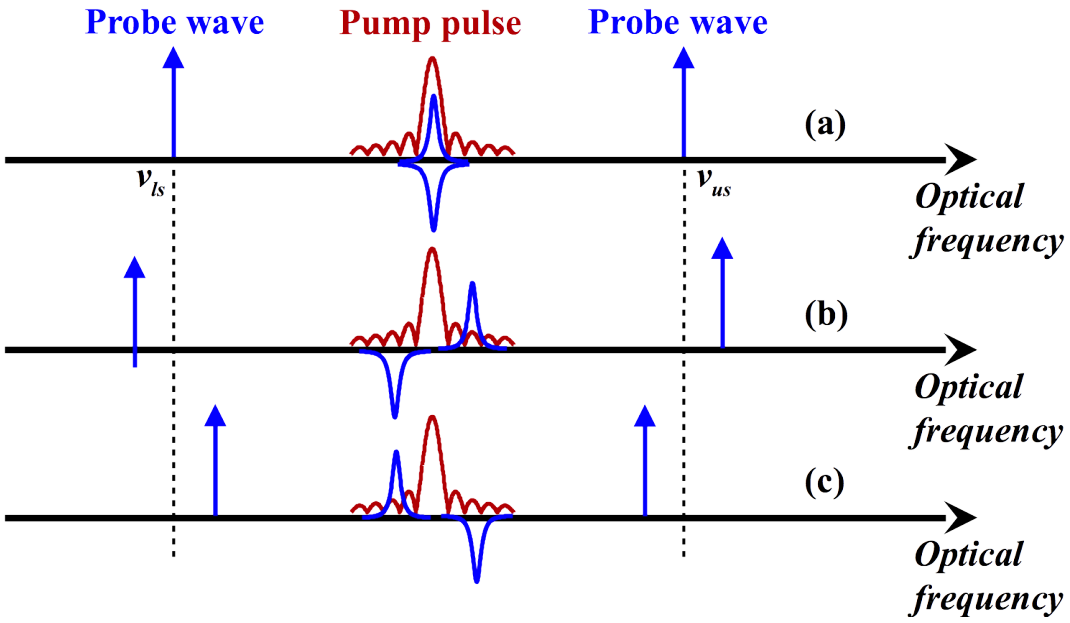

Figure 2.4: Stimulated Brillouin scattering (SBS) interaction between both side-bands probe waves and pump pulsed wave in BOTDA sensor when frequency separation from pump wave to probe waves is equal to the BFS (a), higher than BFS (b) and lower (c).

gain and loss spectra generated by the probe waves do not longer overlap giving rise to a non-flat transfer function over the pulsed signal as it can be observed in Fig. 2.5 (b) and (c). Moreover, as it is analyzed below, this issue can not be solved in general by adjusting the probe spacing using the average BFS of a particular portion of the fiber, for instance, to the BFS of the so-called effective length from the probe input end. The Brillouin gain and loss is so large due to the powerful probe wave injected into the fiber that even when the probe wave has been greatly attenuated by the fiber propagation, the interaction between the pump and probe wave can still introduce significant spectral distortion on the pump pulse spectrum [83].

The solution that we proposed to overcome second-order non-local effects is based on the frequency modulation of the optical probe waves [3]. The Brillouin spectral interaction induced on the pulse in this technique is schematically depicted in Fig. 2.6. As it is shown, the frequency modulation of the optical probe waves broadens the total Brillouin interaction experienced by the pulsed signal [3]. Adjusting the average frequency of both probe waves to the BFS of the fiber, both spectra cancel out leading to no distortion of the pulse. However, as in the previous case, if there is a section of the fiber that has a different BFS, both interactions shift and hence, the pulse becomes affected by a non-flat transfer function, as shown in Fig. 2.6. Notice that the influence of the Brillouin interaction over the pulsed signal is going to be less significant with our method based on frequency-modulated probe waves that the one deploying constant frequency separation between the probes, since the frequency modulation spreads the energy of the interaction into a larger frequency region, thus, reducing the amplitude of the transfer function. However, there is still some distortion of the high frequency components of the pulse that, as it is shown below, limits the maximum probe power that can be deployed in links with BFS variation along the fiber.

In summary, we have qualitatively shown that all techniques available so far to compensate second-order NLE require the fiber to have a fairly uniform BFS along its length. The use of fiber with varying BFS characteristic leads to a residual second-order NLE that may affect the pulsed

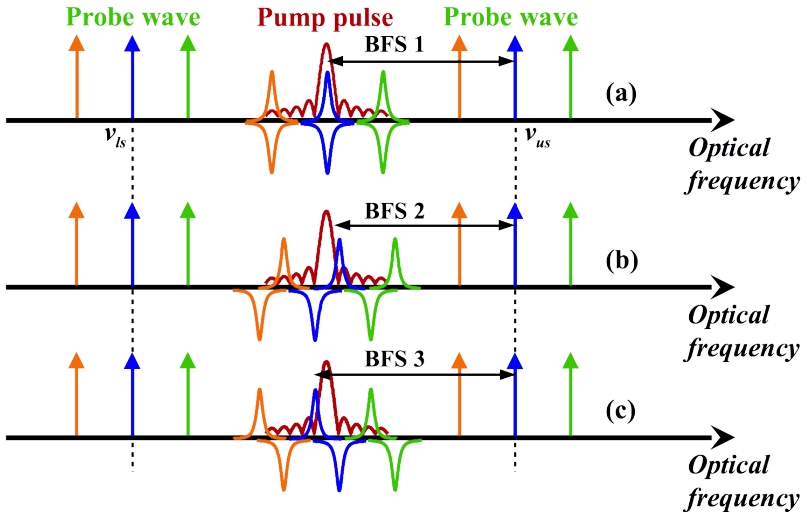

Figure 2.5: Brillouin interaction over the spectrum of the pump wave when frequency separation between both probe waves is (a) equal to the BFS, (b) larger than the BFS and (c) smaller than the BFS.

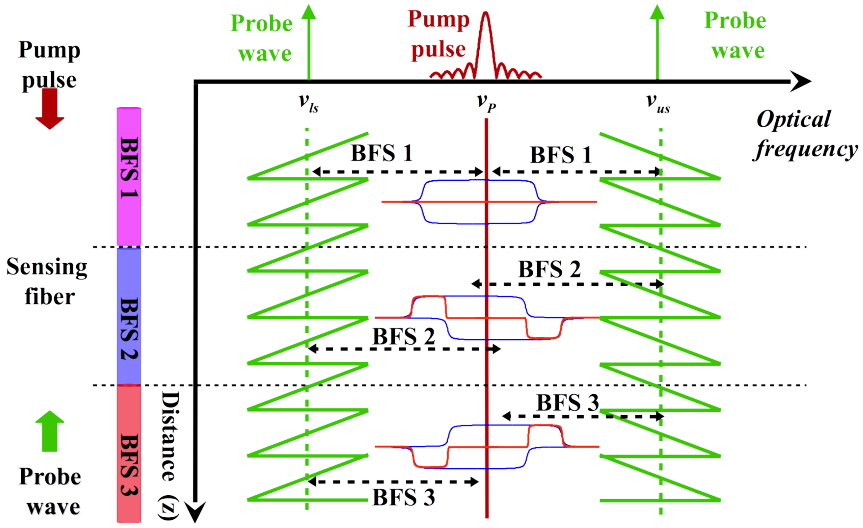

Figure 2.6: Brillouin interaction over the spectrum of the pump wave in BOTDA sensors when frequency modulation is applied. When average central frequency deviation of the probe wave fits the BFS of the fiber (BFS1), BFS is larger than the average frequency detuning between pump and probe wave (BFS2) and when BFS is smaller than the central frequency of the FM (BFS3).

signal. In order to quantify this effect we can solve the differential equations governing Brillouin interaction between the pump pulse and the probe waves assuming that the intensity of the probe waves along the fiber is not affected by the pump wave interaction [7]. This gives the expression of the pump pulse propagating along the fiber:

$$P_p(z) = P_p(0)exp\left[P_{us}(0)\int_0^z \frac{g_b(\Delta\nu_{us})}{A_{eff}}e^{\alpha z}dz - P_{ls}(0)\int_0^z \frac{g_B(\Delta\nu_{ls})}{A_{eff}}e^{\alpha z}dz\right]e^{-\alpha z} \tag{2.12}$$

where $P_p(0)$, $P_{us}(0)$ and $P_{ls}(o)$ are the power of the pump wave, and upper and lower frequency probe waves, respectively, at the input of the fiber, α is the fiber attenuation, A_{eff} is the effective area, and g_B is the Brillouin gain or loss spectra at each location, z, that depends on the local frequency detuning $\Delta\nu_{us}$ and $\Delta\nu_{ls}$, respectively, given by:

$$\Delta\nu_{us} = \nu_p + \nu_{us}(z) - BFS(z) \tag{2.13}$$

$$\Delta\nu_{ls} = \nu_p - \nu_{ls}(z) + BFS(z) \tag{2.14}$$

where ν_p, ν_{us} and ν_{ls} are the optical frequencies of pump, and upper and lower frequency probe waves, respectively, and BFS is the Brillouin frequency shift in each location of the fiber. The solution in Eq. 2.12 assumes pulses with a duration longer than the acoustic phonon lifetime ($\sim$ 10 ns).

As an example of the distortion brought by second-order NLE in non-uniform BFS fiber links, we use the model in Eq. 2.12 to calculate the spectral distortion of the pulse in a link with the BFS distribution shown in Fig. 2.7. The fiber link comprises two consecutive 50-km fiber sections with 10.8 and 10.79 GHz and another fiber section of 20 km with a BFS value, again, of 10.8 GHz. This is quite a realistic scenario in which two types of fibers with slightly different BFS due to fabrication or cabling are deployed in a link.

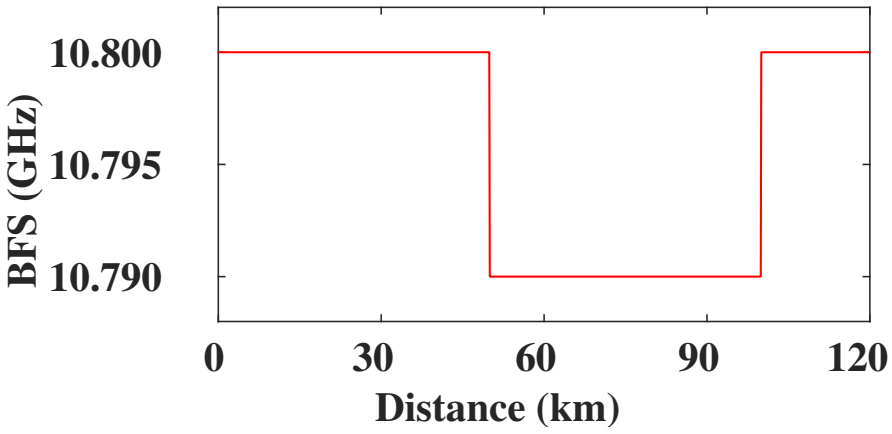

Figure 2.7: BFS distribution used in the simulation.

The total transfer function due to Brillouin interaction experienced by the pulsed signal when injecting different probe power levels in the link is calculated when using either the technique

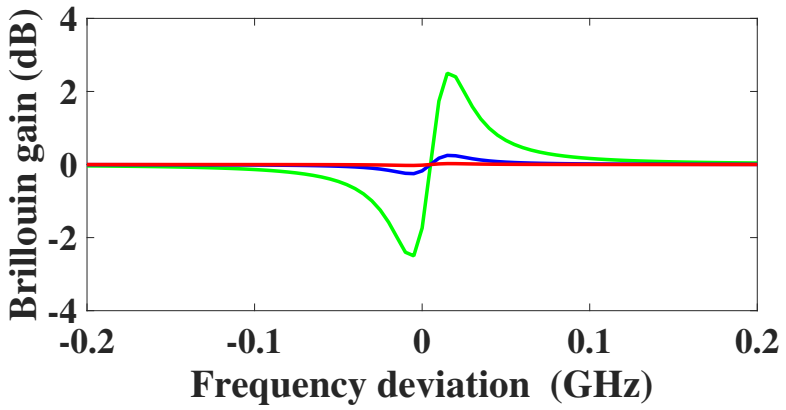

(a)

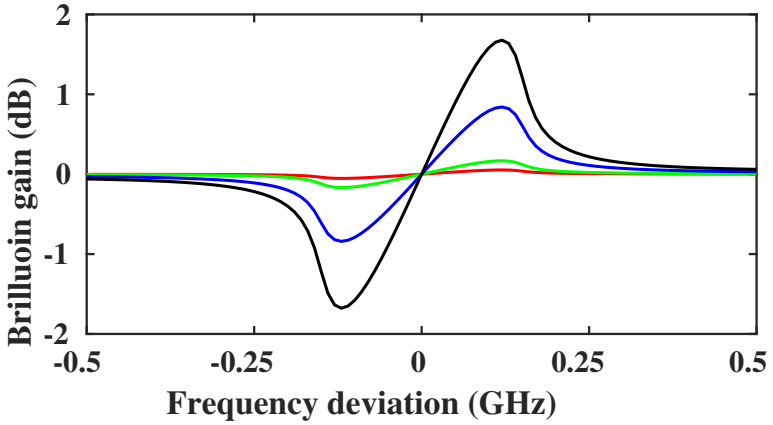

(b)

Figure 2.8: Transfer frequency function due to the Brillouin interaction using the system presented in (a) [2] with power of probe waves -15 dBm (magenta), -5 dBm (cyan), 0 dBm (red) and 5 dBm (green). Plot (b) displays the frequency transfer function presented in [3] using power of probe wave equal to 0 dbm (red), 5dBm (green), 12 dBm (blue) and 15 dBm (black).

for second-order NLE compensation deploying two probes with constant frequency spacing during the spectral scanning (Fig. 2.8(a)), or our method with frequency modulation of the probe waves (Fig. 2.8(b)). Note that the horizontal axis represents the frequency deviation from the central frequency of the pulse spectrum.

In both systems, the peak-to-peak frequency deviation of the probe waves is 300 MHz and the frequency of the probe waves for perfect compensation of second-order NLE is set assuming a BFS value of 10.8 GHz, which is predominant in the fiber, particularly in the first 20-km section at the probe wave input end. The first fact that the calculations in Fig. 2.2.3 highlights is that adjusting the probe wave frequencies taking into account just the BFS of a section of the fiber approximately equal to its effective length is not sufficient to get rid of second-order NLE. Indeed, the calculations display significant spectral distortion of the pump pulse spectra even at moderate probe powers. In addition, the calculations in Fig. 2.8 also highlight that the technique for second-order NLE compensation using frequency modulation of the probe waves is more tolerant to BFS variation than the method using probe waves with constant frequency spacing: at equal power level the amplitude of the spectral distortion is much lower. Up to 10 dB larger probe power can

be deployed with the frequency modulation method for same-order distortion. As it was explained before, this advantage is due to the spreading of the interaction upon the pump pulse into a large frequency region brought by the frequency modulation of the probe, which reduces the maximum level of distortion experienced by the pulse.

2.3. Compensation of second order NLE by tracking the BFS of the fiber

We propose a novel method to solve the limitation on probe wave power imposed by the non-uniformity of the BFS along the fiber in BOTDA setups that compensate second-order NLE. This method is based on dynamically tuning the optical frequency of the probe wave so that it tracks the changes in BFS along the fiber. This is achieved by introducing an additional optical frequency modulation to the probe wave. A schematic of the fundamental of this new technique is depicted in Fig. 2.9. As it can be observed a frequency shift is added to the probe wave optical frequency modulation. This added frequency shift must be set so that the average frequency of the probe waves matches the average BFS of each section of the fiber. Therefore, the gain and loss spectra induced by both probe waves on the pump pulse frequencies cancels out at each section of the fiber so that the spectral distortion that was analyzed above is avoided.

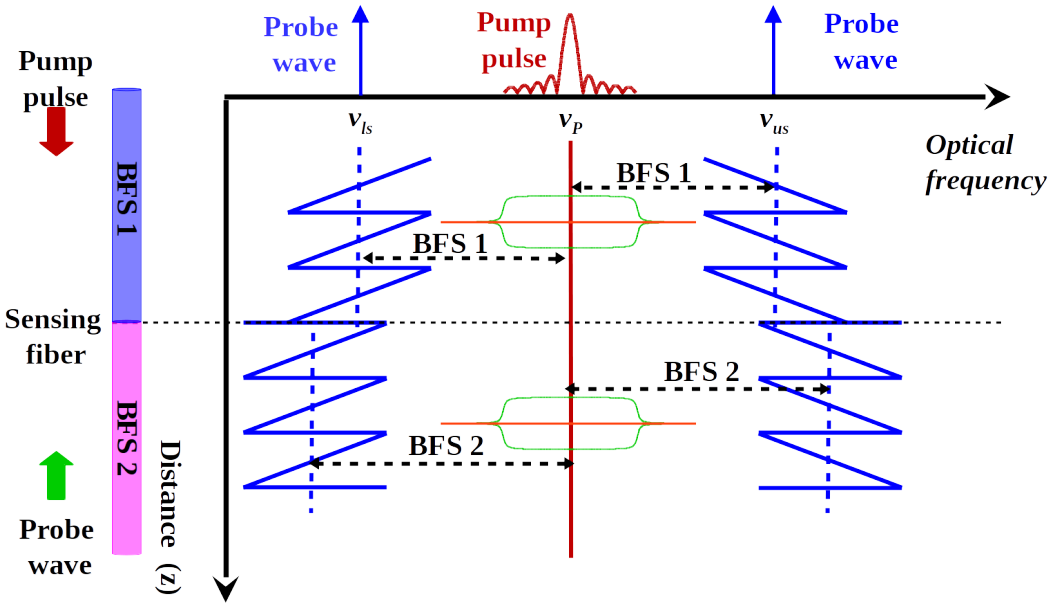

Figure 2.9: Fundamentals of the technique that tracks the BFS. Central frequency of the FM fits the local BFS of the fiber.

Notice that the BFS tracking just described does not need to be very precise or very fast. It is necessary just to adapt to changes in the average BFS profile of different sections of the fiber. This profile can be extracted from the measurements that the BOTDA system is continuously performing or even from a previous characterization of the BFS along the fiber using low spatial resolution, as it will be shown in the following sections. The system can work with sharp changes in BFS profile due to the use of different fiber types concatenated as well as with slow variations of the average BFS of the fiber link due to enviromental or cabling effects. Minor deviations of

the local BFS in small lengths of fiber are not significant because their contribution to the total integrated gain and loss affecting the pulse is going to be small.

2.4. Experimental setup

After the explanation of the basics of this technique, the system has been tested in the laboratory. With this purpose, the setup described in Fig. 2.10 was assembled [3]

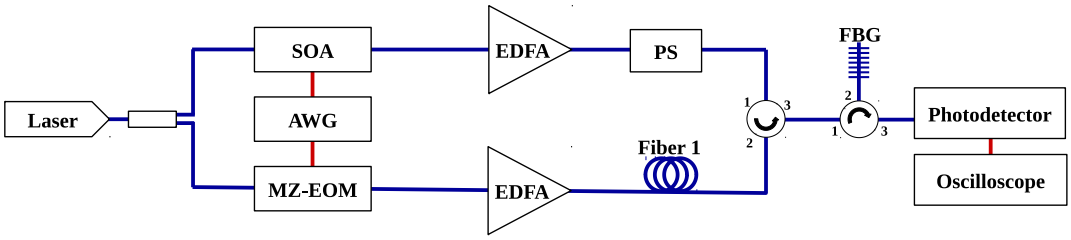

Figure 2.10: Experimental setup for the BOTDA sensor based on tracking the BFS with FM of the probe wave.

The output of a distributed feedback laser (DFB) laser is divided by a coupler into two branches to generate the pump and probe waves. In the upper branch, the output of the coupler is pulsed by a SOA driven by an electrical pulse from an arbitrary waveform generator (AWG). The pump pulse is boosted to a peak of 19 dBm using an EDFA, and its SOP is randomized using a polarization scrambler (PS).

In the lower branch, a dual-probe wave is generated using a Mach Zehnder-electrooptic modulator (MZ-EOM) that is biased at the minimum transmission point of its transfer curve to generate a double sideband suppressed-carrier signal. The MZ-EOM is driven by an AWG, which provides a microwave signal with a saw-tooth frequency modulation centered at 10.8 GHz and with a peak-to-peak frequency deviation of 300 MHz. Also, the AWG provides a synchronization between the electrical pulse and the FM modulation of the microwave signals in order for the pump pulses to always interacts with the same instantaneous frequency at the same location of the fiber [3]. The power of the probe waves is amplified in another EDFA before being injected into the sensing fiber in a counter-propagate direction to the pump pulse. Finally, after Brillouin interaction of these waves with the pump pulse, the probe waves are directed to a fiber Bragg grating via a circulator in order to filter out the upper-frequency probe, and the remaining lower-frequency probe is detected by a photo-detector, which is connected to an oscilloscope.

2.5. Experimental results

A 120-km length of standard single-mode fiber (ITU G.652) with different BFS sections was deployed in the setup of Fig. 2.10 in order to analyze the detrimental effect that a non-uniform BFS profile of the sensing fiber has on the compensation of second-order NLE, and also to demonstrate the capabilities of the proposed tracking technique to overcome this impairments. Fig. 2.11 shows the measured BFS profile of the fiber, where three different fiber spools with a slightly different BFS are clearly distinguishable. The BFS difference between the first two reels (50-km length each) was around 17 MHz, while the deviation between the second and third one (this one with 20-km length) was 46 MHz. This measurements were performed using the setup in Fig. 2.10

without adding the BFS tracking capability. The probe power was 12 dBm and long duration pulses of 200 ns were used because we were interesting just in the evolution of the average BFS along the fiber. During measurements, the last 20 km of the fiber was kept at constant controlled temperature in a climatic chamber.

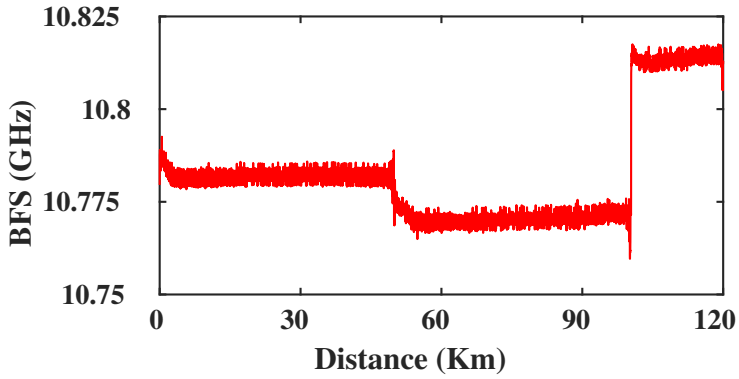

Figure 2.11: Measured BFS along the fiber with the low precision technique.

We started by characterizing the optical frequency response experienced by the pump wave as a result of its interaction with the probe waves. In order to perform this measurement we devised the experimental setup in Fig. 2.12, which is a modification of that in Fig. 2.10. The idea was to deploy the technique for optical transfer function measurement based on the use of optical single-sideband (OSSB) modulation [84]. We modified the upper branch of the setup in Fig. 2.10 to generate a OSSB signal whose sideband could be tuned in the range of frequencies of the pump pulse. Then, this OSSB signal counter-propagates with the probe waves so as to make the sideband experience the same transfer function that the pump pulse would experience. Finally, the OSSB signal is extracted at the far end of the fiber using a circulator and detected in a microwave bandwidth photodetector, which translates the optical transfer function from the optical to the electrical domain [84]. In addition, a 20-GHz electrical VNA is used to scan the frequency of the OSSB sideband and measure the optical transfer function.

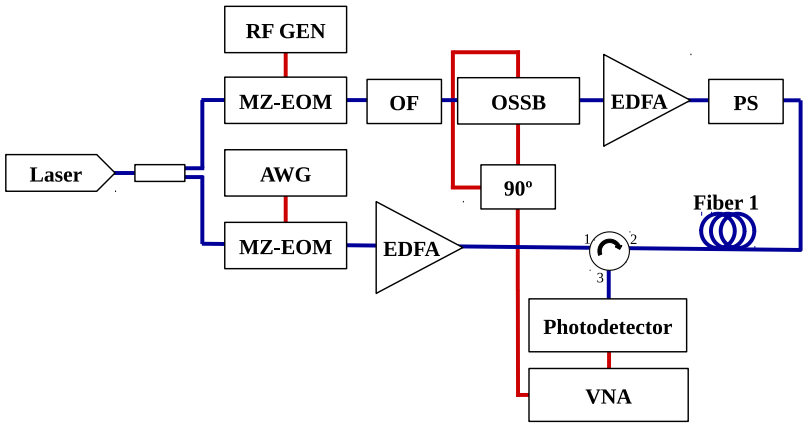

Figure 2.12: Experimental setup used in order to characterize the optical frequency response of the Brillouin interaction that the pump wave spectrum experiences.

The method to derive the OSSB from the laser in Fig. 2.12 uses first a MZ-EOM biased at minimum transmission and driven by an RF generator at 10 GHz to generate a double-sideband

suppressed-carrier signal. The lower-frequency sideband is later removed using and OF, which leaves a single spectral component that becomes the optical carrier of the OSSB and is spaced 10-GHz from the pump central frequency. Then this optical carrier is fed to an optical single-sideband electro optical modulator (OSSB-EOM), which is based on a MZ-EOM with two radio frequency (RF) electrodes driven using a 90° hybrid coupler [85]. The OSSB-EOM is driven by the VNA that scans the sideband frequency, by generating a microwave frequency sweep between 9.5 GHz and 10.5 GHz, and measures the optical transfer function experienced by the pump along the fiber and up to the microwave photodetector.

Fig. 2.13 depicts the distortion of the frequency transfer function, measured using the OSSB method, for increasing probe power. This is the transfer function that the pump pulse experiences due to its interaction with the probe waves. It can be clearly observed that as the probe power is raised, the distortion of the pump wave increases. Indeed, for probe wave powers of 0 dBm and 5 dBm the pump wave spectral distortion is negligible. However, when the probe power is increased to 15 dBm, the pump wave spectrum experiences a large distortion: the low and high frequencies of the spectrum experience a 4-dB peak loss and gain, respectively. Besides, this last measurement is compared in the figure with the calculations using the model in Eq. 2.12, showing good agreement in shape, despite some small differences attributable to the SpBS generated over the OSSB signal frequencies by the counterpropagating continuous probe waves. Notice that the frequency separation of the gain and loss peaks in Fig. 2.13 equals the peak-to-peak frequency deviation of the FM modulation introduced to the probe wave. In addition, the frequencies of the two lobes that each peak can be directly related to the difference between the central frequency of the FM modulated probe waves and the BFS of the different sections of the fiber.

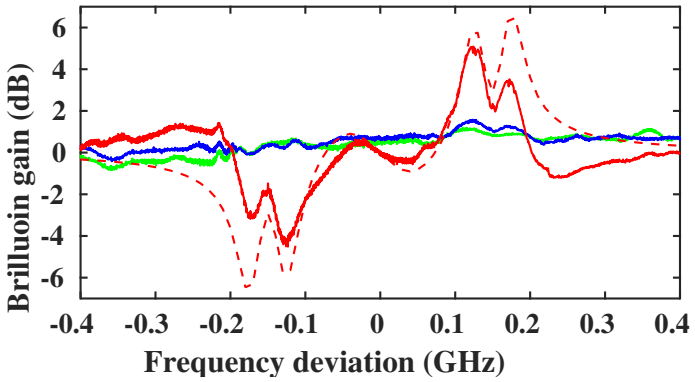

Figure 2.13: Mesured transfer function due to Brillouin interaction between pump wave and probe wave when power of probe wave is 0 dBm (green), 5 dBm (blue) and 15 dBm (red blue line). A simulation of model using Eq. 2.12, denoted by dashed red line, is shown using a probe wave of 15 dBm.

The distortion of the optical transfer function experienced by the pump pulse upon interaction with the probe waves translates to a distortion of the temporal shape of the pulses. This is highlighted in Fig. 2.14, that displays the temporal shape of a 20 ns pulse, measured at the output of the fiber in the setup of Fig. 2.10, when different probe wave power level are deployed. It can be observed that for probe wave power lower than 12 dBm the pulse shape does not experience nearly any distortion.

However, for 12 dBm probe wave power a ripple of around 11% of the pulse amplitude appears on the top of the pulse. Moreover, for 15 dBm this ripple is increased to a variation of 53% of the

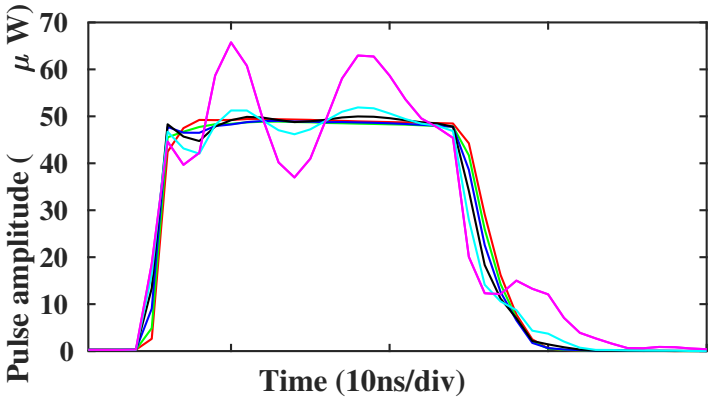

Figure 2.14: Optical pulses at the output of the fiber

amplitude of the pulse and, in addition, the fall edge of the pulse loses its original shape.

Once the detrimental effect on the pump pulse wave that the BFS difference along the sensing fiber had been studied, we experimentally demonstrate the performance of the new BFS tracking technique. For that purpose, the first step is to measure the average BFS profile of the sensing fiber, which was done and displayed in Fig. 2.11. Then the measured BFS profile is used to compensate the average BFS variation of the fiber, by adding an offset frequency to the probe wave modulation, as it was schematically explained in Fig. 2.10. Finally, we performed distributed measurements of BFS using 30-ns pump pulses (3-m spatial resolution) and a probe power of 15 dBm. This probe power was limited by the Brillouin threshold of the fiber. Fig. 2.15 shows the measured BFS measurement along the fiber when this BFS tracking is applied. Notice that is a "virtual" BFS since to obtain the real BFS it is necessary to subtract the frequency offset added to the probe wave modulation at each fiber section. The BFS is not completely flat in Fig. 2.15 because just the last 20 km of the sensing fiber were held inside a climate chamber during measurements. Hence, the first 100 km were exposed to laboratory temperature variations between the initial measurement of the average BFS in Fig. 2.11 and the measurements with tracking in Fig. 2.15, which explains that their BFS is slightly offset from 10.8 GHz. Note that in a real system the BFS tracking would be continuously in operation using previous measurement results so the BFS variation would be perfectly compensated.

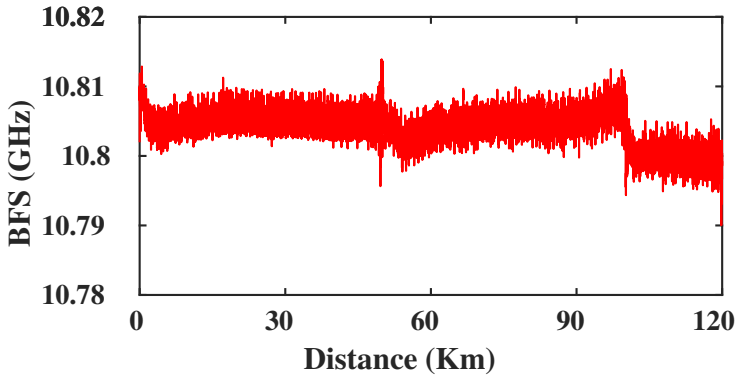

Figure 2.15: Virtual BFS measured using the sistem with tracking BFS.

Fig. 2.16 depicts the temporal shape of 20 ns pump pulses after crossing the whole fiber and for different probe wave power levels, when BFS tracking is applied. It can be observed, that for

a lower probe power than 15 dBm there is negligible pulse distortion, while for a probe power of 15 dBm just a small ripple appears and the fall edge of the pulse preserves is original shape. This small distortion, which does not impair measurements, is due to the residual variation of BFS that was observable in Fig. 2.17. Nevertheless it would be completely suppressed in a system with continuous BFS tracking.

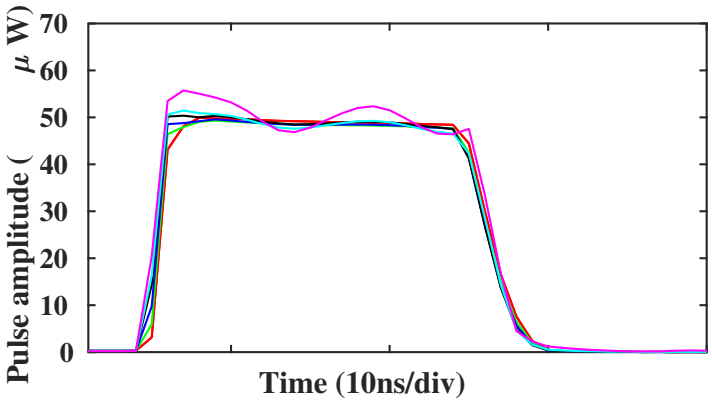

Figure 2.16: Pulses at the output of the fiber when the BFS tracking is applied.

Finally, in order to evaluate the precision of the system, a series of 18 consecutive measurements were performed. Fig. 2.17 shows the precision along the sensing fiber calculated from the standard deviation of those measurements at each location. An approx. 2-MHz (1σ) precision is obtained at the end of the fiber. All these measurements have been done with 1024 averages of the traces.

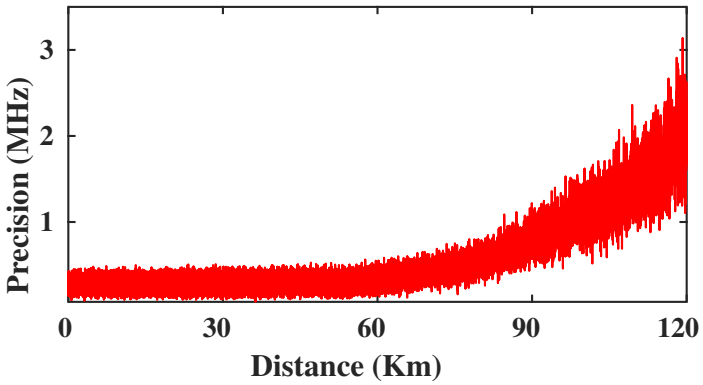

Figure 2.17: Precision of the measurement

2.6. Conclusions

In this chapter, we have introduced the way to obtain the ultimate performance of BOTDA sensors in terms of the probe power that they can deploy. We have identified the factor that was limiting the performance of currently available NLE compensation methods: the inability of those methods to cope with variations of the BFS profiles along the fiber. This is a limitation that really limits real world applications of long-range BOTDA sensors. We have demonstrated that indeed

this was the limiting factor by developing a theoretical model for the pump pulse distortion due to the interaction with the probe waves. Furthermore, we have verified this model experimentally.

In addition, we have presented a new technique that makes BOTDA sensors to completely compensate NLE by adding an optical frequency modulation to the probe to track the variations in average BFS found along the fiber. Therefore, the new limit to probe wave power is the effective Brillouin threshold of the sensing fiber. Nevertheless, the probe FM modulation technique that we deploy pushes this limit to higher powers than in standard BOTDA setups. Using our BOTDA setup, we deployed a probe wave of 15 dBm, which, to the best of our knowledge is the largest probe power ever injected in a long-range BOTDA setup. The enhancement in the detected SNR brought by the use of such power leads to an excellent sensor performance without resorting to additional means such as the use of pump pulse coding or Raman gain.

CHAPTER 3

Pump wave amplification in long-range BOTDA

3.1. Introduction

DURING the last few years, BOTDA has been one the centers of attention of DOFS due to its capability to monitor temperature and strain over extra-large structures. There are several scenarios with a great need for measurement distance of more than 50 km, such as structural health of gas and oil pipelines, bridges, or high voltage electric lines. Further that a long sensing distance, these applications have a common demand for high spatial resolution in the order of one meter or even shorter. Currently, these requirements make it necessary to install several interrogators covering each one a short distance, increasing the cost of the whole system dramatically.

As explained in the section 1.2.5.3 in the introduction chapter, in BOTDA systems a CW probe wave counter-propagates a pump pulse. When frequency detuning between these both waves is almost the same as the BFS of the fiber, there is a Brillouin interaction between them. Probe wave suffers a gain (or loss, depending on the configuration of the sensor) in its amplitude that can be described as:

$$\Delta P_S(z) = \frac{g_0}{A_{eff}} P_{P_i} e^{-\alpha z} P_{S_i} e^{-\alpha L} u \tag{3.1}$$

where the probe wave and the pump wave are given by P_{S_i} and P_{P_i}. g_0 denotes the local coefficient of gain due to Brillouin interaction, A_{eff} is the effective area of the fiber, α means the optical attenuation coefficient of the fiber, L the length of the fiber and u the spatial resolution, given by the temporal width of the pulse as 10 ns$\sim$ 1 m.

As can be observed in Eq. 3.1, the gain that the probe wave experiences is twice dependent on the coefficient of attenuation. One of the dependences defines how the probe wave is attenuated due to its propagation through fiber (αL). On the other hand, the coefficient of attenuation modulates the gain of the Brillouin gain of the probe wave as the pump wave propagates through the fiber (αz). Because of these two contributions of the coefficient of attenuation, the SNR of the detected Brillouin gain drops to small values.

3.2. Techniques used to compensate optical attenuation

The main limitation brought by the optical attenuation of the optical waves is a degradation of the SNR. Assuming that the input powers of all signals injected in the fiber are maximized and optimized in order to avoid non-linear effects such as MI, SpBS, or NLE, the simplest technique to boost the SNR is to perform a signal averaging. But although this technique does not require to implement a modification in the optical setup, it becomes impracticable when the number of averages, N, is largely increased. While the SNR is improved as a factor $\sqrt{N}$, the measurement time is increased with the number of averages, N.

Some techniques that avoid a measurement time penalty implement an amplification of the optical signals. One of the solutions consists of the installations of EDFA repeaters along the fiber link [35, 86]. In these setups, a pair of EDFAs are inserted in the middle of the fiber. Two circulators extract the signal from the fiber, and each circulator sends the probe and pump pulse to the correct EDFA. After both signals have been boosted, they are injected in the sensing fiber link again. Although this kind of technique permits to extend a sensing distance up to 150 km, the EDFAs need to be powered, limiting their use in remote areas.

Several solutions that do not need to be powered away from the interrogation unit have been proposed. All the systems have a point in common with the use of distributed amplification schemes. The first of them is the use of distributed Raman amplification (DRA). This system injects a Raman pump into the fiber, generating a Raman interaction that leads to the an amplification of the pump pulse and also probes wave if a bidirectional DRA pump configuration is used [31, 87]. With these setups, a sensing range of 100 km with a spatial resolution of 0.5 meters has been reached. Nevertheless, Raman interaction has a huge bandwidth, so tens of nanometres bandwidth are wasted. Besides, since DRA needs to pump a high optical power into the fiber, it presents an eye-safety concern when the system is operated in real scenarios. Finally, relative intensity noise (RIN) from the Raman pump is translated to the amplified signal, leading to the degradation of SNR of the signal.

Finally, a technique that does not introduce noise in the system, and amplifies the pump wave using distributed Brillouin amplifier (DBA), was presented as a solution to the problem of the optical attenuation [34]. This system is based on a conventional dual-band probe wave BOTDA, where an extra optical signal has been added. This other signal is provided by a laser whose wavelength has been directly modulated by an electrical current following a triangular shape. As a consequence, an extra interaction occurs over the pump wave. This Brillouin interaction is distributed along the whole pump spectrum, generating a flat gain spectrum that does not disturb the pump wave shape. The performance of this system was successfully demonstrated with the compensation of the optical attenuation that pump pulse suffers in a 50-km length sensing fiber. Further of this work, a sensor that amplifies the pulsed pump wave and does not need to install an extra laser in the setup has been developed during this thesis. This technique generates a gain over the pump wave by its interaction with the probe wave.

3.3. Fundamentals of the gain generation by the probe wave over the pump wave

The technique introduced in this chapter compensates for the attenuation of the pump wave by means of the intrinsic gain generated by the Brillouin interaction. The basics of this technique is the system developed in chapter 2 but, in this case, the lower optical frequency probe wave is

filtered out so that the pump wave spectrum experiences a net gain.

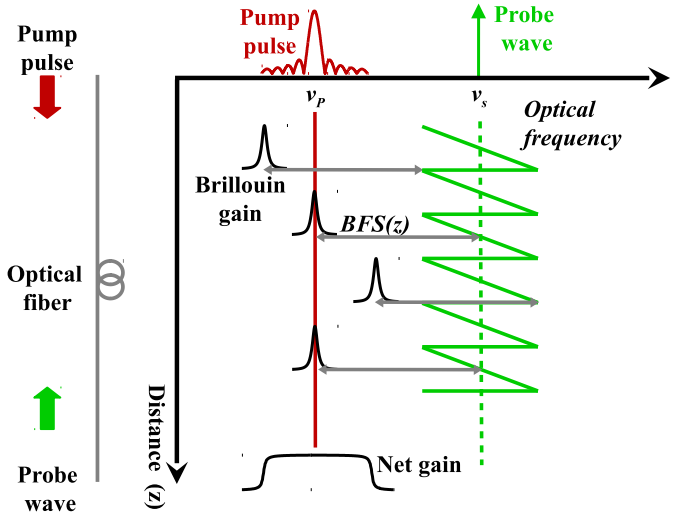

Figure 3.1: Optical waves present in the optical fiber.

Fig. 3.1 depicts, schematically, the fundamentals of the technique. As in a conventional BOTDA, two optical waves that counterpropagate are used, pump pulse and probe wave. In this case, the sensor is arranged as a loss-based configuration. Therefore, the pump wave generates a loss of the probe waves at the same time that the probe wave transfers energy to the pulse wave at every location of the optical sensing fiber. As a difference to a conventional BOTDA, in this case, the probe wave is frequency modulated following a sawtooth shape, so at each position of the fiber the interaction between the pump wave and probe wave occurs with a different frequency separation. The Brillouin gain spectrum that the pulse wave experiences at each location has a Lorentzian shape, but in this case, this Brillouin spectrum gain is slightly shifted in frequency at each position of the fiber. As a consequence, after the Brillouin interaction along all the fiber, the net gain over the frequency spectrum of the pulse wave has a flat shape.

Unlike the conventional BOTDA scan, where the frequency is performed using a discrete frequency swept, this system takes advantage of the frequency modulation of the probe wave. The local instantaneous frequency of the Brillouin interaction depends on the time delay of the optical frequency modulation of the probe wave relative to the launch of the pump pulses in the fiber. Then, variating this relative time delay, the frequency of the Brillouin interaction changes at each location of the fiber. Each relative time delay step applied to both signals will be equal to the sawtooth period of the modulation divided by the number of steps that are applied to the scan process.

3.3.1. Theoretical study of this technique

In order to explain the Brillouin interaction between both waves shown in Fig. 3.1, the well-known steady-state coupled wave equations for the intensity and pump wave are used [88]:

$$\frac{dP_p(z)}{dz} = -g_b(\Delta\nu)P_p(z)P_s(z) - \alpha P_p(z) \tag{3.2a}$$

$$\frac{dP_s(z)}{dz} = -g_B(\Delta\nu)P_p(z)P_s(z) + \alpha P_s(z) \tag{3.2b}$$

Note that these coupled wave equations are only valid when the Brillouin interaction is longer than the phonon lifetime (10 ns), so in order to use this approximation, it is assumed that the deployed pulses are longer than the acoustic phonon lifetime . From the solution of the coupled equations (Eq. 3.2), the evolution of the pump wave is found as:

$$P_p(z) = P_p(0)exp\left[\int_0^z \frac{\eta(z)g_B(\Delta\nu)}{A_{eff}} P_S(L)exp(-\alpha(L-z))dz\right] exp(-\alpha z) \tag{3.3}$$

where the power of the pump and the probe wave injected in the fiber are represented by $P_p(0)$ and $P_s(L)$, L is the length of the fiber while A_{eff} is the effective area, g_B is the Brillouin gain coefficient that depends on $\Delta\nu$, which is the local detuning frequency from the center of the Lorentzian Brillouin spectrum and is given by:

$$\Delta\nu(z) = \nu_p - \nu_s(z) + BFS(z) \tag{3.4}$$

being ν_p the optical *frequency* of the pump wave, $\nu_S(z)$ is the frequency of the probe when meets the pulse at a position z of the fiber and $BFS(z)$ is the BFS at a position z of the fiber. Notice that $\Delta\nu(z)$ variates along the fiber length since a frequency modulation over to the probe wave, as a consequence, the effect that the probe wave has has been applied to the pump pulse spectrum is defined by the integration, along the optical fiber, of multiples periods of the shape of the frequency modulation. The net gain that the pump pulse spectrum experiences depends on the shape of the FM.

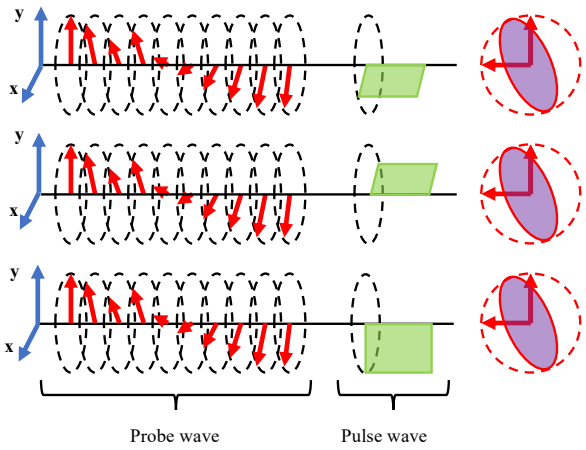

Figure 3.2: Interaction when pulsed signal is polarization randomized

It is essential to highlight the importance of the effect of the relative SOP between pump wave and probe wave, denoted in Eq. 3.3 by $\eta(z)$. As in a conventional BOTDA setup, the relative SOP between both counterpropagating waves determines the efficiency of the interaction. In low-birefringence single-mode optical fibers, the logarithmic gain varies between a minimum of 1/3 when both waves are orthogonal and maximum of 2/3 for parallel counter-propagating signals [80]. Fig. 3.2 schematically displays the situation of the interaction between both waves, probe and pulse pump signals, when a PS randomizes the pump wave. It is shown how the SOP of the probe wave varies slowly along the optical fiber due to the low. Then, the SOP of each pulse injected in

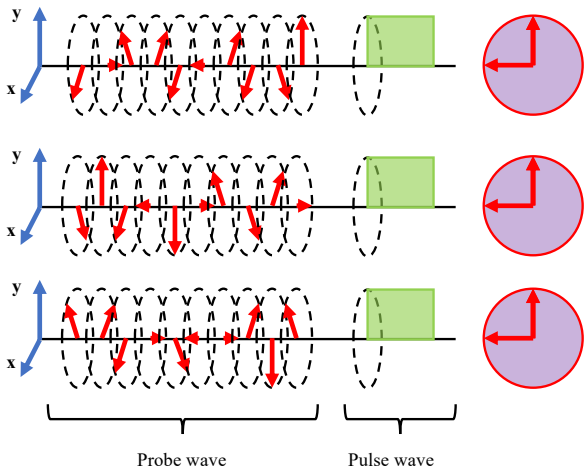

Figure 3.3: Interaction when probe wave signal is polarization randomized

the fiber changes randomly. In this case, each pulse meets the same SOP of the probe wave in each location of the fiber. Consequently, the gain that pump pulse experiences depends on the polarization and can be represented by an ellipse with a 1/3 and 2/3 relationship between its mayor and minor axes (in purple color). This means that one polarization of the pulse may experience a large gain; meanwhile, its orthogonal experiences a smaller gain. The orientation of this elliptic gain depends on the initial SOP of the probe wave. As a consequence, each pulse experiences different gain in each polarization axis, an effect that is not compensated by the averaging process. Since the gain depends on the initial SOP of the probe wave, the solution consists of randomizing instead the SOP in this case of the injected probe wave. Fig. 3.3 displays the relative SOP between probe waves (red arrows) and pump pulse (green rectangles). In this case, the SOP of the probe wave varies randomly along its travel through. In this way, each pulse experiences interaction with a probe wave, whose relative SOP varies randomly along all the possible polarizations during its way. As a consequence, pulses experience a gain that is equally distributed along the possibles SOP leading a polarization non-depending gain, as the purple color circles in the figure indicate.

3.4. Experimental setup

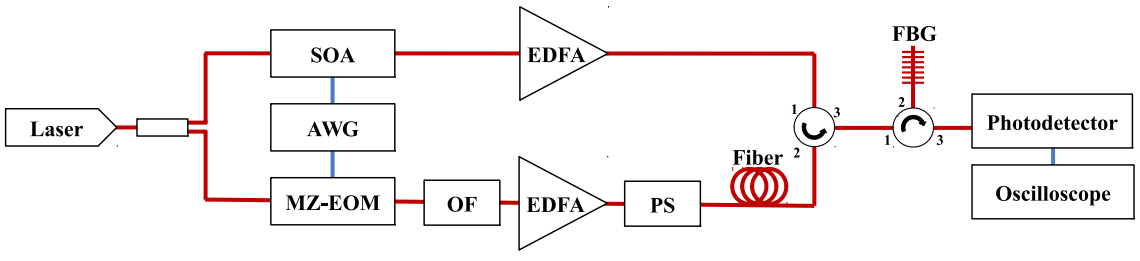

Figure 3.4: Experimental setup for the BOTDA sensor based on frequency modulation of the probe wave.

The setup used in this technique is shown, schematically, in Fig. 3.4. In this setup, the microwave generator used in a regular BOTDA setup is substituted by an AWG. The purpose of the

AWG is to feed the MZ-EOM with a microwave signal used to generate the FM probe wave. A DC signal is used to set the bias voltage of the MZ-EOM in order to generate a double-sideband suppressed-carrier signal. The signal that the AWG supplies is a FM microwave with an instantaneous frequency that varies around the average BFS of the fiber. In this case, the FM microwave follows a saw-tooth shape with a frequency deviation, peak-to-peak, of 200 MHZ and a period of modulation of 12.5 milliseconds (frequency rate of 80 kHz). A lower-cost alternative to the use of the AWG would be to deploy a microwave voltage control oscillator driven by a saw-tooth signal. In order that the pulse always meets the same instantaneous frequency of the probe wave at a given location during an scan step, the frequency modulating signal and the electrical pulse signal that is applied to the driver of the SOA have to be perfectly synchronized, therefore this electrical pulse is generated on the same AWG than the FM signal. Through the change of the relative time delay between the FM and pulse signals, the instantaneous frequency that the pulse meets in each point of the fiber can be changed. After the MZ-EOM, an OF filters out the lower-frequency sideband of the probe wave. Then, the upper-frequency sideband of the probe wave is amplified, using an EDFA up to the limit of 9 dBm, imposed by NLE. Next to that, a PS randomizes its SOP. Finally, the probe wave is launched into 100-km of G.652 FUT. The disposition of the fiber is in two spools of 50 km each one and a hotspot of 140 m located at the extreme end of one of them.

In the upper branch, the pulsed signal, generated by the SOA, is amplified using an EDFA to a peak power of 19 dBm, which is the maximum power before non-linear effects appear. After that, a circulator drives the pulsed signal direct to the FUT.

After the Brillouin interaction inside the fiber the same circulator sends the probe wave to another circulator where an fiber Bragg grating (FBG), configured in reflection, selects the probe wave. Finally, the signal is detected by a photodetector and digitized and store in an oscilloscope.

3.5. Experimental results

Once the theoretical and experimental fundamentals and of this technique has been established, several experiments, to demonstrate experimentally the validity of this system, have been carried out.

Figure 3.5 compares the distribution of the Brillouin spectra measured along the fiber with a dual-probe-sideband BOTDA [3] and for the new BOTDA with amplification of the pump pulse. For the dual-probe BOTDA, the amplitude of the Brillouin spectra decays exponentially due to the attenuation of the pump pulse as it propagates through the fiber. In contrast, in our system, the amplitude initially decays but starts to recover at a distance of around 30 km from the pump input, as it can be seen more clearly in the BOTDA trace in Fig. 3.6. At that distance the gain provided by the probe wave to the pump pulse starts to be significant. Considering that the gain experienced by the pump pulse does not increase the noise level in the measured response of the sensor [34], the increment of the detected amplitude along the fiber translates into an enhancement of the SNR. Notice that this is a BOTDA in loss configuration, but the amplitude of the traces have been inverted for clarity.

Figure 3.7 highlights the effects of polarization on the measured BOTDA signal. It is well-known that the relative polarization state of the pump and probe waves at each location of the fiber determines the mixing efficiency of the gain (or loss) experienced by the probe. This is given by the $\eta(z)$ factor discussed in section 3.3.1 that goes from $\eta(z) = 0$, for orthogonal polarization, to $\eta(z) = 1$, for identical polarization. Therefore, the common practice is to scramble the polarization of one

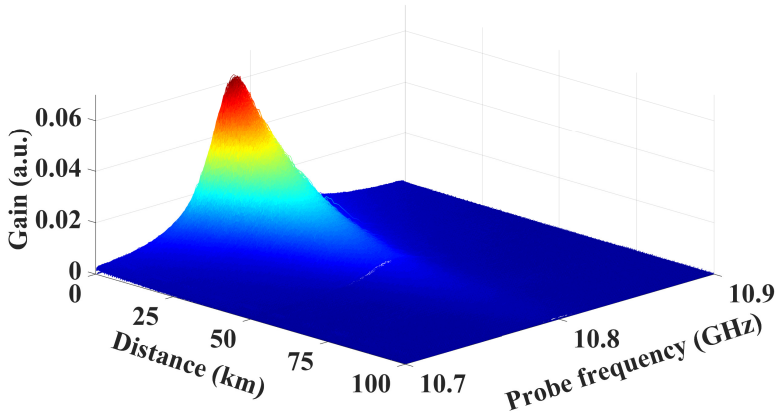

(a)

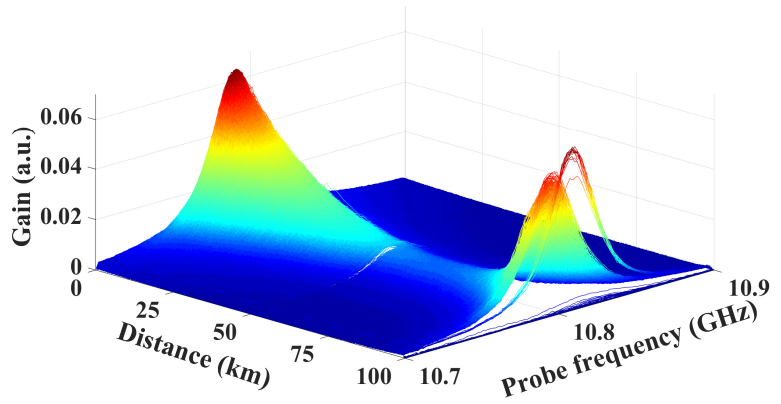

(b)

Figure 3.5: Brillouin gain distribution measured with (a) dual-probe-sideband BOTDA sensor using frequency modulation of the probe wave and (b) novel BOTDA with pulse amplification. A pulse duration of 45 ns was deployed in both measurements.

of the two waves while performing the average of a number of acquisitions of the measurement, so that an average $\eta(z) = 1/2$ response is obtained. However, in our setup, the interplay of the polarization of pump and probe waves is more complex than in conventional BOTDA because the change of the relative polarization state of the two waves also influences the gain experienced by the pulse (Eq. 3.3) as it travels along the fiber. This gain, as it was discussed above (section 3.3.1), ranges from 2/3 to 1/3 of the maximum ideal value obtained for a fiber with no birefringence and identical SOP of pump and probe wave [80].

The two traces shown in Fig. 3.7 compare the measured BOTDA signal with the PS either in the upper branch of the setup after the EDFA, or in the lower branch. Notice that the polarization-induced noise with the PS in the upper branch is larger than when it is in the lower branch, particularly, at the final part of the fiber where the pulse is amplified. The reason for this is that when the scrambler is in the pump branch, the successive pump pulses arrive to a particular position, z, of the fiber with different polarization for each measurement realization. However, contrary to conventional BOTDA, the gain experience by successive pulses is going to also change for each input SOP generated by the PS. Therefore, the Brillouin interaction (loss in this setup) experienced by the probe at that particular, z, does not average in general to a $\eta(z) = 1/2$ factor as

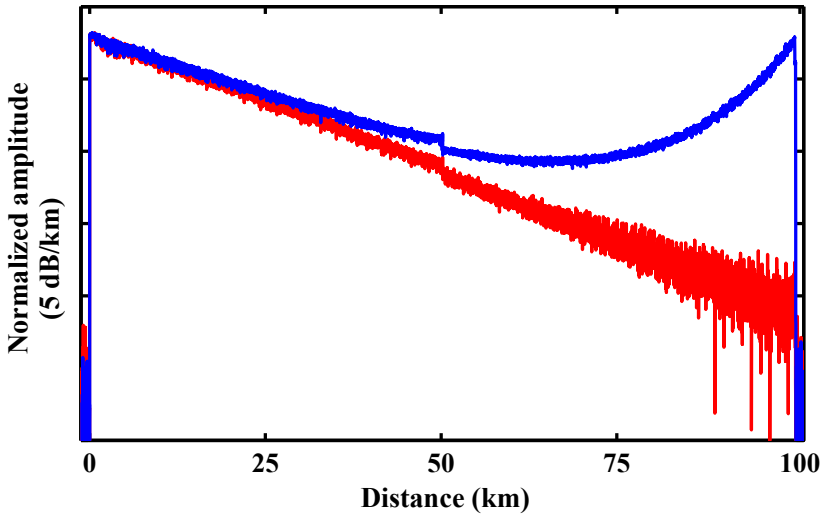

Figure 3.6: Mesured traces of dual-probe-sideband BOTDA (red line) and BOTDA with pulse gain (blue line) using 45-ns pulse duration.

in a conventional BOTDA. The average $\eta(z)$ depends on the particular SOP of the probe at that location and its relative orientation to the SOP of the pump pulse with maximum and minimum gain. In fact, it was observed that the averaged interaction at each particular location of the fiber changed over time due to the slow drift of the relative SOP of probe and pump pulse. This latter effect can severely degrade measurements due to amplitude drifts when the full Brillouin spectra is scanned. The problem with polarization just described can be solved by placing the PS in the probe branch because, in this case, during the course of averaged measurements, the successive pump pulses arrive at each particular location with an average gain after counter-propagating with the probe wave of aleatorized polarization. Then, as the measurement in Fig. 3.7 highlights, a stable averaged Brillouin interaction is experienced by the probe wave at each location.

After the dependence of the Brillouin gain on the relative SOP has been addressed, the amplification that pulse suffers after their propagation through the fiber is shown.

Figure 3.8 presents the detail of the amplification of the pump pulses in extremes of the fiber. The pulses at the input of the fiber and at the output with and without gain are compared for pulses with 45-ns and 55-ns durations. The pulses are amplified by 19.6 dB, compensating the fiber link attenuation. The amplification that pulses suffer is around 19.6 dB, compensating the fiber link attenuation. Notice that the amplified pulse has its leading edge smoothed, generating an increment in its time of rise. Nevertheless, the falling edge keeps its original fall time previous to amplification. This behaviour is due to the fact that stimulated Brillouin scattering is a dynamic phenomena that depends on the interaction of a pump and Stokes waves via acoustic wave. The probe wave, which plays a role of pump in this interaction, is present at a certain location in the fiber and then, when the pump pulse (which acts as Stokes wave) arrives, an acoustic wave is created and the gain starts to gradually grow until it reached and steady state (if the pulse is long enough). Finally, when the pulse leaves the gain is abruptly cut-off.

This effect leads to a distortion of the pulse shape and that can induce a BFS error by SPM, as we previously observed [88]. SPM changes the instantaneous optical frequency of a pulse by [34]:

$$\Delta f(t) = -\frac{\gamma L_{eff}}{2\pi}\frac{dP(t)}{dt} \tag{3.5}$$

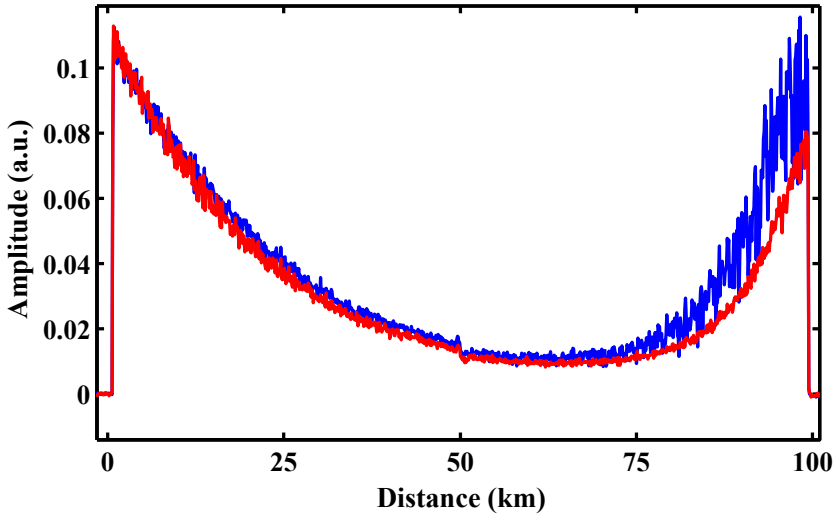

Figure 3.7: BOTDA trace depicting the comparison of the measured polarization noise when the polarization scrambler is either used on the probe wave (red line) or on the pump pulse (blue line)

where L_{eff} is the effective length and γ is the nonlinear coefficient of the fiber. $P(t)$ is the temporal shape of the pulsed wave. Previous studies have reported how this instantaneous frequency shift influences in BOTDA sensors when using pulses that are symmetrical in the time domain and have relatively slow transitions [89]. In that case, SPM induces a symmetrical broadening of the pulse spectrum because Δf in both sides of the pulse have equal amplitude and opposite sign. Then, the broadening of the pulse spectrum results to a broadening of the measured Brillouin spectrum linewidth. However, when an asymmetry in the time-domain shape of a pulse is introduced, like the rise-time smoothing induced by the Brillouin gain in this case, SPM induces an asymmetrical broadening of the pulse spectrum that leads to an error in the measured BFS [34].

Nevertheless, in our BOTDA with gain, the BFS measurement due to SPM can be avoided by deploying differential pulse pair (DPP) measurements [30], which subtract the response of two pulses with different durations, such as the ones depicted in Fig. 3.8. This eliminates the effect of the instantaneous optical frequency shift in the smoothed leading edge of the pulses. Moreover, the use of DPP also helps to solve another problem that is caused by the smoothing of the leading edge of the amplified pulse. This effect generates a change in the effective spatial resolution along the fiber as it can be observed in Fig. 3.8, in which the pulse at the output of the fiber becomes narrower compared to the pulse at the input of the fiber. However, DPP measurement provides a constant resolution independently of the gain of the pulse. This is due to the fact that DPP technique involves the subtraction of the response to the common part of both pulses and the measurement of just the response to the differential part between both pulses. In the set of pulses shown in Fig. 3.8 a constant spatial resolution of 1 meter (55 ns-45 ns = 10ns$\sim$ 1 m).

Figure 3.9 shows the measured BFS distribution in the fiber using DPP technique with two pulses of 45 and 55 ns. Two measurements were sequentially performed with the fiber inputs swapped so as to make sure that the BFS distribution is identical independently of which end is used to inject the probe and pump wave and hence that SPM or non-local effects are not introducing any significant errors. In order to avoid the influence of the temperature variations of the room, where the experiment was carried out, last 140 m of the fiber link in which a different type of SMF with a slightly different BFS was kept at constant temperature using a climate chamber. The

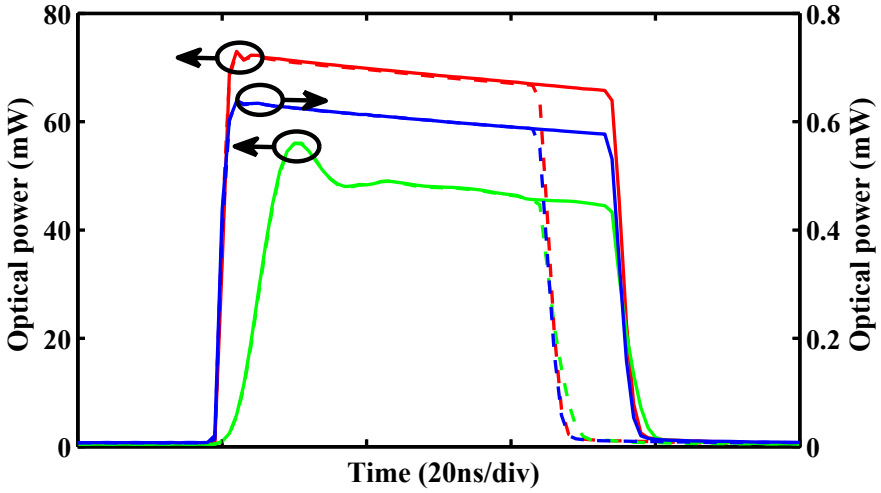

Figure 3.8: Amplification of pump pulses with 45-ns (dashed line) and 55-ns (solid line) duration. Pulses are shown at the input of the fiber (red line), output of the fiber without gain (blue line) and amplified pulses (green line).

detail of the BFS measured at this fiber section is shown in the inset of Fig. 3.9, where an almost identical BFS for both measurements can be observed. It van be also seen that the BFS in the rest of the fiber outside the climate chamber in the room. Notice that, in the temperature controlled fiber length, there is a residual BFS difference of around 0.5 MHz for the measurement in both directions. This small difference is attributed to the effect of the EDFA amplification on the pulse shape. As Fig. 3.8, the top of the pulses are not completely flat, but have a small slope due to the transient effects in the EDFA. This slope, according to Eq. 3.5, leads to a small positive shift in the instantaneous frequency of the pulse that introduces the observed small error in the BFS. In fact, we made estimative calculations using a typical parameter of nonlinear coefficient for SMF that agree well with the observed frequency shift in BFS. These small residual error in the BFS can be avoided simply by making sure that we use a flat-top pulse, which can be achieved, for instance, by using an EDFA prepared for pulsed or bust operation [90].

Finally, Fig. 3.10 displays the BFS measurement uncertainty along the fiber calculated as the standard deviation of 5 consecutive measurements. It shows that the maximum uncertainty is around 1 MHz. Furthermore, as it was expected, the measurement precision and the spectra amplitude in Fig. 3.5(b) are directly related. The section with a larger uncertainty coincides with the positions of the fiber with lower spectra amplitude. All these measures have been done applying an average of the traces of 1500 samples.

3.6. Conclusion

During this chapter, the limitation that optical attenuation presents in long-range BOTDA has been addressed. It allows to increase the measurement range of BOTDA sensors.

We have demonstrated a BOTDA sensor that provides gain to the pump pulses without apply major alterations to the conventional BOTDA setup. Consequently, this new sensor faces is able extend the measurement range up to 100 km with 1-m resolution and 1-MHz BFS precision. This is done without the need to add any amplification scheme, such as Raman amplification, but just

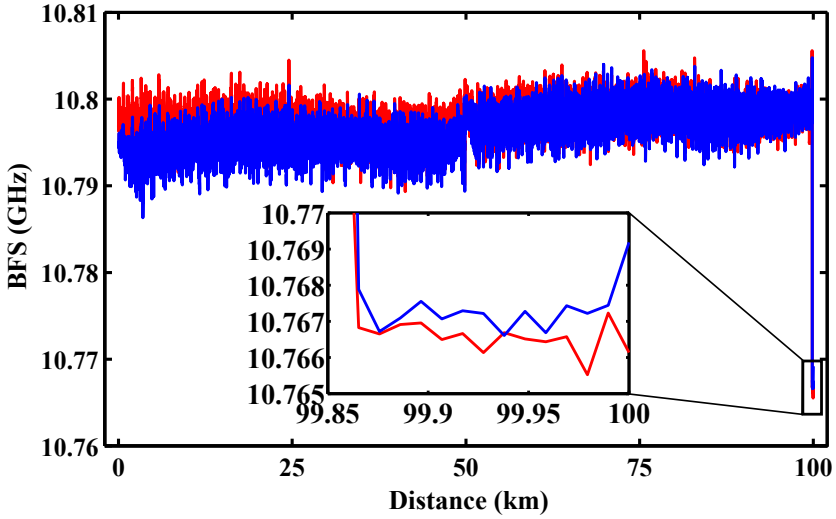

Figure 3.9: Measured BFS distribution along the fiber with the pump pulses injected by the fiber's end were the hotspot is located (red line) or by the opposite end (blue line) and detail of BFS measurement in the hotspot (inset)

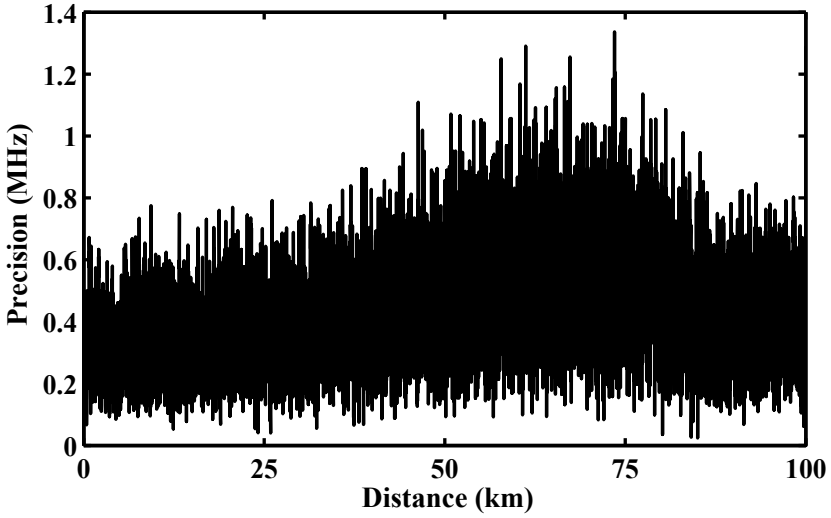

Figure 3.10: Precision of the BFS measurement obtained along the fiber.

taking advantage of the interaction of the two waves, pump pulse and probe, that are used in all BOTDA sensors.

CHAPTER 4

Sidelodes apodization in optical pulse compression DAS

4.1. Introduction

In basic $\phi-$OTDR, an ultra-coherent optical pulse is launched into a FUT. Different RS, randomstatically placed along the fiber, generate multiples copies of the pulse that interfere generating an amplitude and phase pattern in the backscattered signal. When an external perturbation, such as temperature variation or mechanical perturbation is applied to the optical fiber, the relative position between different RS are modified. As a consequence, the amplitude and phase patterns that arise from the interference are modified. These changes in the pattern are modulated by the perturbation, so that perturbation can be demodulated by sampling pairs of positions in RS traces and examining the variation of their relative phase [64].

Among the principal limitations that sensors based on OTDR face, is the attenuation of the pulse power due to optical losses of the fiber. This decreasing of the power of the pulse becomes detrimental to the SNR of the measurement, which depends directly on the energy of the pulse. The energy of the pulse has a dependence on both the amplitude and temporal width of the pulse. Both parameters that characterize the optical pulse can be modified in order to increase the energy of the pulse, hence, the SNR of the measurement. Amplification of the pulse amplitude is linked to the onset of non-linear effects such as SPM and MI. Therefore, these effects let to the degradation of the SNR. Another possibility to increase the energy contained in the pulse is to extend the time duration of the pulse. However, since the spatial resolution of the sensor depends on the temporal width of the pulse, longer pulse duration implies a degradation of the spatial resolution, which impairs the performance of the sensors when a high spatial resolution is needed.

Therefore, the energy of the pulse, and hence the SNR of the system, is limited by the trade-off between pulse length and spatial resolution. In order to overcome this limitation, the OFDR technique was presented. This technique performs a scan of the fiber launching a continuous linear frequency signal along a given bandwidth. Once the frequency scan has been performed, the inverse FFT of the OFDR measurement response is calculated, giving the reflectometry response of the fiber in the time-domain [91]. The spatial resolution given by the OFDR technique is linked directly to the bandwidth of the frequency sweep scan applied. Moreover, since the scan is performed using CW, the SNR of the measurement does not decay when the bandwidth (spatial resolution) is

increased. However, these kinds of systems need to perform a scan with different optical frequencies adds a temporal delay to the measurements, making them not suitable dynamical measurements. Moreover, the measurement range is limited by the coherence length of the laser source, although this limitation can be overcome at the cost of increasing the complexity of the system and using an expensive optical implementation [92].

In order to overcome these limitations, that both OTDR and OFDR present, a technique called OPCR is presented. This technique is based on the pulse compression used in radar [93, 94]. In sensing techniques based on reflectometry, such as radar, OTDR and OFDR, it is possible to launch into the FUT, a well-known signal that generates a backscattering pattern. This backscattering pattern is formed by a superposition of multiple copies of the launched signal. The fact that the signal used and, as a consequence, the reflected signal is well-known facilitates to make use of a matched filter that permits to maximize the SNR of the measurement.

In this chapter, a technique to reduce the sidelobes that are a side effect of using square-shaped pulses with linear frequency modulation (LFM) in pulse compression technique is developed. The technique goes further than the electrical limitations imposed by radar techniques, exploiting the capabilities of optical devices. Firstly, the basics of the pulse compression including its limitations are explained. Then, techniques previously used to avoid these limitations are exposed. Finally, the proposed solution to the sidelobes issue is fully described and experimentally demonstrated.

4.2. Basics of pulse compression

During the introduction of this chapter, the principal limitations of the ϕ-OTDR linked to pulse energy, such as trade-off between SNR and spatial resolution has been discussed as well as some solutions, previously proposed. Next, OPCR technique with its limitations, when square-shape is used, is introduced. In this section, the basics of pulse compression and the solutions proposed in this thesis to face its limitation will be presented.

As it is well-known, and can be found in the literature about radar technology, for a given input signal, $S(t)$, the temporal impulsive response of the matched filter that maximizes the SNR of the measurement is given by $X(t) = S^*(-t)$, being * the complex conjugation operation [93].

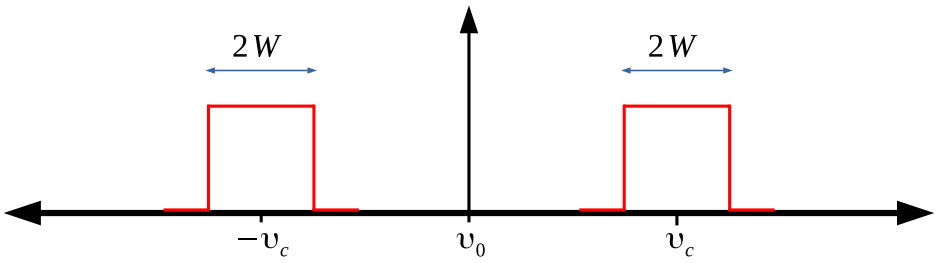

Figure 4.1: spectrum of a complex passband signal.

The output of the filter is given by the convolution between signal and temporal impulsive response of the filter.

$$S_0(t) = S(t) \circledast X(t) = S(t) \circledast S^*(-t) = \int_{-\infty}^{\infty} S(\tau)S^*(\tau - t)d\tau \tag{4.1}$$

Where $S(t)$ is a bandpass signal, schematically depicted in Fig.4.1. This signal in centred at $\pm\omega_c = \pm 2\pi\nu_c$ with a bandwidth equal to $2W$ and is given by:

$$S(t) = \frac{1}{2}u(t)e^{j\omega_c t} + \frac{1}{2}u^*(t)e^{-j\omega_c t} \tag{4.2}$$

Using the narrow bandpass signal described in Eq. 4.2, where $u(t)$ represents que complex envelope of the modulated signal, the output of the matched filter can be described as [93]:

$$S_0(t) = \frac{1}{4}\int_{-\infty}^{\infty}\left[u(\tau)e^{j\omega_c\tau} + u^*(\tau)e^{-j\omega_c\tau}\right]\left[u^*(\tau - t - t_0)e^{j\omega_c(\tau-t-t_0)} + u(\tau - t - t_0)e^{j\omega_c(\tau-t-t_0)}\right] \tag{4.3}$$

after the product inside the integral has been developed, Eq. 4.3 results in:

$$\begin{aligned} S_0(t) =& \frac{1}{4}e^{j\omega_c(t-t_0)}\int_{-\infty}^{\infty}u(\tau)u^*(\tau - t - t_0)d\tau + \\ & \frac{1}{4}e^{-j\omega_c(t-t_0)}\int_{-\infty}^{\infty}u^*(\tau)u(\tau - t - t_0)d\tau + \\ & \frac{1}{4}e^{j\omega_c(t-t_0)}\int_{-\infty}^{\infty}u^*(\tau)u^*(\tau - t - t_0)e^{-2j\omega_c\tau}d\tau + \\ & \frac{1}{4}e^{-j\omega_c(t-t_0)}\int_{-\infty}^{\infty}u(\tau)u(\tau - t - t_0)e^{2j\omega_c\tau}d\tau \end{aligned} \tag{4.4}$$

As it can be seen in the last equation, line 2 and 4 are the complex conjugate of lines 1 and 3 of Eq.4.4 respectively, so using $(a + jb)(a - jb) = 2\Re\{a + jb\}$, Eq. 4.4 it can be rewritten as:

$$\begin{aligned} S_0(t) =& \frac{1}{2}\mathbb{R}\left\{e^{j\omega_0(t-t_0)}\int_{-\infty}^{\infty}u(\tau)u^*(\tau - t + t_0)d\tau\right\} + \\ & \frac{1}{2}\mathbb{R}\left\{e^{j\omega_0(t-t_0)}\int_{-\infty}^{\infty}u^*(\tau)u^*(\tau - t + t_0)e^{-j2\omega_c\tau}d\tau\right\} \end{aligned} \tag{4.5}$$

the second term of the last equation corresponds to the FFT of $u^*(\tau)u^*(\tau - t + t_0)$ evaluated in $\omega = 2\omega_c$. Since the signal $S(t)$ is a narrowband signal centred in ω_c, the spectrum of the complex envelope, $u(\tau)$ decays below ω_c, therefore it is well justified that second term of Eq. 4.5 is neglected, becoming:

$$\begin{aligned} S_0(t) &\approx \frac{1}{2}\mathbb{R}\left\{e^{j\omega_c(t-t_0)}\int_{-\infty}^{\infty}u(\tau)u^*(\tau - t + t_0)d\tau\right\} \\ &= \frac{1}{2}\mathbb{R}\left\{\left[e^{-j\omega_c t_0}\int_{-\infty}^{\infty}u(\tau)u^*(\tau - t + t_0)d\tau\right]e^{j\omega_c t}\right\} \end{aligned} \tag{4.6}$$

if the content inside the square bracket is defined as: $u_0(t)$, then, the output of the MF becomes:

$$S_0(t) \approx \mathbb{R}\left\{u_o(t)e^{j\omega_c t}\right\} \tag{4.7}$$

As deducted from Eq. 4.7, the output of the MF depends on the complex envelope, $u_0(t)$, that is obtained when the complex envelope, $u(t)$, of the narrow passband signal is passed through its

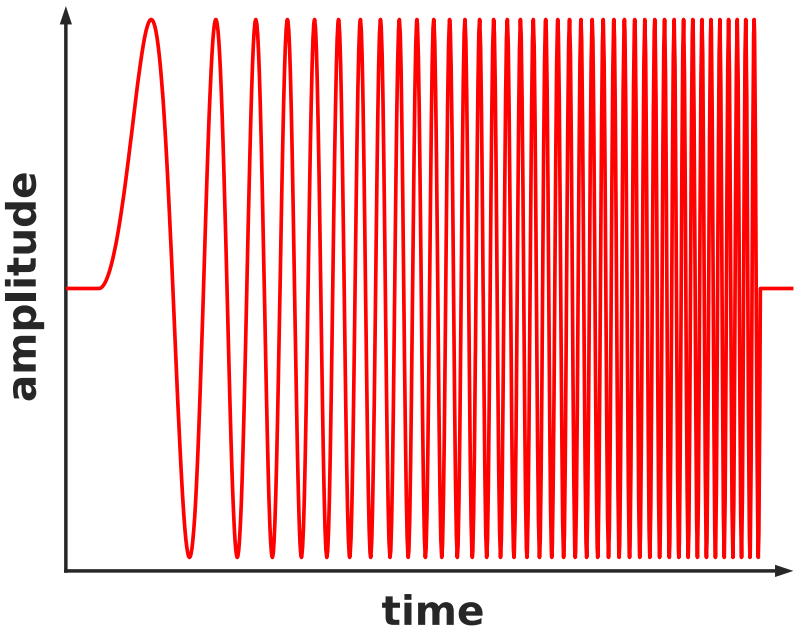

Figure 4.2: Frequency modulation applied to the pulse

MF. It can be concluded that, in the case of a signal formed by a narrow bandpass signal, the output of the MF can be obtained through the complex envelope of the signal used.

The first time that the use of pulse compression was proposed in optical fiber was during the 23-th optical fiber sensor conference (OFS) in 2014 [94]. The fundamental of this technique is based on a pulsed LFM, which is the simplest method to implement pulse compression. In essence, this technique consists of broadening the frequency spectrum of the pulse by applying a LFM inside the pulse. The FM is swept along the duration of the pulse with a constant frequency chirp, as shown in Fig. 4.2. Mathematically, the complex envelope of the LFM pulse is given by:

$$u_0(t) = A \text{ rect}\left(\frac{t}{T}\right) e^{j\beta\pi t^2} \tag{4.8}$$

where A is a constant related to the amplitude, considered equal to $1/\sqrt{T}$ in order to normalize the energy of the pulse to 1. T is the temporal duration of the pulse, rect $\left(\frac{t}{T}\right)$ is the square function and its value is 1 where $|t| \leq T$ and 0 elsewhere. Finally, β is the chirp slope of the frequency modulation which is given by $\beta = BW/T$, being BW the bandwidth of the frequency modulation. When frequency of the pulse is centred at a frequency f_c, Eq. 4.8 is transformed into:

$$s(t) = u_0(t)e^{j2\pi f_c t} \tag{4.9}$$

The output of the MF is given, through Eq. 4.7, by:

$$S_0(t) = \left(1 - \frac{|t|}{T}\right) \frac{\sin(\pi Bt(1 - |t|/T))}{(\pi Bt(1 - |t|/T))} \tag{4.10}$$

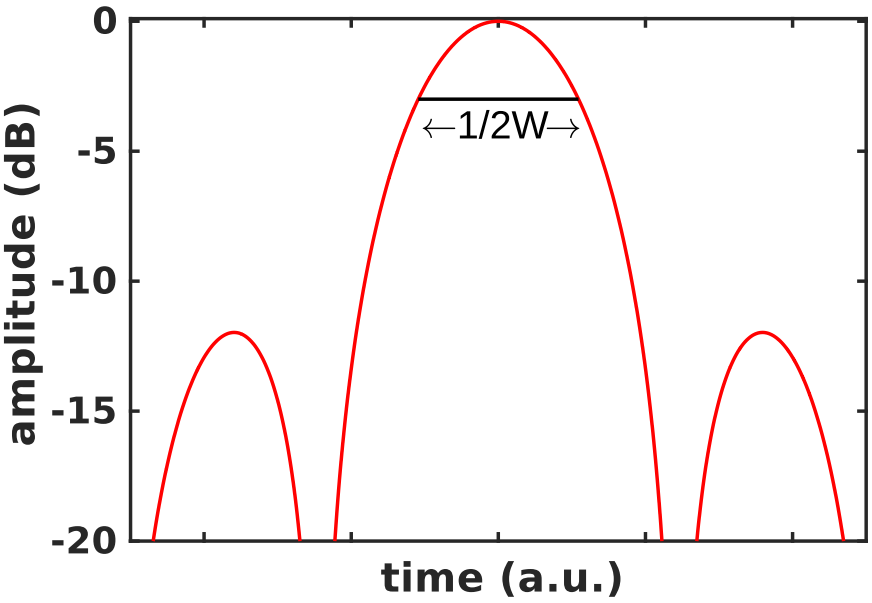

Figure 4.3: Compression of a square pulse with linear frequency modulation when matched filter is used.

when $|t| \leq T$ and 0 elsewhere. As it can be seen in Fig. 4.3, that represents the output of the MF, when a constant-amplitude pulsed LFM signal displays a sinc shape.

As said before, pulse compression permits to break the trade-off between SNR and spatial resolution imposed in conventional OTDR. As Eq. 4.10 shows, the output of MF displays a spatial resolution (at FWHM) equal to the inverse of the bandwidth of the frequency modulation applied to the pulse, independently of the temporal duration of the pulse. The spatial resolution reached by this technique can be deducted from Eq. 4.10 as $1/B$.

However, although OPCR technique implemented in square pulse with LFM is the easiest method to generate pulse compression, it presents a problem that becomes from its nature. Due to its autocorrelation, the compression of a square pulse with LFM presents sidelobes. These sidelobes, that appear in the time-domain and are located in the laterals of the main reflection peak (located at a position off the real reflection) act as a copy of the real reflected event. This degrades the spatial resolution of the sensor and generates crosstalk.

Previously, in radar technology, a number of techniques have been developed in order to alleviate the apparition of sidelobes. Sidelobes come from the autocorrelation of the complex envelope of the used signal. Then, modifying this complex envelope, the amplitude of the sidelobes can be reduced.

4.2.1. Techniques used to mitigate the sidelobes

As aforementioned, the main limitation of pulse compression, when squared-shape pulse LFM is used, becomes from the sidelobes that arise from the autocorrelation of the complex envelope of the pulse. These sidelobes mask the neighbor perturbations, making the detection of two close perturbations impossible. The apparition of sidelobes has motivated the research of techniques to mitigate their presence.

In this section, the main techniques used before to mitigate the apparition of sidelobes are presented. Pulse compression is a technique that was developed in the radar environment decades

ago, and it has been introduced in optical backscattering techniques during the last few years. That is the reason that the major part of the techniques to mitigate sidelobes have been implemented in radar techniques.

Some techniques previously used are based on changing the modulated frequency distribution from linear to non-linear [95, 96]. This solution is based on applying a frequency chirp where the ratio of frequency change vary along the pulse. As a consequence, not all the frequencies will have the same energy, leading to a modification of the complex envelope of the pulse. However, this leads to an increase in the complexity of the system. Another solution used to modify the density of energy of each frequency component of the complex envelope is to modify the amplitude of the envelope of the pulse. Nevertheless, in radar, due to the restrictions imposed by RF amplifiers, which have to work in a saturation regime in order to work efficiently, the amplified pulses must have constant amplitude. In radar, the simpler solution comes from filtering the received signal with weighted windows filter as Hann or Hamming. However, this leads to a loss of SNR due to mismatch loss [93].

In contrast, optical amplifiers (EDFA) work efficiently whatever it is the distribution of the amplitude of the pulse. Taking advantage of the versatility of the EDFA device, it has been seen that the simplest way to modify the density of energy for each electrical frequency of the pulse is to modify the amplitude of the envelope of the LFM pulse.

4.3. Theoretical model of the pulse compression using different amplitude windowing

As mentioned, amplifiers used in the optical domain (EDFA) do not impose a limitation related to the shape of the pulse as RF electrical amplifiers do in radar. This section explains the modification of the amplitude of the optical pulse and its effect in the MF.

The main purpose of the modification is to reduce the sidelobes at the output of the MF of the compressed pulse. As said previously, the output of the MF can be obtained directly from the complex envelope, $u_o(t)$ in Eq. 4.7, as the FFT of its convolution that, in turn, can be understood as inverse FFT of the product of their spectrum.

During the course of this thesis, a study of different amplitude windowing suitable to be applied to the pulse has been performed. As a result, it has been found that a windowing shape that offers an autocorrelation free of sidelobes has to have a smooth profile and avoid sharped edges.

In this case, the windowing profile proposed to implement in this thesis is a Gaussian shape with internal LFM, as indicated in Fig. 4.4. Mathematically, this FM Gaussian pulse is expressed as:

$$G(t) = e^{-\left(\frac{t}{2T_g}\right)^2} e^{j\pi K_g t^2} \tag{4.11}$$

Where the first exponent describes the amplitude of the envelope, T_g is the temporal width between the points of the Gaussian where the amplitude decays a factor, from its maximum, $1/e$. The second exponent describes the frequency modulation applied to the pulse, being K_g is the slope of the frequency chirp.

Once the pulsed signal described in Eq. 4.11 is filtered through a matched filter, it acquires a compressed shape given by:

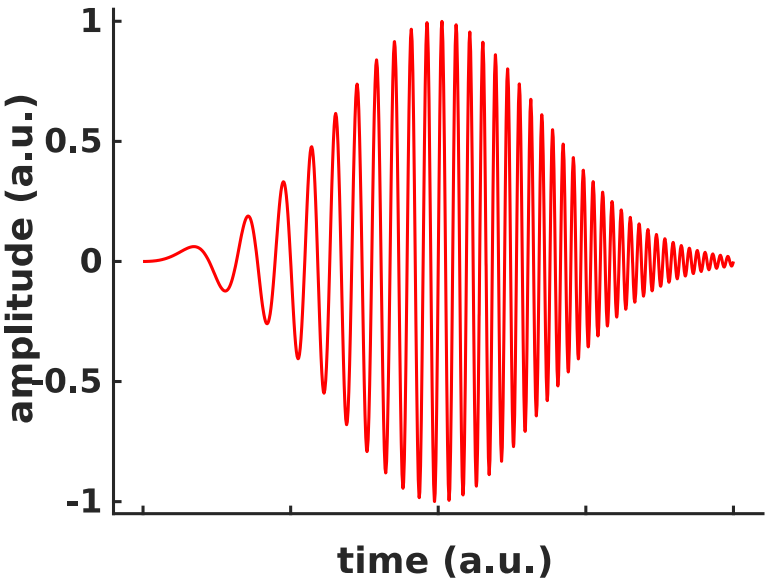

Figure 4.4: Frequency distribution when Gaussian envelope LFM is used.

$$C_g(t) = \int_{\infty}^{\infty} G(\tau)G(\tau - t)d\tau = \frac{K_g T_g}{2} e^{-\left(\frac{K_g T_g t}{2}\right)^2} \tag{4.12}$$

where, as shown in Fig. 4.5, the compression results in a Gaussian shape with a width given by $1/K_g T_g$, the inverse of the bandwidth. In turn, the amplitude of the peak has been increased a value equal to $K_g T_g = B$. From the point of view of the energy, during the compression, in the same way that a width of the pulse is reduced, the amplitude is amplified, being the total area (energy) of the pulse kept constant.

Once the theoretical basis of the technique has been shown, the experimental setup deployed to perform the measurement, in order to demonstrate the behavior of the technique, is described.

4.4. Experimental setup

In this section, the experimental setup used to demonstrate the mitigation of sidelobes is described. The main advantage of this technique is that it requires a minimum alteration of the previous experimental setups used to apply pulse compression techniques.

In Fig. 4.6, a 1550-nm laser emits an optical signal with a linewidth narrower than 15 kHz. The current used to feed the laser is modulated using a ramp (with an amplitude of 2 V peak-to-peak). This modulation is applied just during a time duration equal to the pulse duration, whereas outside this time duration, there is not current modulation applied to the laser. The current modulation generates a variation on the optical frequency carrier of the laser along the pulse duration, applying bandwidth of a 400 MHz. The current used to modulate the wavelength of the laser is supplied by an AWG.

The output of the laser is split into two branches using a 70:30 PM coupler. The 30% of the signal is launched to the lower branch, which is called the reference arm. This signal is used as a LO

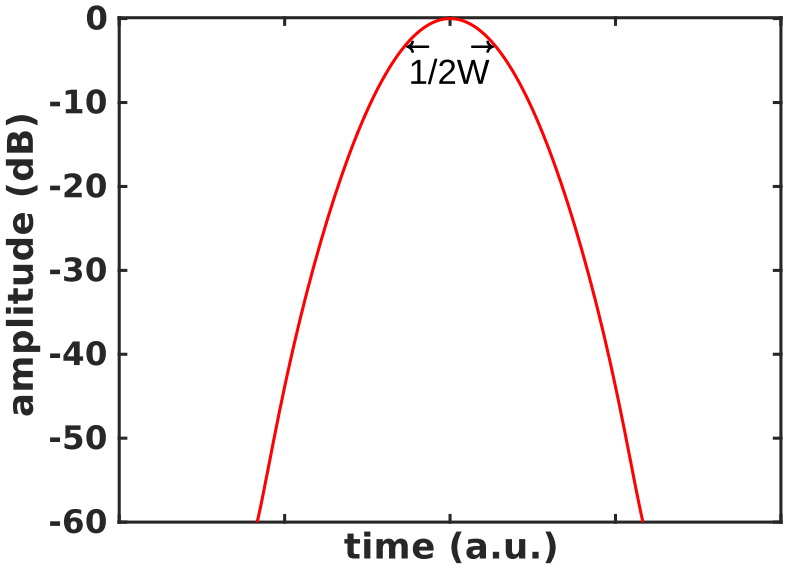

Figure 4.5: Output of the matched filter when compression technique is applied over a LFM with Gaussian envelope pulse.

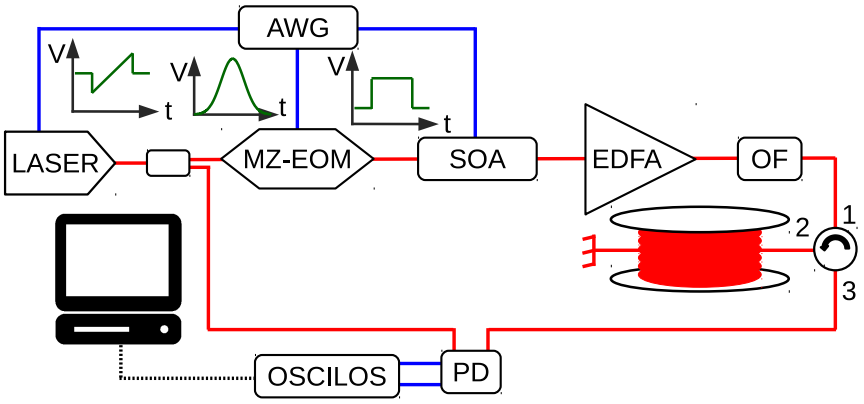

Figure 4.6: Assembled experimental setup in order to develop the optical pulse compression technique. Blue lines indicate electric cables. Red lines depict optical fibers

in the homodyne photodetector. The other output of the coupler (70%) is sent to the MZ-EOM, which is driven by a signal generated by the same AWG used to modulate the current of the laser. This is due to the modulation of the amplitude of the pulse has to be perfectly synchronized with the optical signal to modulate the wavelength. At the output of the MZ-EOM, a SOA working as a 45-dB-extinction ratio (ER) optical switch is used to get rid of the leakage of the pulse wave which is present in the wave due to the low ER ($\sim 30\ dB$) of the MZ-EOM. The presence of the CW due to the low ER of the MZ-EOM introduces additional noise, therefore the degradation of the SNR. The electrical signal that controls SOA is emitted by the same AWG used before since it has to be perfectly synchronized with the signals used to modulate the wavelength of the laser and the MZ-EOM. After SOA, and EDFA boosts the modulated pulsed signal up to a peak power of 19 dBm, which is the limit imposed by the fiber due to non-linear effects such as MI. A 1-nm thin-film optical filter filters the ASE added to the signal by the SOA and EDFA. Finally, the optical LFM pulse is launched into a 50-km FUT through a circulator.

The backscattered signal in the FUT is sent, through the circulator, directly to the homodyne receiver, where it mixes with the LO signal. Before the optical receiver, a polarization controller polarises the optical signal in order to maximize the efficiency of the mixed signals.

The temporal delay between the backscattered signal arm and the reference arm is set in order to avoid the interference of the reflected signal with the wavelength modulation of the laser used to generate the LFM, so the interference uses a constant frequency LO.

After the receiver, the I and Q signals are digitized in an oscilloscope with a sample frequency of 1 GHz. After that, data is stored and post-processed in a computed with a matched filter.

4.5. Experimental results

In order to demonstrate the mitigation of the sidelobes, it has been done a serie of experimental measurements. These measurements describe the method used to evaluate the performance of the technique.

Figure 4.7 shows an example backscattering signal obtained with the system in Fig.4.6 before matched filtering. The power of the back-scattering signal decays exponentially due to the attenuation of the fiber. A strong reflection can be seen at the end of the FUT, which has been induced by connecting a variable optical attenuator (VOA) followed by a short length of fiber that is precisely cleaved to induce a Fresnel reflection. This reflection is used to characterize the pulse, as it is shown below, and its magnitude is controlled by the VOA so that the receiver is not saturated.

Figures 4.8 and 4.9 shows the time-domain amplitude and instantaneous frequency of the pump pulses reflected from the controlled reflection at the end of the FUT for square and Gaussian shapes. This characterization has been performed by detecting the reflected pulses in the homodyne receiver and processing the I and Q components to obtain the complex amplitude information. The temporal width of the pulses has been set to ensure that both pulses contain the same energy, since the average SNR depends directly on the energy of the pulse. The square pulse has a duration of 950 ns, while the Gaussian 1/e-intensity width is 710 ns. In both cases, the pulse leakage is bound by a 1600 ns switching window of the SOA switch. Since both pulses do not have the same temporal duration, the slope of the LFM is not equal in both cases. The square pulse has a slope of 0.25MHz/ns, while the frequency slope of the Gaussian pulse is 0.35 MHz/ns. These complex amplitude measurements have some noise, but this is due to the fact that they are originated by a small reflection at the far end of the FUT. In addition, there is some amplitude distortion which is attributed to the imperfections in the homodyne demodulation due to the tolerances in the optical

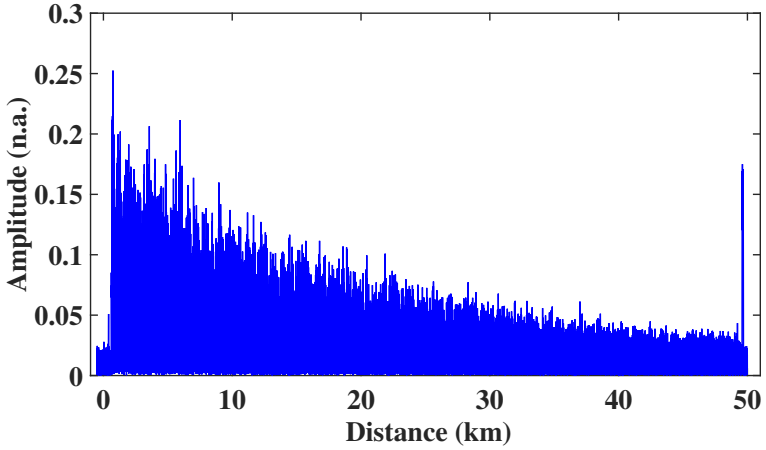

Figure 4.7: measured backscattering signal generated by a pulse

hybrid and balanced receivers.

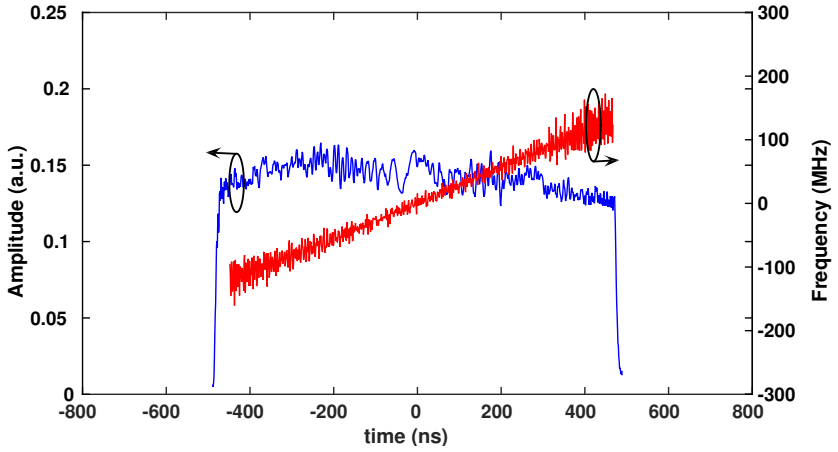

Figure 4.8: Distribution of temporal shape of the envelope (blue line) and instantaneous frequency (red) for square-shaped pulse.

As can be deduced from Eqs. 4.10 and 4.12, the pulse compression obtained with the OPCR method is proportional to the peak-to-peak optical frequency deviation of the applied LFM during the input pulse duration: the larger the total frequency deviation, the greater the pulse compression. At the same time, the frequency deviation of the LFM determines the spectrum of the pulse and, hence, of the backscattering signal. Figure 4.10 depicts the amplitude of the complex spectrum of the signal backscattered from the FUT for square and Gaussian pulses. This is the Fourier transform of the complex amplitude signal obtained from the I and Q components measured in the homodyne receiver. Notice that, for the square pulse, the spectrum takes the approximate shape of a uniform distribution of components over a range of frequencies equal to the peak- to-peak frequency deviation of the LFM. On the other hand, for the Gaussian pulse, the different optical frequencies during the pulse duration are weighted according to the amplitude of the pulse envelope; hence, the pulse spectrum also follows a Gaussian distribution. In these measurements, it can be seen that the 3 dB bandwidth of both signals is approximately equal. This is an important parameter to consider because, as the previous discussion illustrates, the pulse compression that

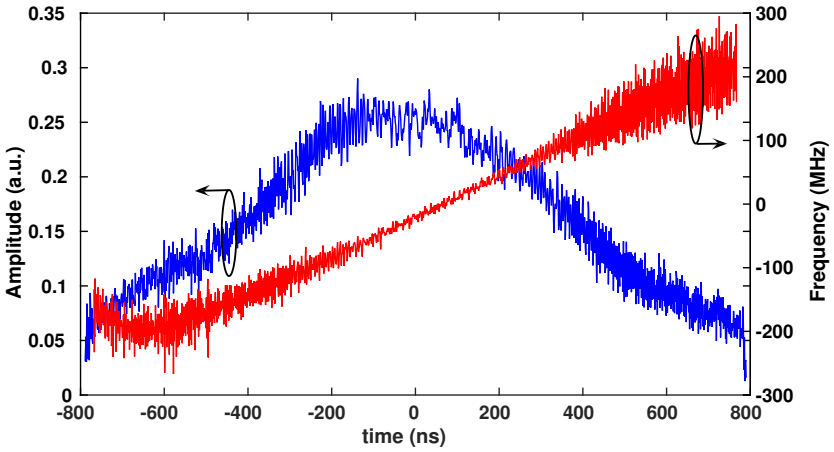

Figure 4.9: Distribution of temporal shape of the envelope (blue line) and instantaneous frequency (red) for Gaussian-shaped pulse.

OPCR can ultimately provide is determined by the electrical bandwidth of the deployed receiver (200 MHz in our case). Therefore, in our system, the LFM modulation of the pulses was adjusted so that the occupied bandwidth of the measured signals was equivalent in order to have a fair comparison between the use of square and Gaussian pulses.

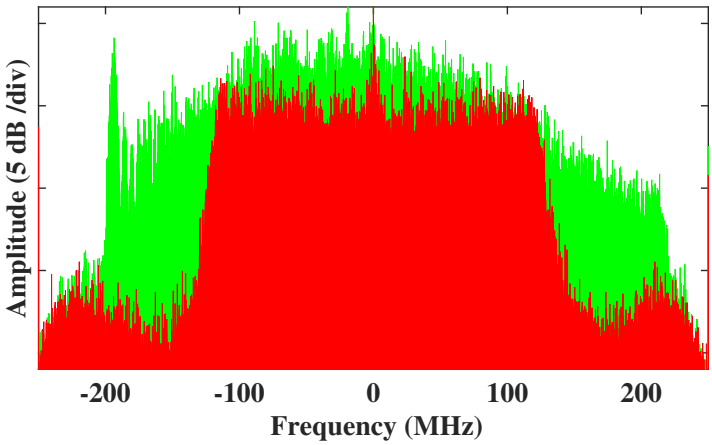

Figure 4.10: Comparative of the spectrum generated by square (red) and Gaussian(red) pulses.

The comparison of the pulse compression obtained with square and Gaussian input pump pulses is depicted in Fig. 4.11. These measurements were obtained applying a matched filtering to the backscattered signal and centering on the end reflection of the FUT. The matched filter for each case used the corresponding input pulse as a template. The spatial resolution, given by the width of the main lobe, is around 34 cm for both compressed pulses. However, as it was expected, the compressed pulse for input square shape has large sidelobes that are 13 dB below the main lobe amplitude. As for the Gaussian, the compressed pulse displays much smaller sidelobes that are 26 dB below the main lobe. These sidelobes actually appear due to the square pulse windowing of the Gaussian pulse generated by the SOA. Moreover, at the location of the sidelobes of the compressed square pulse, the amplitude of the compressed Gaussian pulse drops by 39 dB.

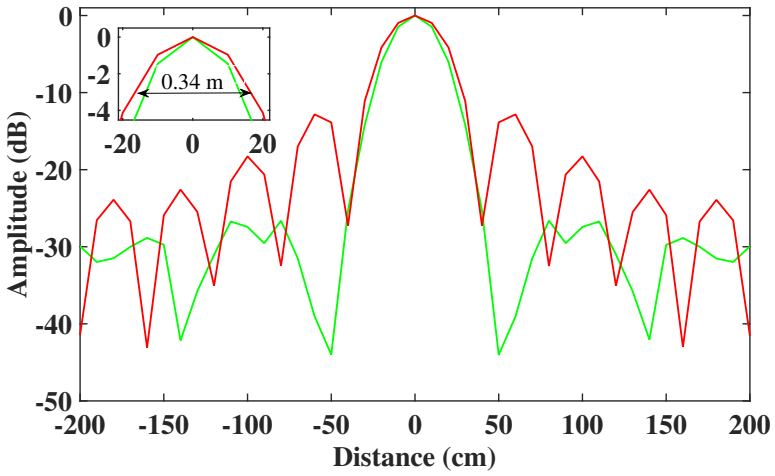

Figure 4.11: Comparative of the pulse compression when square shape (red) and Gaussian shape (green) pulses have been used.

In addition to the previous measurements where the reduction of the sidelobes has been demonstrated, dynamic strain measurements were also carried out to test the performance of our Gaussian OPCR setup. For this purpose, a PFS with a 10-m fiber length was added at the far end of the FUT and was driven by electrical tones to generate a periodical perturbation with 140 $n\varepsilon$ amplitude. Successive backscattering traces at 10 cm spatial sampling were captured and processed for OPCR. Figure. 4.12 depicts example measurements of a differential phase measured within the PFS, i.e., the subtraction of the phase measured in consecutive positions in the fiber inside the PFS. Two measurements are shown with a GL of 10 cm and 1 m, both displaying a sinusoidal shape according to the perturbation applied. For this measurement, the FUT was reduced to 1 km so as to have a pulse time-of-flight which allowed a 13.3 kHz time sampling that provided clear measurements of signal where noise was also visible.

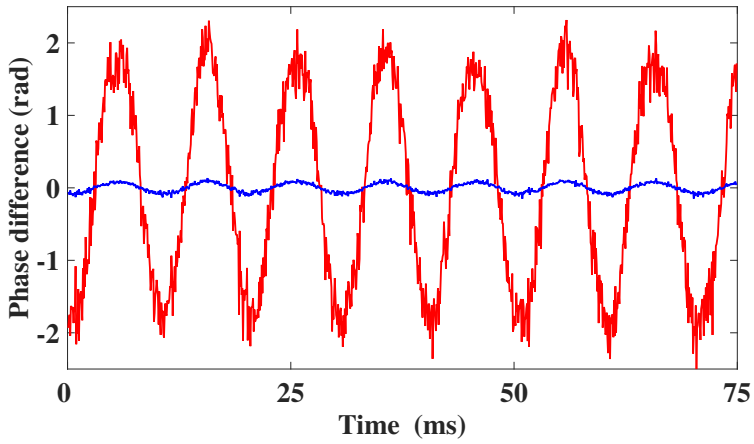

Figure 4.12: Variation of the differential phase when a 100-Hz perturbation is applied over the same location of the fiber using a gauge length of 1-m (red) and 10-cm (blue).

Then the 50 km FUT was used, and the time sampling was reduced to 1.4 kHz due to the pulse time-of-flight. Figure 4.13 shows the FFT of the differential phase measured with a gauge length

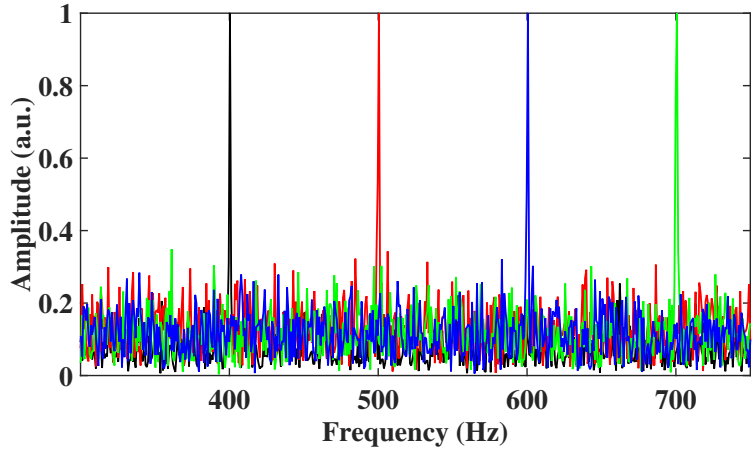

Figure 4.13: FFT of the phase difference measured in the same location of the fiber when a perturbation, at the end of the FUT of 400 Hz (black), 500 Hz (red), 600 Hz (blue) and 700 Hz (green).

of 10 cm for several perturbations with frequencies from 400 to 700 Hz at a location with the PFS at the end of the 50 km FUT. The SNR of the detected signal for every frequency was measured to be around 6 dB without any kind of signal denoising.

Finally, Fig. 4.14 displays the intensity plot of the FFT of a differential phase for the 600 Hz perturbation case for positions around the PFS at the end of the fiber. Notice that the detection of the perturbation is very well confined to its occurrence zone. Some amplitude variation is also apparent within the PFS because of signal fading that is not compensated for in this particular setup.

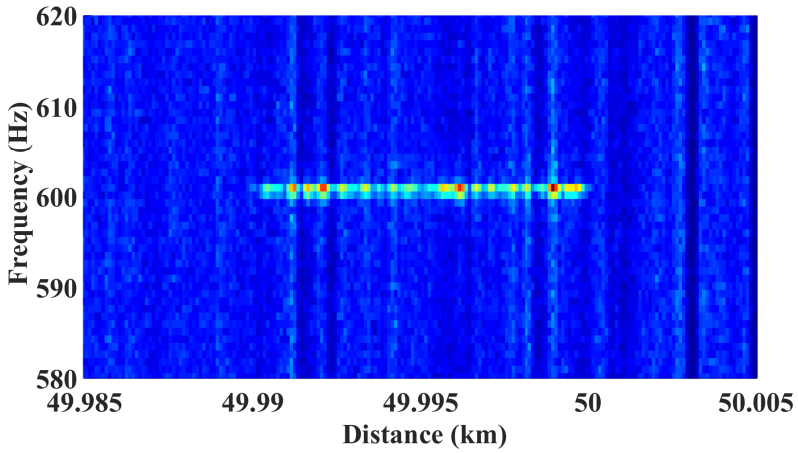

Figure 4.14: Intensity of the FFT of the measured differential phase in the locations around the PFS at the extreme end of the FUT.

An alternative to reducing the compressed pulse sidelobes using our method would be to deploy amplitude weighting of the compressed pulse after detection. This is the method that is normally deployed in radar pulse compression, because the transmitter in those systems does not work in a linear regime and, hence, shaping of the transmitted pulse is inefficient. However, the application of this method to the OPCR would lead to a SNR penalty, since the total receiver filtering is no

longer matched to transmitted pulse. This mismatch loss can be calculated as [93]:

$$SNR_{loss} = \frac{\left(\sum_{n=1}^{N} \omega_n\right)^2}{N \sum_{n=1}^{N} \omega_n^2} \tag{4.13}$$

where ω_n represents the weight of each coefficient, and the total number of coefficients of the windows filter is given by N. When it is applied to a Gaussian shape, the calculated SNR penalty is 2.25 dB. Therefore, in optical systems, where linearity concerns in the receiver do not need to be taken into account, it is more convenient to deploy our Gaussian OPCR method for sidelobe reduction.

4.6. Conclusions

In summary, in this chapter a new a new technique for transmitter pulse shaping in OPCR DAS has been presented. This new technique greatly reduces the sidelobes of the pulse compression leading to a more accurate detection of dynamic events.

The experimental results demonstrate more than 13 dB of sidelobe suppression when using a Gaussian-shaped pulse. Moreover, measurements of dynamic perturbations with a frequency close to the Nyquist limit are performed in a 50 km FUT with 34 cm spatial resolution. This is, to the best of our knowledge, the OPCR DAS with the longest range and largest number of spatially resolved points (50 $km/34\ cm\ =\ 147058 points$) demonstrated to date.

CHAPTER 5

Mitigation of Rayleigh and polarization fading in DAS

5.1. Introduction

As explained during the introduction of this thesis, one of the goals of DOFS is to achieve high sensitivities during their measurement process. There are several applications such as intrusion detection in perimeters or pipelines, monitoring of energy cables, or seismic surveys in oil and gas fields that demand both high sensitivity and fast measurements in order to perform dynamic sensors.

ϕ-OTDR is a technique that exhibits an extremely high sensitivity to external perturbation of the fiber. This high sensitivity is due to ϕ-OTDR uses a light source with a coherence length longer than the length of the deployed pulse. It leads to coherent interference between the different RS. As a consequence of the coherent interference, the resulting amplitude of the reflected signal has a strong dependence on the relative phase optical between the multiple RS.

Nevertheless, this kind of sensors presents a problem related to the linearity of the measurement. Since the resulting interference becomes from multiple RS, its amplitude varies randomly with the amplitude of the applied perturbation, becoming in a sensor able to detect an event but no to quantify it.

In order to prevent this limitation, differential-phase OTDR ($d\phi$-OTDR) sensors (also known as DVS or DAS) were deployed. This kind of sensors is based on measuring the evolution of the optical phase, in each location of the fiber, along time. With that purpose, the phase difference between two points of the fiber is calculated. Several techniques have been implemented to obtain the differential phase. One of these techniques uses an unbalanced fiber Mach-Zehnder interferometer before the photodetector [58]. The GL is given by the extra length of the unbalanced arm of the interferometer. At the output of the interferometer, the backscattering signal has run both arms with different length, resulting in an interference between the reflection of the signal with a separation equal to the GL. The resultant optical signal is sent to a 3x3 coupler which its outputs, with a phase shift of $2\pi/3$ between them, feed three photodetectors. Finally, the differential phase between points separated GL is given by the combination of the three electrical outputs of the photodetectors [59, 60]. Another technique to obtain the differential phase between fiber locations separated GL consists of injecting two pulses with different optical frequencies with a

temporal separation equivalent to the GL, into the fiber [61]. The amplitude of the interference depends on the relative optical phase between both backscattering signals, being modified when a perturbation occurs over the fiber. This technique permits to vary the GL easily by changing the temporal separation between both pulses, but once the measurement is done, the GL can not be modified. A modification of this technique is based on changing the optical phase of the second half of the pulse in consecutive pulses launched into the fiber. In this case, the GL is given by half of the pulse. However, due to the temporal separation between two consecutive pulses is not equal to the time-of-flight of the fiber, the phase variation, due to the perturbation, can not be significant, limiting the performance of this technique for the measurement of high frequency dynamical perturbations. Finally, a technique that uses the differential phase from the measured optical phase of the backscattering signal. This technique is based on amplitude ϕ-OTDR setup with optical phase measurement. With that purpose, the amplitude ϕ-OTDR detection scheme is modified, adding a coherent detection scheme. In the coherent detection, the reflected signal is beaten with a LO provided by the same light source as the sensing signal [64]. Product of the coherent detection, two electrical signals are provided by the detector. These signals, in-phase (I) and in-quadrature(Q) are combined to obtain the phase profile of the reflected signal[64]. By means of the phase difference between two points of this reflected signal, the accumulated phase can be obtained. This accumulated phase depends directly on the amplitude of the perturbation.

However, although $d\phi$-OTDR sensors can detect and characterize the perturbation, they presents a limitation on their performance related to fading. Fading is presented as a sudden and random dropping of the amplitude of the reflected signal, leading to a low SNR, that can have two different origins. The first one is the Rayleigh fading and it is caused by the own nature of the coherent interference between the signals reflected from each scattering centers when the addition of all the optical phasors leads to a destructive interference. As a consequence of the low amplitude of the resultant signal, the SNR drops to low levels, impairing the quality of the measurement in some random points of the fiber. Another source of fading becomes from the polarization mismatch between backscattering signal and LO. The fact that both signals polarizations are not aligned becomes in a loss of mixing efficiency, being 0 when their relative SOP is completely orthogonal [97, 98, 75, 76].

In this chapter, a new technique to prevent the apparition of both fading issue is presented. This technique, developed during this thesis, launches into the fiber, four independent frequency pulses with a different SOP each one. In this way, since four optical frequencies provide four Rayleigh independent responses of the fiber, Rayleigh fading is mitigated. Moreover, each pulse has a different SOP, so their reflected signals will be distributed among all the possible relative SOP with the reference signal. As a consequence, it ensures that, at least, one signal has high mixing efficiency. The performance of the technique is theoretically and experimentally demonstrated, and has been tested measuring a dynamic perturbation at the far end of a 50-km fiber length with any fading [78].

5.2. The problem of Fading in OTDR systems

There are fundamentally two sources of fading of the signal in $d\phi$-OTDR. One of them is caused by the own nature of the coherent interference, and polarization fading originated from the loss of the mixing efficiency with the LO used in the coherent detection due to the polarization mismatch. In this section, the fundamental of problems related to both fading and the solutions proposed are discussed.

5.2.1. Rayleigh fading and techniques to avoid it

As mentioned previously, Rayleigh fading is caused by the own nature of the coherent interference. During the ϕ-OTDR, an optical pulse, conformed by a high coherent light signal, is launched into the sensing fiber. As the pulse travels through the fiber, each RS contained in the fiber length, occupied by the optical pulse, reflects the frontwave of the pulse. The amplitude of the reflected wave by each individual RS is entirely random, in the same way, that the optical phase, that depends on the position of each RS, are randomly located. Therefore, the optical phase is also random equally distributed along the range between 0 and 2π.

Due to RS are randomly distributed, the electric field that is detected in the photodetector is a combination of multiple phasors as follows:

$$E_s(z) = p(z)\sum_k a_e^k e^{j\phi_0^k} = p(z)A_e(z)e^{j\Phi_e(z)} \tag{5.1}$$

where $p(z)$ denotes the relative SOP that will be studied in the next section but, in the context of Rayleigh signal it can be considered constant, and equal to 1, without any loss of generality. a_e^k and ϕ_e^k denote the amplitude and phase of each RS phasor, whereas $A(z)$ and $\Phi(z)$ indicate the random amplitude and optical phase of the set of individual RS detected by the photoreceivers in the position z [99].

The energy from the backscattering waves that arrive to the photodetector defines the SNR of the measurement. It is given by the probability density function of the Rayleigh distribution, P_{BS}, that is proportional to the backscatter optical power, $|E(s)|^2$, and is given as follows [100]:

$$Pr(P_{BS}(z)) = \frac{1}{\overline{P_{BS}(z)}} e^{\frac{\overline{P_{BS}(z)}}{P_{BS}(z)}} \tag{5.2}$$

where $\overline{P_{BS}(z)}$ indicates the mean value of the backscattered power.

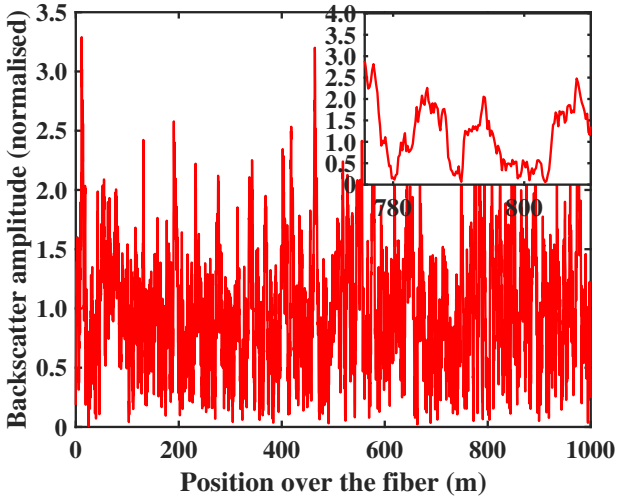

Figure 5.1: Simulation of the backscattering trace with just one wavelength. Inset denotes a detail of the backscattering power profile in the last meters of the fiber.

A simulation of a measured signal given by Eq. 5.1 is shown in Fig. 5.1. This simulation is done using a 1-km fiber length, a 1-mm separation between consecutive RS, a pulse length

of 5 meters and a coherence length longer than the optical pulse. Since the amplitude of the backscattering depends on the addition of multiple phasors with random amplitude and phase, there is a probability that the value of the energy in random locations of the fiber is so small that the SNR becomes too low to provide a trustful measurement. The probability density function of the backscattered power in the simulation is shown in Fig. 5.2. This figure shows the probability of detecting, in some positions along the fiber, a measured value with amplitude so small that becomes in a low SNR. As a consequence, the measurement at this point gives a non-trusty measured value.

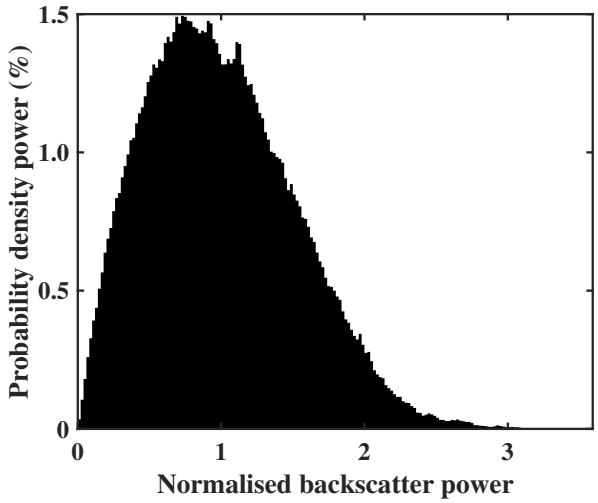

Figure 5.2: Density of probability of the normalized backscattering power when one wavelength is used.

Since each optical fiber has a unique but fixed random distribution of RS, the relative optical phase between the multiple phasors depends strongly on the optical wavelength of the used probe wave. As a consequence, the location of constructive and destructive interference along the backscattering profile is changed randomly when the optical wavelength is modified.

Taking advantage of this fact, a technique to avoid the Rayleigh fading is studied [43, 101]. This system deploys different optical pulses to scan the FUT. Each one of these optical pulses is conformed with a different optical wavelength, as a consequence, the probability of getting a low signal amplitude in the same point of the fiber decays to values close to zero. Then, when Rayleigh backscattering signals from different wavelengths are combined, the points were the amplitude is simultaneously low tend to disappear. More optical different frequency waves imply less probability to get a low amplitude at the same point.

Figure 5.3 shows a simulation of a backscattering trace using the same parameters than the previous simulation but, in this case, three different wavelengths are used. Three wavelengths have been chosen to set a spectral separation longer than the inverse of the pulse so that they are statistically independent. In this case, the pulse has a bandwidth of 20-MHz, so the spectral separation between wavelengths has to be longer than 20 MHz. Since Rayleigh-based sensors are implemented using a third window telecom wavelength, centered at 193.5 THz, when the simulation is run, a separation of 2 GHz from the carrier frequency is applied to the different three optical frequencies used in the simulation. In this simulation, implemented over a 1-km fiber length, the optical fiber attenuation has been neglected.

The results of the simulation depict the Rayleigh backscattering trace for the three optical signals used. All three signals have the same mean power value, and each one of them has statistically the same number of locations where the amplitude of the interference decays to values close to zero, therefore to low SNR. Inset of Fig. 5.3 shows a detail of the backscattering signals generated by all three optical frequencies. It shows that the locations where the amplitude of the coherent interferences drop to values close to zero are not located in the same position when different optical frequencies are used. This means that a combination of multiple used signals in order to avoid the Rayleigh fading.

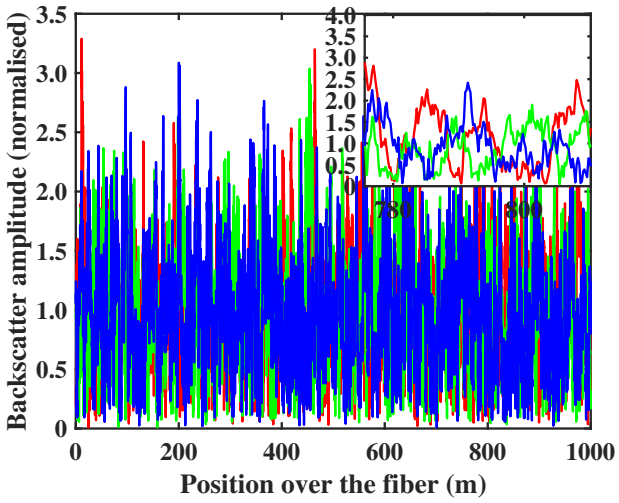

Figure 5.3: Simulation of the backscattering trace when three wavelength are used. Inset shows a detail of the backscattering power profile in the last meters of the fiber.

Fig. 5.4 shows the statistics of the normalized backscattering power of the combination of all three backscattering signals. In contrast to the statistics of a backscattering when a single optical wave is used, in this case, the probability of finding a location with destructive interference, which leads to a zero amplitude, is almost zero. When more that one optical wavelength is used, the distribution of probability density power adopts a Gaussian shape which width is inversely proportional to the number of different optical frequencies and centered at the mean power value. Consequently, the probability of having a too small amplitude becomes almost zero.

5.2.2. Polarization fading

Signal amplitude at the output of a coherent balanced optical receivers presents a dependence on the relative SOP between both signals, that are beaten on the receiver. Given two signals that interfere in an homodine photodetector, it can be perfectly assumed, without loss of generality, that both signals have a defined SOP, as given by Jones notation as follows:

$$\vec{r} = \begin{pmatrix} E_{0x}^{r} e^{j\phi_x^r} \\ E_{0y}^{r} e^{j\phi_y^r} e^{j\psi_r} \end{pmatrix} \tag{5.3a}$$

$$\vec{s} = \begin{pmatrix} E_{0x}^{s} e^{j\phi_x^s} \\ E_{0y}^{s} e^{j\phi_y^s} e^{j\psi_s} \end{pmatrix} \tag{5.3b}$$

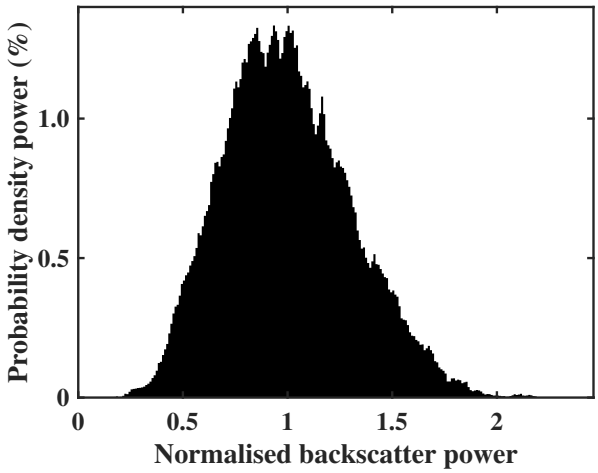

Figure 5.4: Density of probability of the normalized backscattering power when the wavelengths are used.

where $\vec{r}$ and $\vec{s}$ indicate the SOP of the reference and backscattering signal respectively. E_a^b, ϕ_a^b and ψ_a indicate the electric field, optical phase and polarization angle between both axis respectively. In this case, a indicates the x and y axis whereas b denotes the reference (r) and backscattering(s) signals. These signals are combined in the optical detector, and the total electric field, $\vec{E_T}$, is given by both reference $\vec{E_r}$ and signal, $\vec{E_s}$ electric fields as:

$$\vec{E_T} = \begin{pmatrix} E_{0x}^s e^{j\phi_x^s} + E_{0x}^r e^{j\phi_x^r} \\ E_{0y}^s e^{j\phi_y^s} e^{j\psi_s} + E_{0y}^r e^{j\phi_y^r} e^{j\psi_r} \end{pmatrix} \tag{5.4}$$

The total power at the output of the photo-detector is given by $I =< \vec{E_T}\vec{E_T}^{\,*} >$

$$\begin{aligned} I = (&|E_{0x}^s|^2 + |E_{0x}^r|^2 + 2E_{0x}^s E_{0x}^r cos(\Delta\phi_x) + \\ &|E_{0y}^s|^2 + |E_{0y}^r|^2 + 2E_{0y}^s E_{0y}^r cos(\Delta\phi_y + \Delta\psi)) \end{aligned} \tag{5.5}$$

once the alternating current (AC) components of the signal, which contain the information, are kept, Eq. 5.5 becomes:

$$I \approx 2(E_{0x}^r E_{0x}^s cos(\Delta\phi_x) + E_{0y}^r E_{0y}^s cos(\Delta\phi_x + \Delta\psi)) \tag{5.6}$$

where, considering a SMF which ideally does not present a strong and constant birrefringence, $\Delta\phi_x \approx \Delta\phi_y$, that indicate the relative optical phase adquired by both polarizations due to their optical path and perturbation along the fiber. Since $\Delta\phi_x$ and $\Delta\phi_y$ are the cause of Rayleigh interference, thus polarization fading is not affected by relative optical phase between phasors, both $\Delta\phi_x$ and $\Delta\phi_y$ can be considered 0 without any loss of generality. In addition, to extend the generality of this study about the effect of SOP of the optical signals in phase extraction Φ-OTDR, the relative phase between both x and y axes also has been considered, $\Delta\psi$. Eq. 5.6 becomes as:

$$I \propto E_{0x}^r E_{0x}^s + E_{0y}^r E_{0y}^s cos(\Delta\psi) \tag{5.7}$$

from Eq. 5.7 there are extracted some conditions that make the resultant output power becomes too low:

◇ Orthogonal linear relativeSOP

$$E^r_{0x}E^s_{0x} = E^r_{0y}E^s_{0y} = 0$$

◇ Both SOP are circular but in opposite directions

$$\Delta\psi = \pi$$

◇ Independently of values of the electric field, $\Delta\psi$ that meets the criteria

$$\Delta\psi = acos\left(\frac{E^r_{0x}E^s_{0x}}{E^r_{0y}E^s_{0y}}\right)$$

As seen, multiple causes lead to a polarization fading when two electrical waves are combined. Ideally, a possible solution that may mitigate a fading of the power due to polarization mismatch is to insert a polarization controller (PC) at the signal input of the optical photodetector [64]. The use of PC permits to turn the SOP of the signal, increasing the efficiency of the wave mixing. Nevertheless, although this permits to maximize the power locally at the output of the photodetector, SMF fiber presents a small but random birefringence along its length, which leads to a slow random modification of SOP. As a consequence of this slow modification of SOP after propagation of a few meters, the SOP of the signal is still defined but becomes random being totally uncorrelated with its previous SOP. Product of this uncorrelation between SOP of positions along the reflected signal that arrives at the balanced photodetector, the use of a PC becomes an impractical solution when sensing fiber link exceeds a few hundred meters.

Another solution to face the issues linked to polarization fading is based on duplicate the detection scheme, one for each polarization. This system uses a polarization diversity coherent receiver in which each polarization from both signals is sent to a different optical photodetector in order to maximize the efficiency of waves mix for each polarization [75, 76]. This kind of photodetectors can have multiple different configurations: integrated if all the system is inside the same device or non-integrated if the system is divided into multiple devices. In essence, all of them have the same principle of work. Both signals reference (LO) and backscattering signal (s) are split into two polarizations. Each polarization of both signals is sent to beat in the same balanced photodetector (BPD). Once in each BPD, the signal is processed as described in Sec 1.3.4. Note that LO signal has to be equally split in both polarizations to maximize the possible interaction with both polarizations. With this purpose, reference light must be injected into the polarization beam splitter (PBS) with an orientation of 45° using a PC if necessary [74].

After both polarizations of both signals have been beaten, AC of each output are measured and processed. The resultant amplitude and phase are derived from I_x, I_y, Q_x and Q_y, that represents I and Q signals for both x and y polarization as follows [76]:

$$A_s(t) = \sqrt{I_x^2 + I_y^2 + Q_x^2 + Q_y^2} \tag{5.8a}$$

$$\phi_s(t) = atan\left(\frac{Q_x + Q_y}{I_x + I_y}\right) \tag{5.8b}$$

Although the use of polarization diversity detection scheme provides a measurement with a considerable reduction of fading of polarization, it represents an increase of the complexity of the

system. An additional receiver module and receiver module is needed and the volume of data to the stored and processed is doubled. All these issues present a disadvantage when the system is implemented in a real scenario since more complexity of the system is translated into a more expensive system.

During this thesis, a new method to mitigate both Rayleigh and Polarization fading has been presented. In the next section, this new technique is explained, studied in detail, and experimentally demonstrated.

5.3. New technique to mitigate fading in ϕ-OTDR systems

As said in the previous section, fading is an important issue to face in Φ-OTDR sensors. Fading in Φ-OTDR becomes from two different sources: coherent interference and polarization mismatch. In contrast with other problems that affect ϕ-OTDR such as attenuation, fading is completely random both in position and magnitude. As a consequence of that, applied techniques to face fading need to work in the whole fiber length.

The technique we introduce mitigates both fading simultaneously. The basic idea of the system consists of launching sequential pulses with different optical frequencies and polarizations. In addition, each pulse is performed using a linear FM, applying OPCR technique, and, therefore, enhancing the SNR of the signal as it is demonstrated in chapter 4.

Fig 5.5 displays the fundamentals of the technique. Schematically, four pulses are launched consecutively, with a time-delay much smaller than the time-of-flight of the pulse in the fiber. Each pulse has a different optical frequency, being the spectral separation between them more than the inverse of their time duration to ensure the statistically independent fading [43]. Besides, each pulse has a different SOP, distributed along the Pointcaré sphere. This ensures that, at least, three of the backscattering signals do not experience polarization fading simultaneously in the same location of the signal. A possible distribution of the SOP would be $\theta_1 = 3\pi/4$ $\theta_2 = \pi/2$ $\theta_3 = \pi/4$ $\theta_4 = 0$.

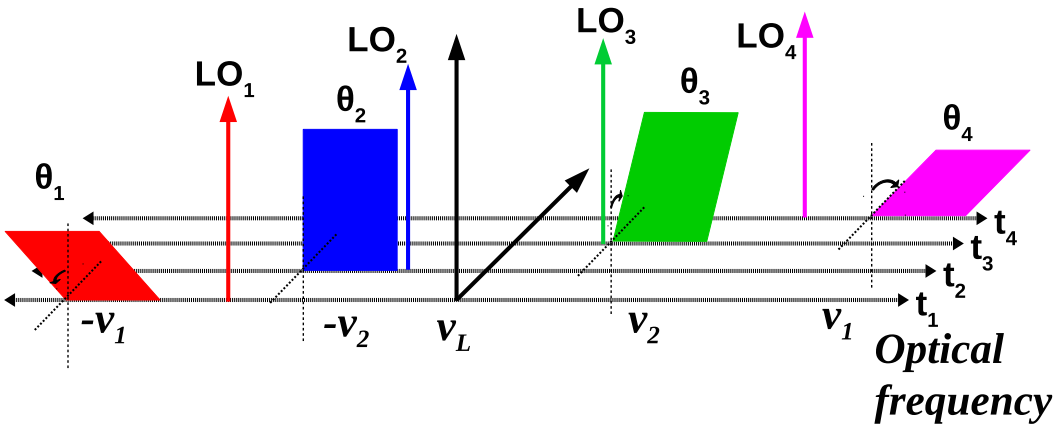

Figure 5.5: Schematic representation of time, frequency and polarization of the four pulses deployed in the technique.

The low birefringence of the fiber turns the SOP of the signals randomly. All four SOP experience the effect of the same birefringence, so their relative SOP are kept constant. In this way, using the combination of four Rayleigh independent signals with different, but constant, relative

SOP between them, in a given position of the fiber there will be, at least, one reflected signal that does not suffer any kind of fading.

The four signals are distributed as four pulses that are sequentially launched. Each pulse is linearly frequency modulated and, as explained previously, their central frequencies are separated by more than the reciprocal of their duration to be statistically independent [43]. The expression for the sequence of pulses sent into the fiber is as follows:

$$S_T = \sum_{i=1}^{4} S_i(t) = \sum_{i=1}^{4} A_i(t) e^{j[(\omega-\Omega_i)+k_i(t-(i-1)\tau))(t-(i-1)\tau]} \tag{5.9}$$

where i is the pulse number, Ω_i represents the electrical central frequency of each pulse, k_i the slope of the frequency chirp of each pulse and the temporal delay of each pulse is denoted by $(i-1)\tau$ where τ is the temporal space between two consecutive pulses.

The reflected signal generated by each pulse is formed by multiple overlapped copies of the original pulse. These copies come from the reflection of the pulse along the fiber. Once these copies arrive to the balanced photodetector, the whole signal is beaten with the LO signal. All four reflected signals are beaten with the four local oscillators at the same time, so the electrical measured signal, after the frequency beaten, can be represented as:

$$S_T^e = \sum_{i=1}^{4} \sum_{m=1}^{4} A_{ik}^e(t) e^{j(\Omega_{im}^e+k_i(t)(t-(i-1)\tau))(t-(i-1)\tau)} \tag{5.10}$$

where i and m denote the pulse, and local oscillator, Ω_{ik}^e is the electrical frequency separation between the i-th pulse and m-the LO. Note that, due to the limited bandwidth of the balanced photodetector, all the beaten frequencies Ω_{im}^e that exceed the bandwidth of the photodetector are not in practice detected, so when frequencies are adequately chosen to have a difference greater than bandwidth, in Eq. 5.10, $i = m$ becoming as

$$S_T^e = \sum_{i=1}^{4} A_i^e(t) e^{j(\Omega_i^e+k_i(t)(t-(i-1)\tau))(t-(i-1)\tau)} \tag{5.11}$$

Eq. 5.11 represents the measured signal for each one of the four pulses. In practice, this signal comes from the multiples reflections suffered by all the pulses along the whole fiber, but for this mathematical demonstration, there is not a loss of generality if it is considered as a single individual copy of each pulse. After the measurement, a FFT is applied to the signal formed by the four signals. It permits to separate the spectrum of the signal generated by each pulse in order to be analyzed separately.

Finally, as explained during section 5.1, this system also combats polarization fading. To that, each one of the pulses is launched into the fiber with a different SOP. One option to deploy the different SOP in each pulse would be to use an electrically-programmable polarization controller. However, they are not fast enough to change the relative polarization of pulses closely separated in time.

Instead of using an electrical-based system to modify the SOP of each pulse, in this thesis, we propose to use a passive all-fiber device. This device is based on the use of a differential group delay (DGD) induced by both axis of a PM fiber between signals of different optical fequencies [102, 103].

The DGD device is based on a segment of PM fiber where the optical signal is introduced with a relative orientation of 45° from the ordinary axis. Once inside the PM fiber, each optical frequency experiences a DGD in each axis, as a consequence, the SOP of each signal is rotated a

relative polarization angle proportional to its optical frequency. At the output of the DGD, the relative angle of polarization, in function of the frequency, is given by:

$$\theta(\Delta f) = \pi \Delta\tau \Delta f \tag{5.12}$$

where $\Delta\tau$ is the differential group delay that the birefringence of the PM fiber induces between both optical frequencies separated Δf. From Eq. 5.12, it is extracted that when frequency separation between both waves fits $\Delta f = 1/2\Delta\tau$, at the output of the DGD these both frequencies will have an orthogonal SOP. Then, choosing the precise relative frequency separation between these four waves, the desired distribution of SOP can be obtained.

When the effect of the polarization mismatch [104] is introduced in Eq. 5.11, it becomes as follows:

$$S_T^e(t) = \sum_{i=1}^{4} cos^2(\varphi(t) + \theta_i) A_i^e(t) e^{j(\Omega_i^e + k_i(t)(t-(i-1)\tau))(t-(i-1)\tau)} \tag{5.13}$$

where $\varphi(t)$ is the relative SOP between the pulse 1-st and the LO, and θ_i is the relative SOP between pulse 1-st and i-th.

If θ_i are correctly chosen, in order to cover uniformly all the possible polarizations such as $\theta_1 = 0$, $\theta_2 = \pi/4$, $\theta_3 = \pi/2$, $\theta_4 = 3\pi/4$, then the terms that determine the efficiency of the mix, due to the polarization mismatch, are compensated in pairs. In this case, it becomes as $cos^2(\varphi(t) + \theta_1) + cos^2(\varphi(t) + \theta_3) = cos^2(\varphi(t) + \theta_2) + cos^2(\varphi(t) + \theta_4) = 1$.

In summary, scanning the FUT using four signals statistically Rayleigh independent and, also, with four different SOP, that are complementary (orthogonal) in pair, it is ensured to avoid any fading as it will be experimentally demonstrated in the next section.

5.4. Experimental setup

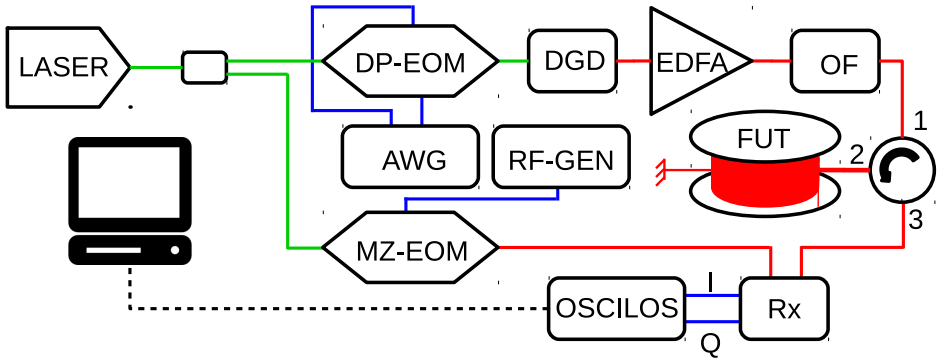

Figure 5.6: Experimental setup deployed in order to demonstrate the technique. Green and red lines indicate PM and SMF fiber respectively. Blue lines indicate electric cables.

Fig. 5.6 displays the experimental setup used to demonstrate fading mitigation. This is dϕ-DVS that implements OPCR using LFM of the pulses and matched filtering [72]. A laser emits a continuous wave with a narrow linewidth of less than 15 KHz. The signal is separated by a coupler in two branches. In the upper branch, a dual parallel-electrooptic modulator (DP-EOM) is configured as an optical single-sideband suppressed-carrier modulator using an 90-degree RF

hybrid coupler to drive the two inputs of the modulator. In turn, the two inputs of the hybrid coupler are driven by an AWG that sequentially generates four 6-μs pulses at 11 GHz and 8.22 GHz. The pulses are separated in time by 7-μs. The bandwidth of each pulse is broadened to 90-MHz by linear modulation of their instantaneous frequency so that after matched filtering the equivalent pulse duration is reduced to a spatial resolution of 1.1 m. The AWG sets the signals sent to each input of the RF hybrid coupler so that the final result is that the four pulses are modulated onto sidebands separated by -11 GHz, -8.22 GHz, +8.22 GHz and +11 GHz, respectively, from the laser frequency. Then, this multi-sideband signal is feed to a DGD implemented with a length of high-birefringence fiber adjusted to obtain a relative delay of $\Delta\tau = 26$ ps between its axis. The optical signal is introduced in the DGD with 45° linear polarization so that it is equally split between its two polarization axis and the relative polarization of each sideband at its output is rotated by an angle $\theta(\Delta\tau) = \pi\Delta f\Delta\tau$ [103]. This makes the pulses located at -11 GHz, -8.22 GHz, +8.22 GHz and +11 GHz to be rotated by 51.48°, 38.52°, -35.25° and -51.48°, respectively. This means that the first and third pulses become orthogonal as well as the second and fourth and it ensures that only one of the four signals can be simultaneously affected by a serious polarization fading. Finally, an Erbium-doped fiber amplifier EDFA followed by an ASE OF boosts the power of the pulses to 19 dBm before injection into a 50-km FUT. A PFS with 10 meters fiber length was added at the far end of the FUT to perform dynamic measurements of vibration. The reflected signal from the fiber is feed to a 250-MHz homodyne receiver whose LO input od the receiver is fed by a MZ-EOM that is biased at minimum transmission and driven with two pure RF tones to generate a double-sideband suppressed-carrier signal with 4 tones located at 8.838 GHz and 10.949 GHz. Each of this tones acts as LO for the detection of one of the pulses. Finally, the I and Q components at the output of the receiver are digitized by an oscilloscope and processed in a computer. First, the signal is digitally filtered to separate the spectral components of the backscattered signals corresponding to each pulse, which are centered at -163, -51, +51 and +163 MHz, respectively. Then, they are compressed individually by matched filtering.

5.5. Experimental results

First, we checked that the polarization induced in the pulses was correct. With this aim, a polarization controller and a polarizer was provisionally installed after the DGD to test the suppression of the different sidebands as the polarization was changed. A polarization of more that 20 dB was measured for all pulses.

Then, the polarization fading of the backscattered signals along the fiber was measured. For this, we installed a PC at the signal input of the homodyne detector that was used to generate random variations of SOP in time. Fig. 5.7 depicts the variation of the amplitude of the reflected signal from one of the pulses coming from 3 different reflections in the fiber: input connector (red line), connector at the PFS (green line), and at the end of fiber connector (blue line). Notice that, as expected, each amplitude varies independently due to the polarization evolution in the fiber. Hence, it is demonstrated that polarization fading for all positions in the fiber can not compensated simultaneously by adjusting the output SOP. Fig. 5.8 demonstrates the compensation of polarization fading with the four pulses for the reflected signals from the connector at the far end of the fiber. Notice that the signals from the different pulses have different amplitude variation with the random change of polarization in a 2-s interval. However, the amplitude obtained combining the four pulses is almost flat, hence, the polarization fading is shown to be compensated.

Finally, dynamic measures have been performed in order to test the improvement in the phase

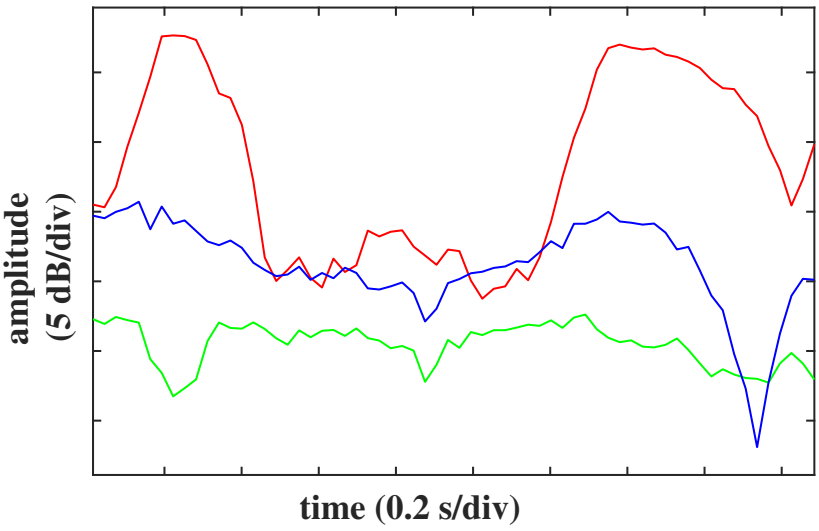

Figure 5.7: Random variation of the amplitude of backscattering signal related to the SOP of the same pulse along the length of the fiber.

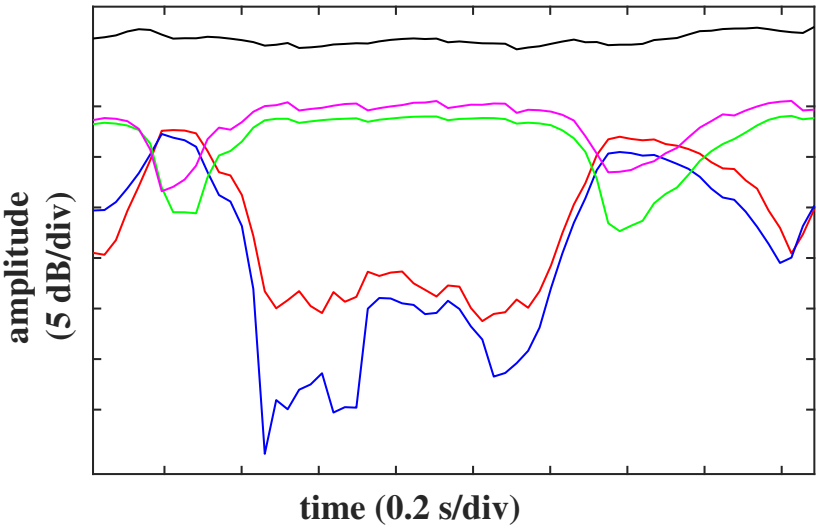

Figure 5.8: Variation of the amplitude of the backscattering signal related to the SOP of the four pulses in the same location of the fiber.

detection brought by fading compensation. Fig.5.9 depicts time-domain measurements of differential phase using a short fiber of 2.2 km. The frequency of the signal applied to the PFS was 25 Hz and the amplitude was 138-$n\varepsilon$ which translates to approx. 9 rad at the operating wavelength in the 10 meters of the device. The figure depicts the phase difference measurement with a gauge length of 12 m for the backscattered signal for each of the four pulses and their combination. Notice that for pulse 1 and pulse 2 the measurement is rather noise whereas for pulse 3 and pulse 4 was much cleaner. This is explained by polarization fading: the backscattered signal from pulse 1 and 2 have a similar polarization (approx. 13° difference when they are linearly polarized) that is experiencing polarization fading in this measurement. Nevertheless, the phase difference obtained by combining the four pulses is cleaner because the backscattered signal from pulses 3 and 4, which is also similar polarized (also separated by approx.13° for linear polarization), is orthogonal to the fading. Therefore, this demonstrates that the system is able to compensate the polarization fading. Moreover, the phase-difference amplitude matches the nominal vibration amplitude quite well.

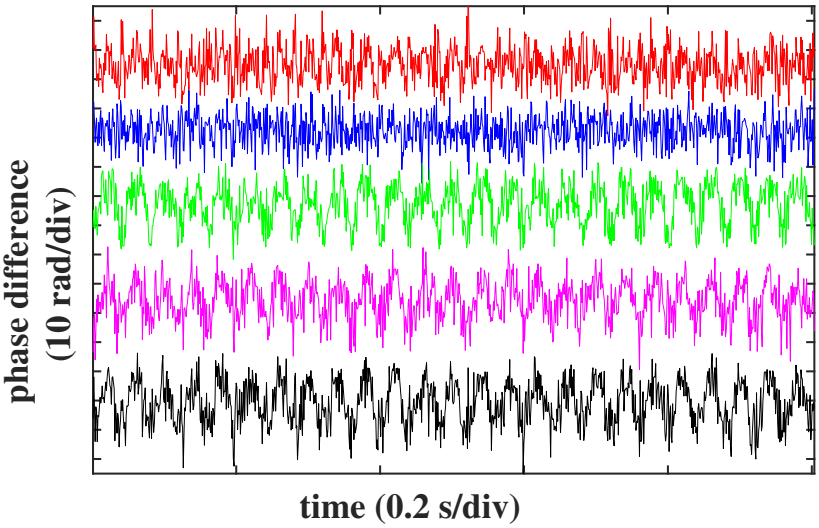

Figure 5.9: Amplitude of the phase measurement in each signal.

Finally, Fig. 5.10 depicts measurements of a 500-Hz vibration with the PFS located at the end of the 50 km of fiber. In this case, the measurements are shown in the frequency domain (after FFT) because the vibration frequency is closed to the Nyquist limit imposed by the time-of-flight of this fiber length, hence few samples per cycle are obtained. The figure displays an intensity plot of the FFT of the differential phase measured with a gauge length of 12 m for locations relative to the location of the PFS at the end of the fiber. Notice that the perturbation is clearly discernible.

5.6. Conclusions

In conclusion, we have demonstrated a method to simultaneously compensate polarization and signal fading in dϕ-DVS sensors. This has the main advantage of reduced complexity compared to previous systems relying just on an all-optical low cost device to achieve polarization diversity instead of requiring the hardware duplication involved in systems that deploy polarization diversity receivers. The system has shown good performance when implemented in long-range measurements with an OPCR setup.

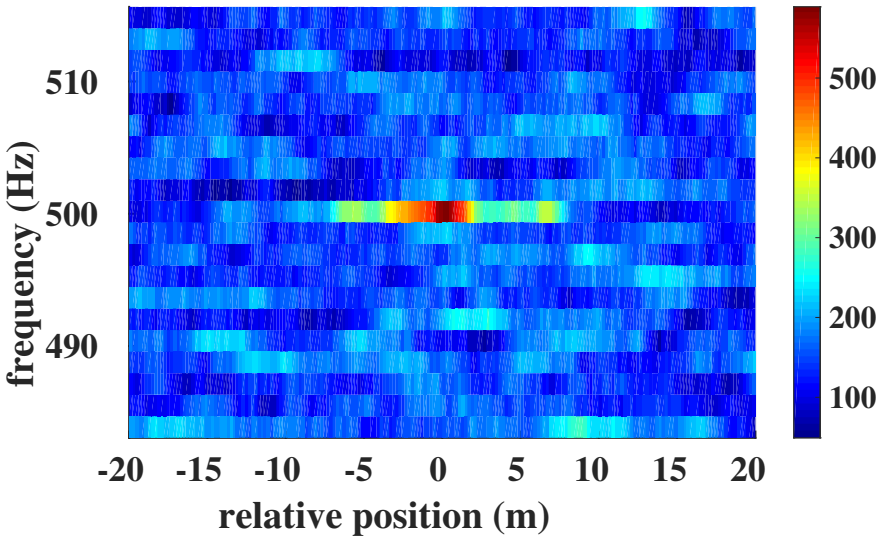

Figure 5.10: Intensity of the FFt calculated over the combination of four measured signals.

CHAPTER 6

High Dynamic range measurement in DAS

6.1. Introduction

Among DOFS, ϕ-OTDR offers extremely high sensitivity. ϕ-OTDR is based on the measurement the reflected signal, whose local variation in the time indicates the existence of a perturbation. However, although ϕ-OTDR deploys a strong sensitivity to detect a dynamical perturbation, the resultant amplitude of the reflected measured signal does not variate linearly with the amplitude of the perturbation. Therefore, it makes a sensor not able to characterize the amplitude and frequency of a dynamical perturbation.

To face this limitation, ϕ-OTDR with phase recovery was introduced [64]. The optical phase, in contrast with amplitude, variates linearly with the amplitude of the applied perturbation over the fiber. Among the multiple techniques used to recover the optical phase, in one of them the reflected signal in the FUT is sent to a 90° hybrid homodyne detector where is beaten with a reference signal, known as LO. The amplitude and optical phase of the reflected signal are calculated from the electrical outputs of the balanced detector I and Q, as shown in section 1.3.4 of this thesis.

In addition to phase recovery, the balanced homodyne detector also permits to enhance the SNR of the measurement signal due to the beat with a higher-power LO signal. Moreover, techniques such as pulse compression have been implemented to increase the SNR of the measurement [105], as discussed on chapter 4 of this thesis. However, phase recovery using coherent detection also brings problems linked to polarization fading. When two signals are mixed, the efficiency of the interference is given by the relative SOP between both signals. Also, Rayleigh fading, which occurs in all kind of ϕ-OTDR sensors degrades the SNR in some locations of the signal when the interference of the signals backscattered from the multiple scattering centers within the optical pulse becomes destructive. Chapter 5 of this thesis describes a solution to compensate both types of fadings [78].

Finally, another critical limitation that constrains the performance of ϕ-OTDR based on optical phase extraction is related to the maximum amplitude of the perturbation that can be measured. In ϕ-OTDR with phase recovery, the variation of the phase along the measurement depends directly on the amplitude of the perturbation which is deducted from the variations of the phase between

two consecutive measurements. As a consequence, the maximum slew rate is limited to π-rad value between two consecutive samples [106], limiting the performance of the sensors in some applications such as structural health monitoring in aircraft wings.

During this chapter, a technique that avoids the limitation imposed by the maximum amplitude and frequency of the perturbation that can be measured is presented. First, this technique is theoretically studied, then a set of experimental tests have been done in order to demonstrate its potential. The technique uses the phase difference between both polarized signals of a PM fiber in order to obtain a phase profile that follows the perturbation shape but with an amplitude proportional to the refractive index difference between both PM axes. In addition, since both measured polarization signals are statistically Rayleigh uncorrelated, the Rayleigh fading can be avoided using a combination of them.

6.2. The problem of ambiguity in the phase

In the introduction of this chapter, some of the problems that constrain the performance of ϕ-OTDR systems have been addressed. Enhancement such as the increment of the SNR without harming of the spatial resolution have been discussed in chapter 4, whereas the solution of the problem that presents both kinds of Rayleigh and polarization fading were presented in chapter 5. In this chapter, the problem related to the limitation imposed by the maximum amplitude of the perturbation that can be measured in ϕ-OTDR with phase recovery is addressed. First, the mathematical description of the problem is introduced as well as the proposed solution to increase the maximum amplitude of the perturbation that can be measured. In addition, use of perfect periodic autocorrelation (PPA) codes is introduced in order to get a good peak side-lobe ratio (PSR).

In ϕ-OTDR, the measurement of amplitude imposes a limitation since it does not variate linearly with the magnitude of the perturbation. As a consequence, the perturbation can be detected; nevertheless, it can not be characterized. In order to avoid this limitation and extend the system to DAS measurements, recovery of the phase was introduced [64]. Both electrical output signals, I and Q, of the detector, are combined in order to obtain the backscattering optical phase signal along the fiber in the same pulse measurement. Once the phase profile generated by each pulse propagated into the fiber is measured, the differential phase is calculated by the phase subtraction between two points separated a distance equal to GL. Differential phase profile in the same point of the fiber indicates the accumulation of phase due to the perturbation over the fiber. This differential phase follows the shape of the perturbation. Then, performing consecutive measurements, the evolution of the differential phase in the same location of the fiber, between consecutive measurements, gives the temporal evolution of the mechanical perturbation.

Nevertheless, a limitation on the performance arises when phase variation between two consecutive measurements exceeds the value of π. Since the value of the phase presents an ambiguity when the phase value changes an amount larger of π, the unwrap function begins to experience a malfunction [106].

Two main causes contribute to the generation of the ambiguity of the measured phase, as shown in Fig. 6.1. On the one hand, there is the own amplitude of the perturbation, which is linked to a bigger phase variation between two consecutive samples. When the amplitude is increased, phase variation, in a period of time between two consecutive samples may exceed the value of π. On the other hand, the phase variation between two consecutive samples, $\Delta\tau$ is proportional to the frequency of the perturbation. Bigger frequency of the perturbation implies a bigger slew ratio,

which is translated to a larger amount of phase change between two consecutive samples.

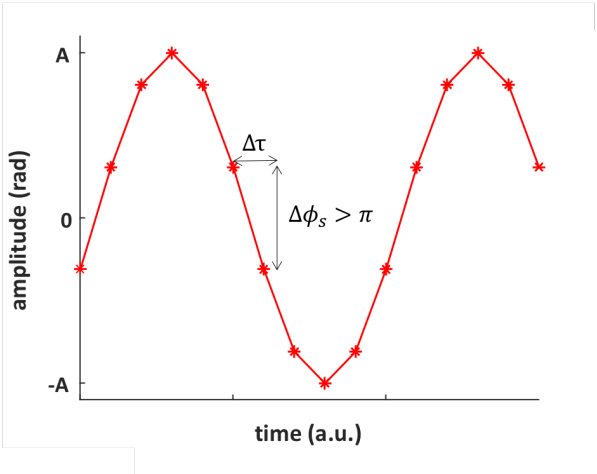

Figure 6.1: Theoretical measured sinusoidal perturbation. Stars indicate the sampled points by the sensor.

the maximum amplitude, A, that can be measured is obtained from the phase variation between two consecutive samples equal to 2π. Given a sinusoidal signal, $S(t)$, with a frequency of the perturbation f_p:

$$S(t) = Asin(2\pi f_p t) \tag{6.1}$$

the maximum slew ratio is given by the maximum value of its first derivative:

$$\frac{d}{dt}S(t) = A2\pi f_p \tag{6.2}$$

the phase change between two consecutive samples is given by $S'(t)\Delta\tau$:

$$\pi = A2\pi f_p \Delta\tau = A2\pi f_p \frac{1}{f_s} \tag{6.3}$$

then the maximum amplitude of the perturbation before system begins to fail becomes as:

$$A = \frac{f_s}{2f_p}\ rad \tag{6.4}$$

Fig. 6.2 displays a simulation of the measured phase when a sinusoidal perturbation with an amplitude $A = f_s/f_p$, being $f_s = 100\ Hz$ and $f_p = 1\ Hz$, has been applied over the fiber. The red line indicates the simulated measurement of the perturbation when the amplitude is equal to the maximum amplitude before the system begins to fail, as described in Eq. 6.4. Green and blue lines show when unwrap algorithm begins to fail because the amplitude of both signals exceeds the maximum amplitude, having the green and blue signals an amplitude 1.01 and 10 times bigger than the maximum amplitude that sensor admits. As expected when the amplitude of the perturbation begins to be bigger than the maximum allowed amplitude, the reconstruction of the perturbation by the system begins to fail in the maximum slope point. As a consequence of these mismatch between real and measured perturbation, the measured perturbation displays a smaller amplitude than the real one. Moreover, when the amplitude exceeds the maximum amplitude significantly, the measured perturbation can not be recovered, losing its shape completely.

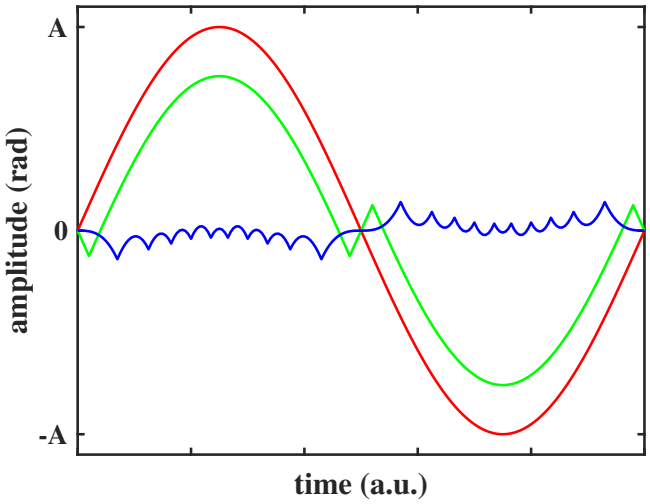

Figure 6.2: Simulation of the measurements of different amplitudes of the perturbations.

In order to prevent this limitation of the maximum amplitude that the system can measure, different techniques can be applied. The first and more obvious solution to this issue is to increase the sampling frequency of the sensor since it is translated to a reduction in the phase variation between two consecutive measurements. However, this solution is limited by the characteristics of the acquisition equipment and, ultimately, by the length of the fiber, which determines the maximum usable sample frequency as the inverse of the time-of-flight of the pulse. Due to the dependence of the sampling frequency with the length of the fiber, Eq. 6.4 can be expressed in terms of the length of the fiber, L in meters, becoming as:

$$A = \frac{1}{2 f_p L 10^{-8}} rad \tag{6.5}$$

Another solution proposed in this thesis is based on the measurement of the phase difference between two phase profiles with two optical signals with slightly different propagation constants. This reduces the sensitivity of the sensor to the perturbation in the fiber, and as a consequence, the amplitude of the measured phase. Therefore the amount of phase between two consecutive points can be increased. In the technique that we have devised, both phase profiles are obtained from the backscattering signal simultaneously generated in both axes of PM fiber. As Fig. 6.3, the probe signal is introduced at an angle of 45° from its principal axis, being equally split between each polarized axis. Finally, the two polarised backscattered signals are separated using a polarization diversity photodetector. Since each signal is forced to be transmitted through one of the axes of a PM fiber, the accumulated optical phase by each signal is proportional to the index of refraction of the axis. As a consequence, the differential phase between both signals is proportional to the difference of the index of refraction between ordinary and extraordinary axes of the PM fiber.

As in a direct phase analysis, phase difference between points distanced the GL, $\Delta\phi_{diff}$, is calculated for both polarised signals (x and y). In addition to this direct phase analysis, the difference of both differential phases is calculated as follows:

$$\Delta\phi_{diff}(z) = \left(\phi^x_{z+GL} - \phi^x_z\right) - \left(\phi^y_{z+GL} - \phi^y_z\right) \tag{6.6}$$

where $\phi^x_{z+GL} - \phi^x_z$ and $\phi^y_{z+GL} - \phi^y_z$ are the phase difference in the GL for both principal axes, x

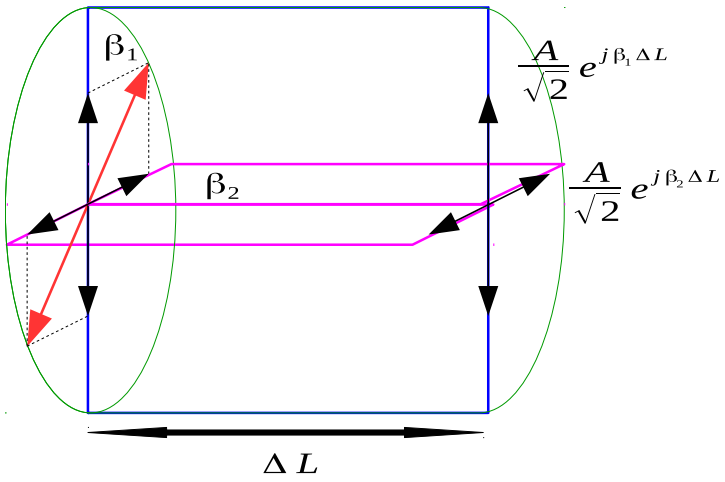

Figure 6.3: Schematic representation of signal propagation through both axis of a PM fiber.

and y, respectively, of the PM fiber. Notice that both phase differences have to be performed before apply unwrapping algorithms. This permits to overcome the failure of the unwrapping algorithm.

Besides, the polarization maintaining configuration of the setup prevents of the presence of polarization fading, as well as Rayleigh fading.

On the one hand, the use of PM fiber with a diversity polarization detection scheme guarantees that both orthogonal polarizations are measured at the same time. On the other hand, the use of both the principal axis of the PM fiber provides two Rayleigh independent signals. Due to the difference in the index of refraction between both axis, light signals experience a different optical path, which is equivalent to the use of different optical frequencies in each optical signal used in each principal axis of the PM fiber.

When small perturbations are applied to the fiber, the difference of the differential phase between both signals is proportional to $\Delta\beta\Delta l$ where $\Delta\beta = \beta_2 - \beta 1$, which is the difference on the propagation coefficients of the principal axis of the fiber and Δl the elongation that a resolution cell suffers due to the perturbation. This system takes advantage of both polarized signals that, in turn, are Rayleigh independent of mitigating fading of the signals through the combination of the signals with inverse-variance weighting as follows [107]:

$$\Delta\phi = A_x\Delta\phi_x + A_y\Delta\phi_y \tag{6.7}$$

where A_x and A_y denote the weight of each inverse-variance and are given by:

$$A_{x,y} = \frac{\sigma_{y,x}^2}{\sigma_x^2 + \sigma_y^2} \tag{6.8}$$

where $\sigma_{x,y}$ denote the variance of the signal differential phase for each polarised measured signal. Moreover, it has to satisfy $A_x + A_y = 1$.

Finally, in contrast to conventional ϕ-OTDR, where a single optical pulse is launched into the FUT to perform the scan, in this chapter, a novel optical codification technique is employed. As discussed in chapter 4, single-pulse ϕ-OTDR sensors, presents an important trade-off between spatial resolution and SNR of the measurement. In order to break this limitation, this system employs a pulse compression technique, based on the use of binary antipodal phase shift keying (PSK) codes, that provides good SNR. This codification was previously studied in the context of radar signals [93], and it has also recently been demonstrated in the optical context. [108]. This

kind of codification is a pseudorandom sequence whose elements jump between both values +1 and -1. Code sequences such as m-sequences and Lagrange-sequences, among others, are a good example of this kind of code, which increases their PSR as the length of the code, N, in increased. Moreover, they can be converted in PPA codes when the values of the settings are changed by $\{exp(j\Phi), +1\}$ where Φ is provided by [109]:

$$\Phi = acos\left(-\frac{N-1}{N+1}\right) \tag{6.9}$$

From Eq. 6.9, it is extracted that, as N is increased, Φ becomes closer to π, becoming in an antipodal set of values, which are simple to implement optically. In addition, when the Legendre code case is analyzed, if N is a prime number that obeys $N = 4k - 1$ being k an integer, the compression of the sequence does not display significant sidelobes, being almost perfect.

As PPA provides an enhancement of the SNR at the same time as good PSR, they are chosen to be used to perform the scan of the FUT in this technique. The interrogation is done launching a sequence of pulses with identical electric envelope, and pseudo-randomly sign (phase), given by:

$$E_{in}(t) = \sum_{k=1}^{N} C_k E_0 a(t - kT_{bit}) \tag{6.10}$$

Where E_0 symbolizes the amplitude of the electric field, $a(t)$ gives the envelope of the pulse and the code element at a position k is denoted by C_k. The envelope of the pulse takes positive values where is contained in the interval $[-T_{bit}/2, T_{bit}/2]$ and drops to 0 elsewhere. Due to the properties of the PPA that $E_{in}(t)$ in Eq. 6.10 exhibits, the compression of the code after matched filtering acquires a form:

$$R(\tau) \approx E_0^2 N R_a(\tau) \tag{6.11}$$

where $R_a(\tau)$ is the autocorrelation of a elementary single pulse. When these PPA codes are used to interrogate FUT in DAS, whose optical field reflected along the whole fiber, is described as follows:

$$E_{FUT}(t) = \int_0^L \rho(z') E_{in}(t - \frac{2z'}{v_g}) dz' \tag{6.12}$$

where v_g denotes the group velocity of the light and L the total length of the fiber. $\rho(z')$ represents the complex backscattering coefficient of the fiber, given by $\rho(x) \approx r(z) exp(-j2\beta z)$. It represents both complex backscattering amplitude ($r(z)$) and optical phase that signal acquires due to the round-trip between input and z-position of the fiber. The complex amplitude of the local backscattering is considered randomly distributed. It can be treated as a white random distribution, so it accomplishes $< r(z')r^*(z'') > \propto \delta(z' - z'')$. Finally, the optical signals that is reflected along the FUT is measured using an I/Q photodetector and cross-correlated with the signal used to perform the scan (Eq. 6.10), giving:

$$R_{FUT}(t) = A \int_0^L \rho(z') R_a(t - \frac{2z'}{v_g}) dz' \tag{6.13}$$

Eq. 6.13 can be understood as a convolution of the autocorrelation for the elementary pulse and the complex profile of the FUT. A is a constant that holds parameters such as gain of the detector and length of the code.

In this section, a mathematical description of the main limitation linked to the detection of high amplitude of the perturbation in phase-recovery ϕ-OTDR has been addressed. Moreover, the mitigation of Rayleigh and polarization fading using the combination of both signals generated from both polarisations. Finally, the fundamental of PPA codes used to enhance the SNR without hurting the spatial resolution at the same time that backscattering is compressed without the apparition of sidelobes.

In the next section, the experimental setup deployed to evaluate the performance of the technique is described.

6.3. Experimental setup

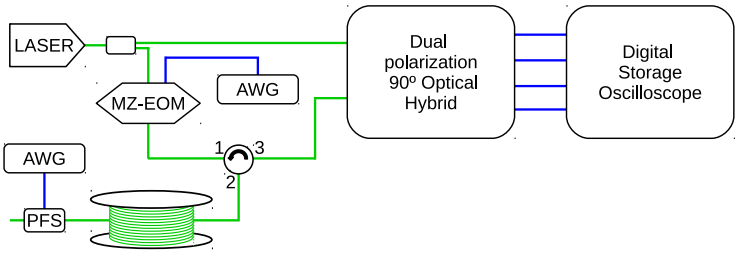

Figure 6.4: the experimental setup. Green lines indicate PM fiber and blue lines denote electrical lines.

Fig. 6.4 depicts schematically the optical setup used in this work. An ultra-coherent laser emitted CW light with linewidth of *sym* 0.1 kHz and power of 21 dBm. Then, a 90:10 PM coupler (R/S) split the optical signal into two branches. One of these, which was used as a reference, was sent directly to a dual polarisation optical hybrid (DPOH). The other output of the coupler was used as a sensing arm. A PM MZ-EOM, that was biased for carrier suppression (minimum transmission) was used to generate the interrogation waveform. The MZ-EOM was driven by a binary antipodal phase shift keying (PSK) sequence of return-to-zero (RZ) pulses. The envelope of the basic pulse (bit) was raised-cosine and its FWHM was 1.5 ns. As usual, the MZ-EOM was driven in push-pull configuration. With these settings the light at the MZ-EOM output comprised RZ pulses which jumped between two opposite phases (0 and π). The modulated optical signal was sent to a PM circulator with linear polarization at an angle of 45° with respect to the principal axes of the device in order to split the power equally between the principal axes of the sensing fiber. It is assumed that cross-coupling between polarizations is negligible. The circulator diverted the signal to a 144-m PM fiber spool that had a PFS attached at its far end. An AWG controlled the frequency and amplitude of the signal that fed the PFS. The reflected light of the optical fiber was directed by the circulator, to the DPOH. Quadrature components of the optical signal (I and Q) for both polarizations were detected using four balanced photodetectors with bandwidths of 800 MHz. The electrical signals were digitized and stored by an oscilloscope at a sampling rate of 2.5 GSamples/s. In this work, the sequence length was chosen to be 6211 leading to a scan period of 9.3165 μs.

Once the experimental setup deployed has been shown, a set of experiments was carried out to demonstrate the performance of the technique.

6.4. Experimental results

A set of experimental verifications have been done in order to demonstrate the potential of the technique presented in this chapter of this thesis.

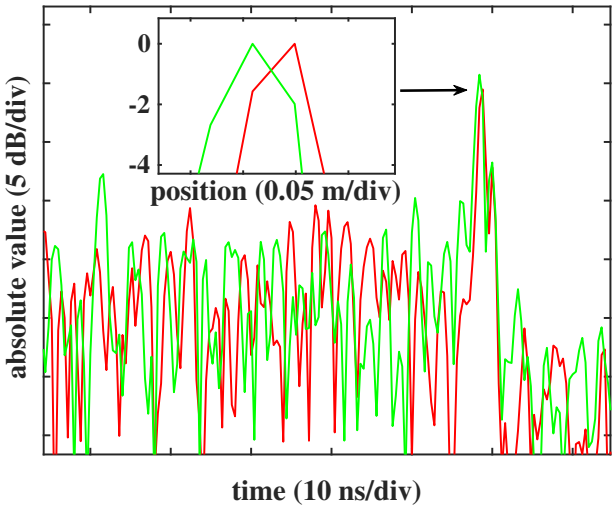

Figure 6.5: Profiles of the absolute value of the reflected signal for each polarisation. The inset shows a detail of both peaks at the far end of the fiber.

Fig. 6.5 shows the Rayleigh profiles of the two principal polarizations in the PM fiber. As mentioned above, since the two polarizations had different refractive indices they traveled different optical paths in the fiber and their Rayleigh profiles were different. This is similar to the case were the measurement is performed with two different frequencies. In the case of a PM fiber with a $\Delta n \approx 0.001$, the equivalent frequency shift is approximately 200 GHz. The peaks of the decoded signals (normalized by their maximum value), at the fiber end, can be seen in the inset of Fig. 6.5. The two peaks appear shifted by 5 cm. The apparent spatial shift is due to the difference in refractive indices and mismatch in the lengths of pigtails and RF cables leading to the detectors. During post processing of the signal, this offset was compensated in order to align the spatial responses of the two polarizations. The FWHM of each of the peaks is seen to be 10 cm. The relatively high noise level which can be seen in Fig. 6.5 in the section right after the fibers end reflection, is attributed to two main factors. The first factor is related to the imperfect implementation of the interrogating pulse sequence and the resulting autocorrelation sidelobes [108]. Another important factor is the relatively large bandwidth (800 MHz) with which the backscattered signal was measured.

To demonstrate measurement of dynamic strain, 62 cm of the PM fiber were wrapped around a piezoelectric cylinder. The cylinder was fed with a sinusoidal signal of 130 Hz and with different amplitudes.

Fig. 6.6 shows the spectrum of the differential phase in the last 4 m of the sensing fiber for both polarizations and for their combination. The spatial separation used for calculating the phase difference was chosen bigger than the length of the wrapped fiber segment to ensure the linearity of the measurement [43]. Spectra were filtered using a bandpass filter between the frequencies of 80 and 2000 Hz. The perturbation at 130 Hz can be observed at the upper right corner of each spectrum. Subplot (c) displays how signal fading induced noise was significantly reduced due to

the combination of the signals in the manner described in Equ. 6.7 and 6.8.

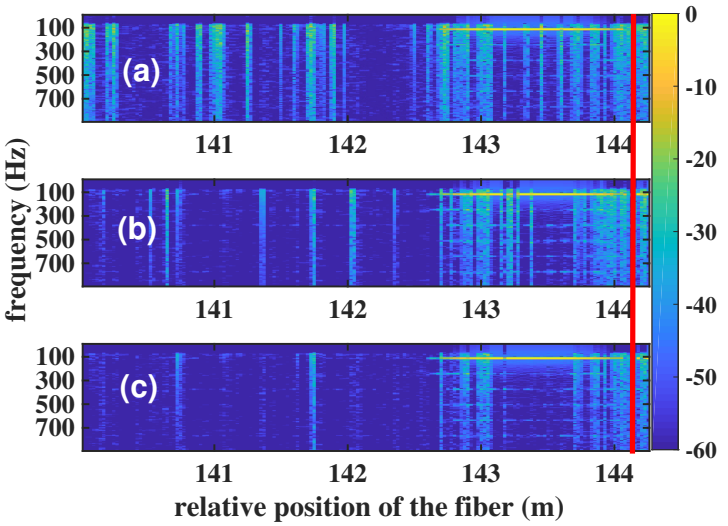

Figure 6.6: Map of the amplitude of the frequency spectrum for (a) horizontal polarization, (b) vertical polarization and (c) combination of them both. Amplitude are in dB and red line indicates the extreme end of the fiber

Spectra of the differential phase power averaged over the location of the excitations are shown in Fig. 6.7. the improvement in SNR in the case of the combined response with respect to the response of each polarization alone is evident. This is primarily due to the great improvement in signal fading in the combined response case. The peak powers of these harmonics are more than 40 dB smaller that the peak at the fundamental frequency and the SNR of the perturbation is $\sim$ 50 dB higher than the noise floor representing sensitivity of $\sim 1.1\, mrad/\sqrt{Hz}$. Note the presence of harmonics of the fundamental frequency of the excitation. The harmonics are attributed to mechanical resonances in the fiber stretching setup.

Fig. 6.8 shows examples of phase difference signals for both polarizations. The examples correspond to a location where one of the polarizations (vertical) had low SNR while the other polarization (horizontal) showed good SNR. Also shown is the weighted sum of the signals according to the inverse variance weighting approach (Eq. 6.7 and 6.8). It can be seen that the combined signal retains the good SNR of the horizontal polarization and is not affected by the fading of the signal of the vertical polarization.

As previously described, when the phase difference, at a given fiber position, between two consecutive scans, exceeds π, unwrapping becomes ambiguous and errors occur. In order to demonstrate this limitation, the amplitude of the excitation applied to the fiber was significantly increased. Figure 6.9 shows the phase differences, $\Delta\phi_{x,y}$, as measured for each polarization, as a function of the excitation amplitude. Red squares and green circles indicate the phase signal measured for the vertical and horizontal polarization components respectively. Note how when the voltage applied to the PFS varied between 0 and 5 V_{pp} the phase signal increased linearly as expected whereas when the voltage exceeded 10 V_{pp} unwrapping ceased to function properly. In the same figure, blue markers refer to $\Delta\phi_{diff}$. It can be seen that the differential phase between the polarization components varies linearly with the amplitude of the excitation. The solid lines in Figure 6.9 are linear fits to the measured values.

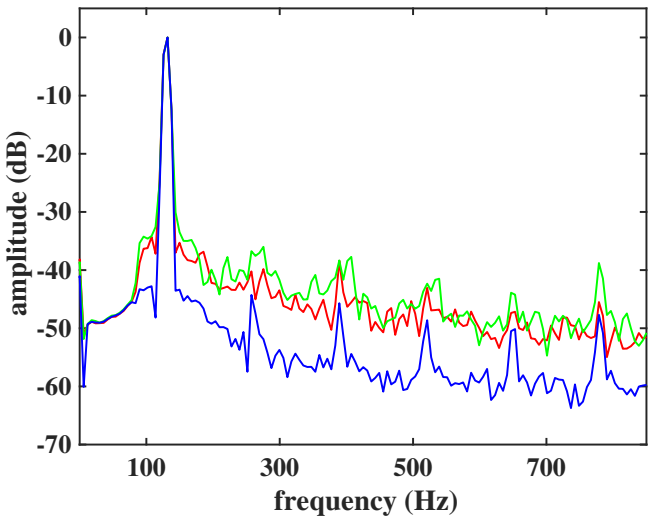

Figure 6.7: Amplitude of the FFT calculated from the differential phase for horizontal polarization (red), vertical polarization (green) and the combination of both measurements (blue).

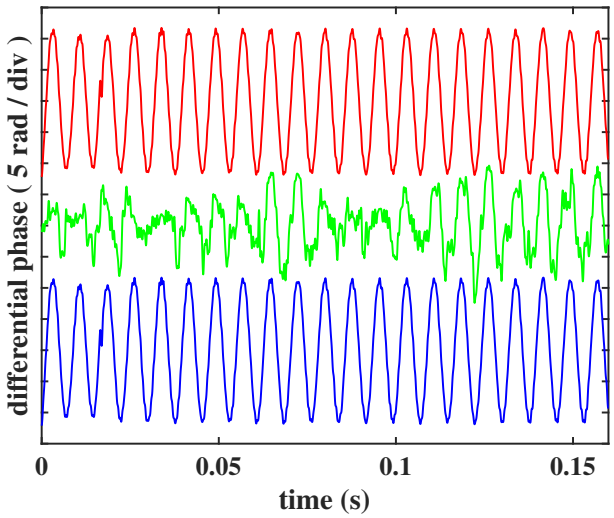

Figure 6.8: Differential phase, in time-domain, in a fiber location inside the perturbation for horizontal polarization (red), vertical polarization (green) and the combination of them both (blue).

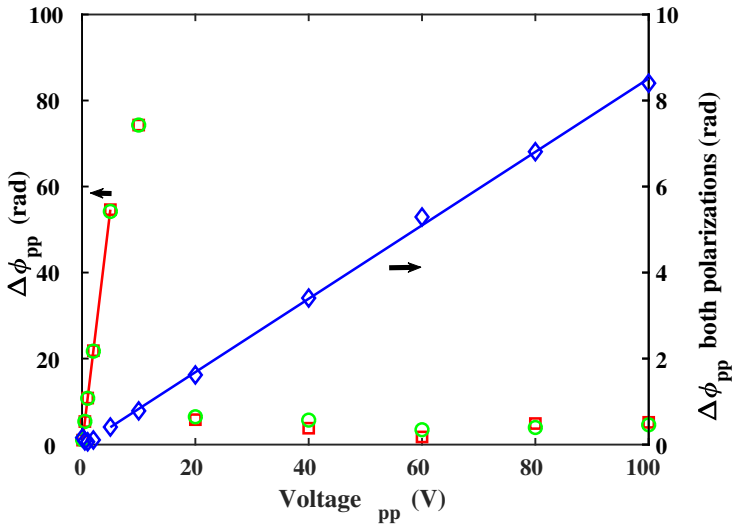

Figure 6.9: Amplitude of the detected perturbation using both polarizations (red and green markers are refered to left axis) for different applied votlages. Blue line indicates the measured amplitude using the differecte between both polarizations.

6.5. conclusions

In this chater, a new system for distributed dynamic strain sensing with high resolution, fast update rate and high sensitivity was presented and tested. The system uses PPA code, a PM sensing fiber and a polarization diversity receiver to achieve zero polarization fading, low probability of signal fading and polarization-differential-phase mode for very large signals. The system operated at a scan rate of ∼107 kHz and achieved spatial resolution of $\sim 10cm$, sensitivity of $\sim 1.1mrad/\sqrt{Hz}$ and ratio between the powers of the maximum and minimum excitations of 136 dB.

CHAPTER 7

Conclusions and open lines

Throughout this thesis, several solutions aimed to enhance the performance of DOFS based on Brillouin and Rayleigh scattering have been presented. Two contributions have been proposed to enhance the performance of BOTDA sensors and three works have been developed to improve the features of DOFS based on Rayleigh scattering.

The conclusions are grouped according to the specific research topic in each kind of sensor.

7.1. Contributions to BOTDA sensors

The contributions to BOTDA sensors have been focused on increasing the power of the probe wave without incurring in NLE and also on generating a distributed amplification over the pump pulsed signal in order to compensate for the effects of the optical attenuation.

7.1.1. Contribution to increase the power of the probe wave

In chapter 2, a system to mitigate second-order NLE is presented. This technique is based on introducing a frequency offset to the FM probe waves that counterpropagate the pump wave in order to follow the distribution of BFS of the fiber. This system has mitigated the apparition of second-order NLE when the power of the probe wave is increased. It has been found that second-order NLE arises when both Brillouin interactions between both prove waves and pump wave do not overlap completely, resulting in a distortion of the spectrum, therefore the shape of the pump wave. A previous technique that develops a frequency modulation of the probe waves partially mitigates second-order NLE [3]. Nevertheless, it fails when BFS is not constant along the fiber since both interactions do not overlap. The frequency offset added to the FM probe wave generates that the central frequency of the probe wave follows the profile of the BFS. As a consequence, the Brillouin interaction of both interactions overlaps completely along the whole fiber, generating a flat zero net interaction that does not generate distortion. To do that, the BFS profile used to modify the FM of the probe wave is firstly measured with low spatial resolution. Then a measurement with the modified FM is done, generating a virtual BFS that is compensated after the measurement. In order to test this technique, the distortion that pulse, due to the

second-order NLE, has been compared when the technique is applied and is not applied, showing a considerable reduction of the distortion when applied. Finally, the largest probe wave power to our acknowledgment, of 15 dBm, which is limited by SpBS, has been used. A spatial resolution of 3 meters with an accuracy of 2 MHz with an average of 1024 samples when a measurement of 120-km fiber link is done..

7.1.2. Contribution to mitigate the attenuation of the pump wave

In chapter 3 We demonstrate a simple technique to provide conventional Brillouin optical time-domain analysis sensors with mitigation for pump pulse attenuation. The technique is based on operating the sensor in loss configuration so that energy is transferred from the probe wave to the pump pulse that becomes amplified as it counter-propagates with the probe wave. Furthermore, the optical frequency of the probe wave is modulated along the fiber so that the pump pulse experiences a flat total gain spectrum that equally amplifies all the spectral components of the pulse, hence, preventing distortion. This frequency modulation of the probe brings additional advantages because it provides increased tolerance to non-local effects and to spontaneous Brillouin scattering noise, so that a probe power above the Brillouin threshold of the fiber can be safely deployed, hence, increasing the signal-to-noise ratio of the measurement. The method is experimentally demonstrated in a 100-km fiber link, obtaining a measurement uncertainty of 1 MHz at the worst-contrast position.

In contrast with chapters 2 and 3, chapters 4, 5 and 6 are based on Rayleigh scattering.

7.2. Contribution to Rayleigh sensors

7.2.1. Contribution to mitigate sidelobes in OPCR technique

In chapter4, a Rayleigh sensor that uses OPCR, avoiding the apparition of sidelobes, is presented. This technique is based on modulating the amplitude of the pulse-envelope. It has been shown that sensors that use OPCR presents the apparition of sidelobes when compression is applied to a squared shape pulse, leading to a degradation of performance of the sensors such as SNR, spatial resolution and interference with close perturbations. It has been demonstrated that the shape of the compression arises from the cross-correlation of the optical FM pulse. As a consequence, a modification of the optical pulse results in a change of the shape of the compression pulse. Unlike radar, optical sensors do not present limitations on the used amplifiers. It permits to apply a pulse modulation that smoothes the output of the MF, avoiding sidelobes. In this work, the desired shape modulation of a Gaussian is applied to the pulse, becoming in a sidelobes free OPCR sensor. With this sensor, a measurement able to detect a phase profile of a perturbation at the extreme end of the 50-km fiber has been demonstrated with a spatial resolution of 0.34 cm.

7.2.2. Contribution to mitigate polarisation and Rayleigh fading in OTDR

In chapter 5, a Rayleigh DOFS that mitigates simultaneously signals and polarization fading is presented. This technique is based on launching consecutively into the fiber, optical pulses with different optical frequencies and SOP. As demonstrated, signal fading appears when the combination of multiple reflected waves becomes destructive interference. Moreover, when two

signals interfere, the efficiency of the mix is modulated by the relative SOP between them, becoming low when the relative SOP is orthogonal. Both effects lead to a low amplitude of the measured signal, resulting in a low SNR that degrades the measurement. It has been found that when the optical frequency is modified, the relative phase between multiple reflected waves changes, consequently the amplitude of the resultant interference, avoiding the signal fading. Moreover, in order to avoid polarization fading, schemes detection that measures both orthogonal polarizations simultaneously have demonstrated to avoid the fading of polarization. However, it presents a penalty of increasing the complexity of the system and duplicate the volume of data to be measured and processed. Our technique launches consecutively four pulses with different optical carried in order to mitigate signal fading. Besides, a DGD inserted in the setup induces a variation of the SOP of each pulse proportional to its optical frequency. When optical frequencies are properly chosen, all the possible SOP are covered by a combination of the four pulses. IT permits to avoid polarization diversity detection scheme and, therefore, to simplify the data processing. Using that, four signals are measured, ensuring, at least one of them is free of both kinds of fading. This sensor has demonstrated to measure a perturbation at the extreme end of a 50-km fiber link with a spatial resolution of 1 meter.

7.2.3. Contribution to extend the dynamic range in ϕ-OTDR

Finally, chapter 6 presents a sensor that extends the dynamic range measurement in DAS. The technique is based on measuring a phase profile of the perturbation that variates slower than the real phase variation. It has been demonstrated theoretically and experimentally that when the amplitude of the perturbation turns to a large value, unwrap algorithm can not reconstruct the measured phase profile since phase jumps bigger that 2π occurs between two consecutive samples. As a consequence, the amplitude of the perturbation able to be measured is limited. In this work, the phase profiles measured consecutively in both axes of PM fiber are combined in order to obtain their difference. This phase difference follows the profile of the perturbation, but its amplitude is drastically reduced proportionally to the difference of refractive index between both axis. To do that, an all PM fiber setup is used to introduce a sequence of pulses, which permits to generate perfect auto-correltaion (PAC), into a PM fiber link with an angle of 45°, generating both phase profile in both axes. Using this technique, a measurement larger than 1000 rad_{pp} has been done.

7.3. Open lines

Finally, to finish this thesis, some open lines are proposed in order to follow the course of this thesis.

In the field of DOFS based on Brillouin scattering, this thesis has been addressed to extend the measurement distance of the sensor. A proposal future research consists on combine techniques deployed in chapter 2 and 3 in order to generate a Brillouin amplification at the same time that second-order NLE are voided. It would permit to increase the power of the probe wave, therefore, the maximum distance of the measurement.

On the other hand, DOFS based on Rayleigh scattering have demonstrated to be able to perform a long-range measurement. Possible future researches to continue on Rayleigh sensor would be to avoid the limitation presented by the technique developed in chapter 6. This technique deploys a PM fiber link in order to combine both measured phase profiles. However, PM fiber presents a high economical cost, which limits the maximum distance that can be measured. The possible

evolution of this work is to employ two different optical wavelengths in standard fiber. Using that, the maximum amplitude able to be measured can be modulated as a function of the frequency separation between both wavelengths.

Bibliography

[1] Luc Thévenaz, Stella Foaleng Mafang, and Jie Lin. Effect of pulse depletion in a Brillouin optical time-domain analysis system. *Opt. Express*, 21(12):14017–14035, Jun 2013.

[2] Alejandro Domínguez-López, Zhisheng Yang, Marcelo A. Soto, Xabier Angulo-Vinuesa, Sonia Martín-López, Luc Thévenaz, and Miguel González-Herráez. Novel scanning method for distortion-free BOTDA measurements. *Opt. Express*, 24(10):10188–10204, May 2016.

[3] R. Ruiz-Lombera, J. Urricelqui, M. Sagues, J. Mirapeix, J. M. López-Higuera, and A. Loayssa. Overcoming nonlocal effects and Brillouin threshold limitations in Brillouin optical time-domain sensors. *IEEE Photonics Journal*, 7(6):1–9, Dec 2015.

[4] Global distributed fiber optic sensing market size and forecast to 2025. https://www.verifiedmarketresearch.com/product/global-distributed-fiber-optic-sensing-market-size-and-forecast-to-2025/. Accessed: 2019-11-11.

[5] Robert W. Boyd. *Nonlinear Optics, Third Edition*. Academic Press, Inc., Orlando, FL, USA, 3rd edition, 2008.

[6] T. Horiguchi, T. Kurashima, and M. Tateda. Tensile strain dependence of brillouin frequency shift in silica optical fibers. *IEEE Photonics Technology Letters*, 1(5):107–108, May 1989.

[7] Govind P. Agrawal. *Nonlinear Fiber Optics, 5th Edition*. The Institute of Optics, University of Rochester, 2013.

[8] Luc Thévenaz. *Advanced Fiber Optics*. EPFL Press, 1st edition, 2011.

[9] Weiwen Zou, Zuyuan He, and Kazuo Hotate. Investigation of strain- and temperature-dependences of brillouin frequency shifts in geo2-doped optical fibers. *J. Lightwave Technol.*, 26(13):1854–1861, Jul 2008.

[10] Kazuo Hotate. A correlation-based continuous-wave technique for measuring brillouin gain spectrum distribution along an optical fiber with centimeter-order spatial resolution. *Proc.SPIE*, 4185:4185 – 4185 – 11, 2000.

[11] Dieter Garus, Katerina Krebber, Frank Schliep, and Torsten Gogolla. Distributed sensing technique based on Brillouin optical-fiber frequency-domain analysis. *Opt. Lett.*, 21(17):1402–1404, Sep 1996.

[12] R. Bernini, A. Minardo, and L. Zeni. Distributed sensing at centimeter-scale spatial resolution by bofda: Measurements and signal processing. *IEEE Photonics Journal*, 4(1):48–56, Feb 2012.

[13] Toshio Kurashima, Tsuneo Horiguchi, and Mitsuhiro Tateda. Distributed-temperature sensing using stimulated brillouin scattering in optical silica fibers. *Opt. Lett.*, 15(18):1038–1040, Sep 1990.

[14] Michael Iten and Alexander M. Puzrin. BOTDA road-embedded strain sensing system for landslide boundary localization. *Proc.SPIE*, 7293:7293 – 7293 – 12, 2009.

[15] Michael Iten and Alexander M. Puzrin. 891769. *Proc.SPIE*, 7647:7647 – 7647 – 15, 2010.

[16] Aldo Minardo, Giuseppe Porcaro, Daniele Giannetta, Romeo Bernini, and Luigi Zeni. Real-time monitoring of railway traffic using slope-assisted brillouin distributed sensors. *Appl. Opt.*, 52(16):3770–3776, Jun 2013.

[17] Marcelo A. Soto and Luc Thévenaz. Modeling and evaluating the performance of brillouin distributed optical fiber sensors. *Opt. Express*, 21(25):31347–31366, Dec 2013.

[18] Dario Alasia, Miguel González-Herráez, Laura Abrardi, Sonia Martín-López, and Luc Thévenaz. Detrimental effect of modulation instability on distributed optical fiber sensors using stimulated brillouin scattering. In *Proceedings Volume 5855, 17th International Conference on Optical Fibre Sensors*, volume 5855, pages 5855 – 5855 – 4, 2005.

[19] Stella M. Foaleng and Luc Thévenaz. Impact of Raman scattering and modulation instability on the performances of Brillouin sensors. In *21st International Conference on Optical Fibre Sensors (OFS21), 2011, Ottawa, Canada*, volume 7753, pages 7753 – 7753 – 4, 2011.

[20] Mohamed N. Alahbabi, Yuh Tat Cho, Trevor P. Newson, Peter C. Wait, and Arthur H. Hartog. Influence of modulation instability on distributed optical fiber sensors based on spontaneous brillouin scattering. *J. Opt. Soc. Am. B*, 21(6):1156–1160, Jun 2004.

[21] Mehdi Alem, Marcelo A. Soto, and Luc Thévenaz. Analytical model and experimental verification of the critical power for modulation instability in optical fibers. *Opt. Express*, 23(23):29514–29532, Nov 2015.

[22] G. P. Agrawal. *Fiber-Optic Communication Systems*. John Wiley and Sons, 2002.

[23] Alejandro Domínguez-López, Xabier Angulo-Vinuesa, Alexia López-Gil, Sonia Martín-López, and Miguel González-Herráez. Non-local effects in dual-probe-sideband Brillouin optical time domain analysis. *Opt. Express*, 23(8):10341–10352, Apr 2015.

[24] Tomoya Shimizu, Kazuhide Nakajima, Kazuyuki Shiraki, Koji Ieda, and Izumi Sankawa. Evaluation methods and requirements for the stimulated Brillouin scattering threshold in a single-mode fiber. *Optical Fiber Technology*, 14(1):10 – 15, 2008.

[25] Asaf David and Moshe Horowitz. Low-frequency transmitted intensity noise induced by stimulated brillouin scattering in optical fibers. *Opt. Express*, 19(12):11792–11803, Jun 2011.

[26] V. I. Kovalev and R. G. Harrison. Threshold for stimulated brillouin scattering in optical fiber. *Opt. Express*, 15(26):17625–17630, Dec 2007.

[27] X. Bao, A. Brown, M. DeMerchant, and J. Smith. *c*haracterization of the *b*rillouin-loss spectrum of single-mode fibers by use of very short (10-ns) pulses. *Opt. Lett.*, 24(8):510–512, Apr 1999.

[28] A. W. Brown, B. G. Colpitts, and K. Brown. Distributed sensor based on dark-pulse brillouin scattering. *IEEE Photonics Technology Letters*, 17(7):1501–1503, July 2005.

[29] S. M. Foaleng, M. Tur, J. Beugnot, and L. Thévenaz. High spatial and spectral resolution long-range sensing using Brillouin echoes. *Journal of Lightwave Technology*, 28(20):2993–3003, Oct 2010.

[30] Wenhai Li, Xiaoyi Bao, Yun Li, and Liang Chen. Differential pulse-width pair BOTDA for high spatial resolution sensing. *Opt. Express*, 16(26):21616–21625, Dec 2008.

[31] Xabier Angulo-Vinuesa, Sonia Martín-López, Javier Nu no, Pedro Corredera, Juan Diego Ania-Casta non, Luc Thévenaz, and Miguel González-Herráez. Raman-assisted Brillouin distributed temperature sensor over 100 km featuring 2 m resolution and 1.2°C uncertainty. *J. Lightwave Technol.*, 30(8):1060–1065, Apr 2012.

[32] X. Angulo-Vinuesa, S. Martín-López, P. Corredera, and M. González-Herráez. Raman-assisted Brillouin optical time-domain analysis with sub-meter resolution over 100 km. *Opt. Express*, 20(11):12147–12154, May 2012.

[33] Sonia Martín-López, Mercedes Alcon-Camas, Félix Rodríguez, Pedro Corredera, Juan Diego Ania-Casta non, Luc Thévenaz, and Miguel Gonález-Herráez. Brillouin optical time-domain analysis assisted by second-order raman amplification. *Opt. Express*, 18(18):18769–18778, Aug 2010.

[34] Javier Urricelqui, Mikel Sagues, and Alayn Loayssa. Brillouin optical time-domain analysis sensor assisted by Brillouin distributed amplification of pump pulses. *Opt. Express*, 23(23):30448–30458, Nov 2015.

[35] Yongkang Dong, Liang Chen, and Xiaoyi Bao. Extending the sensing range of Brillouin optical time-domain analysis combining frequency-division multiplexing and in-line EDFAs. *J. Lightwave Technol.*, 30(8):1161–1167, Apr 2012.

[36] Marcelo A. Soto, Gabriele Bolognini, Fabrizio Di Pasquale, and Luc Thévenaz. Simplex-coded botda fiber sensor with 1 m spatial resolution over a 50 km range. *Opt. Lett.*, 35(2):259–261, Jan 2010.

[37] A. Zornoza, M. Sagues, and A. Loayssa. Self-heterodyne detection for snr improvement and distributed phase-shift measurements in botda. *Journal of Lightwave Technology*, 30(8):1066–1072, April 2012.

[38] Hon. J.W. Strutt. Xv. on the light from the sky, its polarization and colour. *The London, Edinburgh, and Dublin Philosophical Magazine and Journal of Science*, 41(271):107–120, 1871.

[39] John David Jackson. *Classical electrodynamics*. John Wiley and Sons, New York, NY, 3rd ed. edition, 1999.

[40] A. Hartog and M. Gold. On the theory of backscattering in single-mode optical fibers. *Journal of Lightwave Technology*, 2(2):76–82, April 1984.

[41] George W. Stroke. Principles of optics. electromagnetic theory of propagation, interference, and diffraction of light. *Science*, 146(3648):1154–1154, 1964.

[42] Immanuil L. Fabelinskii. *Introduction*. Springer New York, Boston, MA, 1968.

[43] Arthur H Hartog. *An Introduction to Distributed Optical Fibre Sensors*. CRC Press, 2017.

[44] M. K. Barnoski and S. M. Jensen. Fiber waveguides: a novel technique for investigating attenuation characteristics. *Appl. Opt.*, 15(9):2112–2115, Sep 1976.

[45] Kivilcim Yüksel, Marc Wuilpart, Véronique Moeyaert, and Patrice Megret. Optical frequency domain reflectometry: A review (invited). *ICTON 2009: 11th International Conference on Transparent Optical Networks*, 06 2009.

[46] Brian Culshaw S. Gareth Pierce, Alistair MacLean. Optical frequency domain reflectometry for interrogation of microbend-based optical fiber sensors. In *SPIE's 7th Annual International Symposium on Smart Structures and Materials*, volume 3986, 2000.

[47] Sascha Liehr, Nils Nöther, and Katerina Krebber. Incoherent optical frequency domain reflectometry and distributed strain detection in polymer optical fibers. *Measurement Science and Technology*, 21(1):017001, nov 2009.

[48] W. Eickhoff and R. Ulrich. Optical frequency-domain reflectometry in single-mode fibers. In *Integrated Optics and Optical Fiber Communication*, page WF3. Optical Society of America, 1981.

[49] Mark Froggatt and Jason Moore. High-spatial-resolution distributed strain measurement in optical fiber with rayleigh scatter. *Appl. Opt.*, 37(10):1735–1740, Apr 1998.

[50] F. Peng, N. Duan, Y. Rao, and J. Li. Real-time position and speed monitoring of trains using phase-sensitive OTDR. *IEEE Photonics Technology Letters*, 26(20):2055–2057, Oct 2014.

[51] Ning Duan, Fei Peng, Yun-Jiang Rao, Jiang Du, and Yao Lin. Field test for real-time position and speed monitoring of trains using phase-sensitive optical time domain reflectometry (ϕ-otdr). volume 9157, 2014.

[52] J. C. Juarez, E. W. Maier, Kyoo Nam Choi, and H. F. Taylor. Distributed fiber-optic intrusion sensor system. *Journal of Lightwave Technology*, 23(6):2081–2087, June 2005.

[53] Y. Koyamada, M. Imahama, K. Kubota, and K. Hogari. Fiber-optic distributed strain and temperature sensing with very high measurand resolution over long range using coherent otdr. *Journal of Lightwave Technology*, 27(9):1142–1146, May 2009.

[54] L. Zhou, F. Wang, X. Wang, Y. Pan, Z. Sun, J. Hua, and X. Zhang. Distributed strain and vibration sensing system based on phase-sensitive otdr. *IEEE Photonics Technology Letters*, 27(17):1884–1887, Sep. 2015.

[55] Marcelo A. Soto, Xin Lu, Hugo F. Martins, Miguel Gonzalez-Herraez, and Luc Thévenaz. Distributed phase birefringence measurements based on polarization correlation in phase-sensitive optical time-domain reflectometers. *Opt. Express*, 23(19):24923–24936, Sep 2015.

[56] J. Pastor-Graells, H. F. Martins, A. Garcia-Ruiz, S. Martin-Lopez, and M. Gonzalez-Herraez. Single-shot distributed temperature and strain tracking using direct detection phase-sensitive otdr with chirped pulses. *Opt. Express*, 24(12):13121–13133, Jun 2016.

[57] R. Juškaitis, A. M. Mamedov, V. T. Potapov, and S. V. Shatalin. Interferometry with rayleigh backscattering in a single-mode optical fiber. *Opt. Lett.*, 19(3):225–227, Feb 1994.

[58] R. Posey, G. A. Johnson, and S. T. Vohra. Strain sensing based on coherent rayleigh scattering in an optical fibre. *Electronics Letters*, 36(20):1688–1689, Sep. 2000.

[59] E. Gottwald and N. Pietzsch. Measurement method for determination of optical phase shifts in 3x3 fibre couplers. *Electronics Letters*, 24(5):265–266, March 1988.

[60] A Masoudi, M Belal, and T P Newson. A distributed optical fibre dynamic strain sensor based on phase-OTDR. *Measurement Science and Technology*, 24(8):085204, jul 2013.

[61] Dakin John Philip and Lamb Christopher. Distributed fibre optic sensor system.

[62] A E Alekseev, V S Vdovenko, B G Gorshkov, V T Potapov, I A Sergachev, and D E Simikin. Phase-sensitive optical coherence reflectometer with differential phase-shift keying of probe pulses. *Quantum Electronics*, 44(10):965–969, oct 2014.

[63] Z. Pan, K. Liang, Q. Ye, H. Cai, R. Qu, and Z. Fang. Phase-sensitive otdr system based on digital coherent detection. In *2011 Asia Communications and Photonics Conference and Exhibition (ACP)*, pages 1–6, Nov 2011.

[64] Zinan Wang, Li Zhang, Song Wang, Naitian Xue, Fei Peng, Mengqiu Fan, Wei Sun, Xianyang Qian, Jiarui Rao, and Yunjiang Rao. Coherent ϕ-otdr based on i/q demodulation and homodyne detection. *Opt. Express*, 24(2):853–858, Jan 2016.

[65] Govind P. Agrawal. *Fiber Optic Communication Systems, 3rd Edition.* The Institute of Optics, University of Rochester, 1997.

[66] Maurizio Zoboli and Paolo Bassi. High spatial resolution otdr attenuation measurements by a correlation technique. *Appl. Opt.*, 22(23):3680–3681, Dec 1983.

[67] Jean-Jacques Bernard and Emmanuel Depresles. High-resolution correlation otdr for distributed fiber-optic sensors and mobile cabling. *Fiber and Integrated Optics*, 7(2):79–84, 1988.

[68] M. Nazarathy, S. A. Newton, R. P. Giffard, D. S. Moberly, F. Sischka, W. R. Trutna, and S. Foster. Real-time long range complementary correlation optical time domain reflectometer. *Journal of Lightwave Technology*, 7(1):24–38, Jan 1989.

[69] M. D. Jones. Using simplex codes to improve otdr sensitivity. *IEEE Photonics Technology Letters*, 5(7):822–824, July 1993.

[70] Duckey Lee, Hosung Yoon, Na Young Kim, Hansuek Lee, and Namkyoo Park. Analysis and experimental demonstration of simplex coding technique for snr enhancement of otdr. In *Proceedings of the Lightwave Technologies in Instrumentation and Measurement Conference, 2004.*, pages 118–122, Oct 2004.

[71] Duckey Lee, Hosung Yoon, Pilhan Kim, Jonghan Park, Na Young Kim, and Namkyoo Park. Snr enhancement of otdr using biorthogonal codes and generalized inverses. *IEEE Photonics Technology Letters*, 17(1):163–165, Jan 2005.

[72] Weiwen Zou, Shuo Yang, Xin Long, and Jianping Chen. Optical pulse compression reflectometry: proposal and proof-of-concept experiment. *Opt. Express*, 23(1):512–522, Jan 2015.

[73] Arthur Hartog, L. Liokumovich, Nikolai Ushakov, O.I. Kotov, Timothy Dean, T. Cuny, and Alexis Constantinou. The use of multi-frequency acquisition to significantly improve the quality of fibre-optic distributed vibration sensing. 05 2016.

[74] M. Ren, P. Lu, L. Chen, and X. Bao. Theoretical and experimental analysis of ϕ-otdr based on polarization diversity detection. *IEEE Photonics Technology Letters*, 28(6):697–700, March 2016.

[75] Guangyao Yang, Xinyu Fan, Bin Wang, Qingwen Liu, and Zuyuan He. Polarization fading elimination in phase-extracted otdr for distributed fiber-optic vibration sensing. In *2016 21st OptoElectronics and Communications Conference (OECC) held jointly with 2016 International Conference on Photonics in Switching (PS)*, pages 1–3, July 2016.

[76] Q. Yan, M. Tian, X. Li, Q. Yang, and Y. Xu. Coherent ϕ-otdr based on polarization-diversity integrated coherent receiver and heterodyne detection. In *2017 25th Optical Fiber Sensors Conference (OFS)*, pages 1–4, April 2017.

[77] M. Nakazawa. Theory of backward rayleigh scattering in polarization-maintaining single-mode fibers and its application to polarization optical time domain reflectometry. *IEEE Journal of Quantum Electronics*, 19(5):854–861, May 1983.

[78] Juan José Mompó and Alayn Loayssa. Mitigation of polarization and signal fading in distributed vibration sensors. In *26th International Conference on Optical Fiber Sensors*, page WF26. Optical Society of America, 2018.

[79] J. J. Mompo Rosello, S. Lihi, N. Arbel, N. Levanon, A. Loayssa, and A. Eyal. Distributed dynamic strain sensing via perfect periodic coherent codes and a polarization diversity receiver. *Journal of Lightwave Technology*, pages 1–1, 2019.

[80] M. O. van Deventer and A. J. Boot. Polarization properties of stimulated Brillouin scattering in single-mode fibers. *Journal of Lightwave Technology*, 12(4):585–590, April 1994.

[81] A. Minardo, R. Bernini, L. Zeni, Luc Thévenaz, and F. Briffod. A reconstruction technique for long-range stimulated Brillouin scattering distributed fibre-optic sensors: Experimental results. *Measurement Science and Technology*, 16(4):900–8, 2005.

[82] A. Minardo, R. Bernini, and L. Zeni. A simple technique for reducing pump depletion in long-range distributed Brillouin fiber sensors. *IEEE Sensors Journal*, 9(6):633–634, June 2009.

[83] Xiaobin Hong, Wenqiao Lin, Zhisheng Yang, Sheng Wang, and Jian Wu. Brillouin optical time-domain analyzer based on orthogonally-polarized four-tone probe wave. *Opt. Express*, 24(18):21046–21058, Sep 2016.

[84] Alayn Loayssa, Rubén Hernández, David Benito, and Sonia Galech. Characterization of stimulated brillouin scattering spectra by use of optical single-sideband modulation. *Opt. Lett.*, 29(6):638–640, Mar 2004.

[85] G. H. Smith, D. Novak, and Z. Ahmed. Technique for optical ssb generation to overcome dispersion penalties in fibre-radio systems. *Electronics Letters*, 33(1):74–75, 1997.

[86] Flavien Gyger, Etienne Rochat, Sanghoon Chin, Marc Niklès, and Luc Thévenaz. Extending the sensing range of brillouin optical time-domain analysis up to 325 km combining four optical repeaters. *Proc. SPIE*, 9157:91576Q, 2014.

[87] M. Fernandez-Vallejo, D. Olier, A. Zornoza, R. A. Pérez-Herrera, S. Diaz, C. Elosua, C. Bariain, A. Loayssa, and M. L
opez-Amo. 46-km-long raman amplified hybrid double-bus network with point and distributed brillouin sensors. *IEEE Sensors Journal*, 12(1):184–188, Jan 2012.

[88] X. Bao, J. Dhliwayo, N. Heron, D. J. Webb, and D. A. Jackson. Experimental and theoretical studies on a distributed temperature sensor based on brillouin scattering. *Journal of Lightwave Technology*, 13(7):1340–1348, July 1995.

[89] Stella M. Foaleng, Félix Rodríguez-Barrios, Sonia Martín-López, Miguel González-Herráez, and Luc Thévenaz. Detrimental effect of self-phase modulation on the performance of Brillouin distributed fiber sensors. *Opt. Lett.*, 36(2):97–99, Jan 2011.

[90] Y. Awaji, H. Furukawa, B. J. Puttnam, N. Wada, P. Chan, and R. Man. Burst-mode optical amplifier. In *2010 Conference on Optical Fiber Communication (OFC/NFOEC), collocated National Fiber Optic Engineers Conference*, pages 1–3, March 2010.

[91] W. EICKHOFF and R. ULRICH. Optical frequency-domain reflectometry in single-mode fibers. In *Integrated Optics and Optical Fiber Communication*, page WF3. Optical Society of America, 1981.

[92] S. Venkatesh and W. V. Sorin. Phase noise considerations in coherent optical fmcw reflectometry. *Journal of Lightwave Technology*, 11(10):1694–1700, Oct 1993.

[93] Nadav Levanon and Eli Mozeson. *Radar signals*. John Wiley & Sons, 2004.

[94] Shuo Yang, Weiwen Zou, Xin Long, and Jianping Chen. Pulse-compression optical time domain reflectometer. In *OFS2014 23rd International Conference on Optical Fiber Sensors, 2014, Santander, Spain*, volume 9157, 2014.

[95] Zhiqiang Ge, Peikang Huang, and Weining Lu. Matched nlfm pulse compression method with ultra-low sidelobes. In *2008 European Radar Conference*, pages 92–95, Oct 2008.

[96] L. Feng, R. Liting, W. Shunjun, Z. Qiansheng, and Z. Zhiqiang. Design of modified spectrum filter based on mismatched window for nlfm signal. In *2009 2nd Asian-Pacific Conference on Synthetic Aperture Radar*, pages 274–277, Oct 2009.

[97] Ziyi Zhang and Xiaoyi Bao. Distributed optical fiber vibration sensor based on spectrum analysis of polarization-otdr system. *Opt. Express*, 16(14):10240–10247, Jul 2008.

[98] Juan C. Juarez and Henry F. Taylor. Polarization discrimination in a phase-sensitive optical time-domain reflectometer intrusion-sensor system. *Opt. Lett.*, 30(24):3284–3286, Dec 2005.

[99] P. Healey. Statistics of rayleigh backscatter from a single-mode optical fibre. *Electronics Letters*, 21(6):226–228, March 1985.

[100] P. Healey. Statistics of rayleigh backscatter from a single-mode fiber. *IEEE Transactions on Communications*, 35(2):210–214, February 1987.

[101] Dian Chen, Qingwen Liu, and Zuyuan He. Phase-detection distributed fiber-optic vibration sensor without fading-noise based on time-gated digital ofdr. *Opt. Express*, 25(7):8315–8325, Apr 2017.

[102] J. P. Gordon and H. Kogelnik. Pmd fundamentals: Polarization mode dispersion in optical fibers. *Proceedings of the National Academy of Sciences of the United States of America*, 97(9):4541–4550, 2000.

[103] J. Urricelqui, F. López-Fernandino, M. Sagues, and A. Loayssa. Polarization Diversity Scheme for BOTDA Sensors Based on a Double Orthogonal Pump Interaction. *Journal of Lightwave Technology*, 33(12):2633–2638, June 2015.

[104] Michael Bass, Casimer DeCusatis, Jay Enoch, Vasudevan Lakshminarayanan, Guifang Li, Carolyn Macdonald, Virendra Mahajan, and Eric Van Stryland. *Handbook of Optics, Third Edition Volume I: Geometrical and Physical Optics, Polarized Light, Components and Instruments(Set)*. McGraw-Hill, Inc., New York, NY, USA, 3 edition, 2010.

[105] Juan José Mompó, Sonia Martín-López, Miguel González-Herráez, and Alayn Loayssa. Sidelobe apodization in optical pulse compression reflectometry for fiber optic distributed acoustic sensing. *Opt. Lett.*, 43(7):1499–1502, Apr 2018.

[106] Kazuyoshi Itoh. Analysis of the phase unwrapping algorithm. *Appl. Opt.*, 21(14):2470–2470, Jul 1982.

[107] D. Shahar. Minimizing the variance of a weighted average. *Open Journal of Statistics*, 7:216–224, 2017.

[108] Lihi Shiloh, Nadav Levanon, and Avishay Eyal. Highly-sensitive distributed dynamic strain sensing via perfect periodic coherent codes. In *26th International Conference on Optical Fiber Sensors*, page TuE25. Optical Society of America, 2018.

[109] S. W. Golomb. Two-valued sequences with perfect periodic autocorrelation. *IEEE Transactions on Aerospace and Electronic Systems*, 28(2):383–386, April 1992.

List of publications

International journals

1. **J. Mompó**, J. Urricelqui, and A. Loayssa, "Brillouin optical time-domain analysis sensor with pump pulse amplification," Opt. Express 24, 12672-12681 (2016).

2. **J.J. Mompó,** H. Iribas, J. Urricelqui, and A. Loayssa, "Second-Order Nonlocal Effects Mitigation in Brillouin Optical Time-Domain Analysis Sensors by Tracking the Brillouin Frequency Shift Profile of the Fiber," IEEE Photonics Journal, vol. 9, no. 5, pp. 1-12, 2017.

3. H. Iribas, J. Urricelqui, **J.J. Mompó**, J. Mariñelarena, and A. Loayssa, "Non-local effects in Brillouin optical time-domain analysis sensors," Applied Sciences (Switzerland), vol. 7, no. 8, Art. no. 761, 2017.

4. **J. Mompó**, S. Martín-López, M. González-Herráez, and A. Loayssa, "Sidelobe apodization in optical pulse compression reflectometry for fiber optic distributed acoustic sensing," Opt. Lett. 43, 1499-1502 (2018).

5. **J. J. Mompó**, L. Shiloh, N. Arbel, N. Levanon, A. Loayssa and A. Eyal, "Distributed Dynamic Strain Sensing via Perfect Periodic Coherent Codes and a Polarization Diversity Receiver," in Journal of Lightwave Technology, vol. 37, no. 18, pp. 4597-4602, 15 Sept.15, 2019.

Conference proceedings

1. **J.J. Mompó**, Javier Urricelqui, Alayn Loayssa, "Brillouin optical time-domain analysis sensor with amplification of pump pulses and tolerant to non-local effects," Proc. SPIE 9916, Sixth European Workshop on Optical Fibre Sensors, 991634 (30 May 2016);

2. **J.J. Mompó**, Haritz Iribas, Javier Urricelqui, Alayn Loayssa, "Second-order non-local effects mitigation in BOTDA sensors by tracking the BFS profile," Proc. SPIE 10323, 25th International Conference on Optical Fiber Sensors, 103237E (23 April 2017);

3. **J.J. Mompó** and A. Loayssa, "Mitigation of polarization and signal fading in distributed vibration sensors," in 26th International Conference on Optical Fiber Sensors, OSA Technical Digest (Optical Society of America, 2018), paper WF26.

4. Alayn Loayssa, Javier Urricelqui, Haritz Iribas, Jon Mariñelarena, **Juan José Mompó**, "Latest research on long-range Brillouin distributed sensing," Proc. SPIE 10934, Optical, Opto-Atomic, and Entanglement-Enhanced Precision Metrology, 109340K (1 March 2019);

5. J. Mariñelarena, **J. J. Mompó**, J. Zurita, J. Urricelqui, A. Judez, M. López Amo, S. Jiménez, A. Achaerandio, A. Loayssa, "Structural health monitoring of solar trackers using distributed fiber optic sensors," Proc. SPIE 10970, Sensors and Smart Structures Technologies for Civil, Mechanical, and Aerospace Systems 2019, 109701V (27 March 2019)

Book chapters

1. A. Loayssa, J. Urricelqui, H. Iribas, **J.J. Mompó**, and J. Mariñelarena, "Fiber-optic Brillouin distributed sensors: from dynamic to long-range measurements," In: Sensors for Diagnostics and Monitoring, CRC Press, K338070, ch. 2, 2018.